UNIVERSITÀ POLITECNICA DELLE MARCHE

DOCTORAL THESIS IN INFORMATION ENGINEERING
CURRICULA BIOMEDICAL, ELECTRONICS AND
TELECOMMUNICATION ENGINEERING – XVI CYCLE

Analysis of Complex and Chaotic Electromagnetic Structures: the Reverberation Chamber and its Applications

---

Author:
Luca BASTIANELLI

Supervisors:
Prof. Franco MOGLIE
Prof. Valter MARIANI PRIMIANI

A thesis submitted in fulfillment of the requirements
for the degree of Doctor of Philosophy

in the

Dipartimento di Ingegneria dell'Informazione

UNIVERSITÀ
POLITECNICA
DELLE MARCHE

UNIVERSITÀ POLITECNICA DELLE MARCHE

Abstract

Dipartimento di Ingegneria dell'Informazione

Doctor of Philosophy

Analysis of Complex and Chaotic Electromagnetic Structures: the Reverberation Chamber and its Applications

by Luca BASTIANELLI

This dissertation deals with the study of complex electromagnetic cavities, evaluated by theoretical, numerical and experimental results obtained by using the reverberation chamber. This facility was chosen due to their characteristics, in particular the possibility to create a random field within it. The main activity was based on the development of techniques and assumptions in order to improve the performance of the chamber, focusing at relatively low frequency, in other words near the minimum frequency where the chamber well operates. Performance can be improved by design a new stirrer optimized and tailored for the specific chamber or applications. Another solution is to modify the geometry of the chamber, this solution contrary to the adoption of a new-shaped stirrer is less expensive and applicable in already existing chambers. The challenge was to connect the improvement due to these irregular-shaped chamber to the lowest usable frequency, empirically evaluated as three-six times the frequency of the fundamental mode of the considered chamber. New shaped chambers have been carried out by adding curved diffractor along their perimeter. Simulations performing the finite-difference time-domain method have been done in order to investigate the effects due to diffractors. In this dissertation the performance were evaluated in terms of characteristic parameter used in electromagnetic compatibility tests. Results show that the improvement at relatively low frequency (considering a large chamber w.r.t. the wavelength) is given by the increase of the modal overlap whereas a typical parameter taken into account during electromagnetic compatibility tests, i.e. number of uncorrelated positions, decreases. This relevant improvement that could arise to a lower shift of the lowest usable frequency is predictable by a simple model derived using the quality factor without a priori information of the chamber. Experimental measurements were performed in the reverberation chamber of our laboratory (DII – UNIVPM), just, to provide a qualitative comparison with simulations. Not all configurations were replicated in the laboratory. Moreover, the reverberation chamber was used in order to carry out more experimental measurements, i.e. emulation of a real life environment, shielding effectiveness tests.

Acknowledgements

The Ph.D. course has been a great and exciting experience of my life! Not only from the scientific/academic point of view, but also for the cultural exchange with fantastic people who I met. I would like to thank all people that I met and with which I exchanged opinion and ideas during this period. In particular, I owe my deepest gratitude to:

⋆ Prof. Franco Moglie and Prof. Valter Mariani Primiani, my tutors in Ancona. I am grateful to them for teaching me many skills. Experimental bases for EMC tests and advanced numerical knowledge. They deserve a special mention for efforts made to following me with consistency and continuity.

⋆ Not least thank to Dr. Gabriele Gradoni, friend/supervisor which teach me advanced mathematical tools and always he is able to find a relation from everything to "Waves" and "Chaos". Many thanks again for the patience and for the wonderful dinners in Nottingham. followed me during my period in Nottingham, and steadily helps me!

⋆ A relevant acknowledge to my girlfriend Emma who supported and tolerated me for the whole course, since the beginning!

⋆ All the people with whom i collaborated during these years. In particular, Davide Micheli (Università La Sapienza di Roma), Angelo Gifuni (Università Parthenope di Napoli), Massimo Barazzetta (Nokia), Riccardo Diamnanti (Telecom Italia), Luk R. Arnaut (Queen's Mary University of London London), Gregor Tanner, Stephen Craig and David Thomas (University of Nottingham).

⋆ Thanks to Hayan and Aidee, i never forget the time spent together in Nottingham and time spent to "try" to perfectly cook "Italian Pasta"!

⋆ Thanks to all colleagues Valentina, Luigi, Giovanni, Matteo, Eleonora, Giorgio, Carmine, Sandy, Armando, Mattia, Filippo and all students who performed experimental activities at the university.

⋆ Finally, a thought to my family who always substained me! Thanks!

Moreover, i would like to acknowledge the School of Mathematical Sciences, University of Nottingham, for hospitality during my visiting period; and the two projects where I was involved:

- COST Action IC1407 (ACCREDIT) for the opportunity gave me by the short term scientific mission (STSM)

- PRACE and ISCRA projects for award the access to resource FERMI (before) and MARCONI (after) based in Italy at CINECA.

Contents

List of Figures

List of Tables

Introduction

Since the last 20 years the reverberation chamber (RC), beside the use in acoustic, have been receiving more and more interest as facility test in particular in electromagnetic compatibility (EMC) tests. The peculiarity of this facility is that the electromagnetic field is statistically uniform, isotropic and without depolarization in a defined region called working volume (WV), within an acceptable uncertainty and confidence limit. Moreover, another notable advantage of this facility is that performed measurements are robust, repeatable in the radio-frequency (RF) and microwave ranges [2–6]. The same measurement after long time (if necessary) will have the same results, due to the statistical properties. The field within the cavity consists of alternate maxima and minima that due to the continuous change of the boundary conditions, then an average between the chamber's realizations is made. The statistical properties of this cavity are attained by the field mixing (stirring) obtained in different ways. There are more than one stirring processes, the most common is due by an irregular metallic structure called stirrer that rotates continuously n order to change the boundary conditions within the chamber. Besides the mechanical stirrer it is possible to apply a source stirring, positioning stirrer, frequency stirring or a combination of them. Each chamber realization, corresponding to a stirrer position, consists to a set of different modes that are independent each other and remarking that the deterministic field in the cavity evolves randomly as the boundary conditions are stochastic [7] will be adopted a random plane wave spectrum as a model for the field. This supports a statistical approach for the analysis (e.g. mean value, high-order momentum, probability density function). The operation of an RC in opposite to the anechoic chamber.

During my Ph.D. in engineering information I was engaged in theoretical, experimental and numerical investigation of electromagnetic fields in complex cavity, i.e. the RC [8, 9].

Most efforts have been addressed on the study of chaotic cavities with the purpose of improve the performance of an already existing (large) RC, in particular focusing at low frequency, as mush as possible below the lowest usable frequency (LUF). One of the most relevant challenge is the establishment of a physically motivated description for the LUF [10], still empirically evaluated [11]. This analysis was done in collaboration with Dr. Gabriele Gradoni (University of Nottingham) where I spent part of my Ph.D. improving my knowledge in advanced and applied mathematics. The basic idea is to adopt a new shape of the RC inspired by geometries explored in dynamical systems belong to the quantum chaos field. The simplest way is to design a chamber with non-parallel walls, but this is not a convenient approach if the RC is already made. Besides non-parallel

one can modify the geometry by inserting curved diffractors i.e. spheres/hemispheres within the RC, easier solution for an existing RC w.r.t. the non-parallel walls. In this way the energy localization drastically decreases and a consequence is the decrease of regular orbits in the phase space as well. In fact regular modes are basically stationary waves given to the symmetry of the problem. On the contrary chaotic modes are ergodic and do not exhibit regular paths [12, 13]. Several works were addressed to this field in particular by adopting the Random Matrix Theory (RMT) [14, 15]. In this thesis was adopted another approach, closer to the EMC where their characteristic parameters were considered and analyzed, i.e. number of uncorrelated stirrer positions, field uniformity. The analysis was done by powerful simulations that implementing the finite-difference time-domain (FDTD) method. This study and preliminary results have gathered positive and constructive criticism by the community. The results that stem from this work are useful to the community as they show the impact of diffractors on key parameters defined in the standard, which must be met for valid use of the reverberation chamber in an lectromagnetic compatibility (EMC) tests.

In order to improve the chamber's behavior new stirrer/s can be designed. This is a common and efficient practice to optimize the proper chamber, but this solution is tailored to the specific chamber and difficult to export for other chambers. Anyway, the definition and evaluation of a helically shaped stirrer was done.

Moreover, the RC can be used to replicate real-life environments, because it is a rich multipath environment, exploited for emulating real-life sites e.g. indoor/outdoor environment, over-the-air test (OTA). In this thesis is reported the analysis done in order to match the standard requirements for the validation of the chamber for tests and some results. Further experimental measurements were performed, using the reverberation chamber facilities at the University of Nottingham. The capability of an RC to reproduce a real scenario is very important and allows to save money and time for measurements e.g. remaining in the laboratory instead of moving all instruments out of the laboratory, i.e. OTA tests.

Results about the electromagnetic characterization of concrete samples were reported, this emphasize the wide use of the RC.

Chapter 1

The reverberation chamber

The reverberation chamber (RC), Figure 1.2, is basically an overmoded electrically large cavity, with an high quality factor. Its name derive by the reverberating room used in acoustics. The main feature of this environment are that the electro-magnetic field inside a defined region, called working volume (WV), is statistically uniform, isotropic and depolarized within an acceptable uncertainty and confidence limit. The capability to obtain the previous statistical properties are due to the stirring process.

The RC is used in electromagnetic compatibility (EMC) tests. We are going to describe more deeply its feature later. We begin this thesis with a brief recall of the Electromagnetic Theory, used for the analysis and for explain the basis of the Finite-Difference Time-Domain (FDTD) technique described in Chapter 2.

1.1 Maxwell's equations

As previously mentioned, the RC is a cavity made by conducting walls and uniformly filled by a dielectric, usually air. A brief remark of fundamentals of electromagnetic theory is needed to understand and explain the properties of a cavity, i.e. modes exited in a rectangular cavity. The International System of Units (SI) will be used on this thesis.

Consider a region of the space without electric or magnetic current sources, the time dependent Maxwell's equations are: Faraday's Law:

$$\frac{\partial \mathbf{B}}{\partial t} = -\nabla \times \mathbf{E} - \mathbf{M} \tag{1.1}$$

Ampere's Law:

$$\frac{\partial \mathbf{D}}{\partial t} = \nabla \times \mathbf{H} - \mathbf{J} \tag{1.2}$$

Gauss' Law for the electric field:

$$\nabla \cdot \mathbf{D} = 0 \tag{1.3}$$

Gauss' Law for the magnetic field:

$$\nabla \cdot \mathbf{B} = 0 \tag{1.4}$$

in differential form, whereas Faraday's Law:

$$\frac{\partial}{\partial t}\iint_A \mathbf{B}\cdot d\mathbf{A} = -\oint_l \cdot\mathbf{E}d\mathbf{l} - \iint_A \mathbf{M}\cdot d\mathbf{A} \tag{1.5}$$

Ampere's Law:

$$\frac{\partial}{\partial t}\iint_A \mathbf{D}\cdot d\mathbf{A} = \oint_l \mathbf{H}\cdot d\mathbf{l} - \iint_A \mathbf{J}\cdot d\mathbf{A} \tag{1.6}$$

Gauss' Law for the electric field:

$$\oiint_A \mathbf{D}\cdot d\mathbf{A} = 0 \tag{1.7}$$

Gauss' Law for the magnetic field:

$$\oiint_A \mathbf{B}\cdot d\mathbf{A} = 0 \tag{1.8}$$

for the integral form, where

- **E** is the electric field [V/m]
- **D** is the electric flux density [C/m^2]
- **H** is the magnetic field [A/m]
- **B** is the magnetic flux density [Wb/m^2]
- **J** is the electric current density [A/m^2]
- **M** is the equivalent magnetic current density [V/m^2]
- A is a three dimensional surface [m^2] and $d\mathbf{A}$ the differential normal vector of the surface A [m^2]
- l is the contour of the surface A [m] and $d\mathbf{l}$ the differential length vector of the contour l [m].

For isotropic, linear and nondispersive materials the constitutive relations are:

$$\mathbf{D} = \epsilon\mathbf{E} = \epsilon_r\epsilon_0\mathbf{E} \qquad \mathbf{B} = \mu\mathbf{H} = \mu_r\mu_0\mathbf{H} \tag{1.9}$$

$$\mathbf{J} = \mathbf{J}_{source} + \sigma\mathbf{E} \qquad \mathbf{M} = \mathbf{M}_{source} + \sigma^*\mathbf{H} \tag{1.10}$$

where

- **J** and **M** act as independent source of the E-field and H-field energy, $\mathbf{J}_{source}$ and $\mathbf{M}_{source}$

- ϵ is the electrical permittivity [F/m]
- ϵ_r is the relative electrical permittivity [dimensionless]
- ϵ_0 is the free-space permittivity [F/m]
- μ is the magnetic permeability [H/m]
- μ_r is the relative permeability [dimensionless]
- μ_0 is the free-space permeability [H/m]
- σ is the electric conductivity [S/m]
- σ^* is the equivalent magnetic loss [Ω/m]

Then, substitute (1.9) and (1.10) into (1.1) and (1.2), assuming linear, isotropic, lossy and nondispersive materials we obtain:

$$\frac{\partial \mathbf{H}}{\partial t} = -\frac{1}{\mu}\nabla \times \mathbf{E} - \frac{1}{\mu}\left(\mathbf{M}_{source} + \sigma^* \mathbf{H}\right) \tag{1.11}$$

$$\frac{\partial \mathbf{E}}{\partial t} = \frac{1}{\epsilon}\nabla \times \mathbf{H} - \frac{1}{\epsilon}\left(\mathbf{J}_{source} + \sigma \mathbf{E}\right) \tag{1.12}$$

now, for the six vector components expressed in the Cartesian coordinates of the curl operators of (1.11) and (1.12) we can write the following system of six coupled scalar equations:

$$\frac{\partial H_x}{\partial t} = \frac{1}{\mu}\left[\frac{\partial E_y}{\partial z} - \frac{\partial E_z}{\partial y} - \left(M_{source_x} + \sigma^* H_x\right)\right] \tag{1.13}$$

$$\frac{\partial H_y}{\partial t} = \frac{1}{\mu}\left[\frac{\partial E_z}{\partial x} - \frac{\partial E_x}{\partial z} - \left(M_{source_y} + \sigma^* H_y\right)\right] \tag{1.14}$$

$$\frac{\partial H_z}{\partial t} = \frac{1}{\mu}\left[\frac{\partial E_x}{\partial y} - \frac{\partial E_y}{\partial x} - \left(M_{source_z} + \sigma^* H_z\right)\right] \tag{1.15}$$

and

$$\frac{\partial E_x}{\partial t} = \frac{1}{\epsilon}\left[\frac{\partial H_z}{\partial y} - \frac{\partial H_y}{\partial z} - \left(J_{source_x} + \sigma E_x\right)\right] \tag{1.16}$$

$$\frac{\partial E_y}{\partial t} = \frac{1}{\epsilon}\left[\frac{\partial H_x}{\partial z} - \frac{\partial H_z}{\partial x} - \left(J_{source_y} + \sigma E_y\right)\right] \tag{1.17}$$

$$\frac{\partial E_z}{\partial t} = \frac{1}{\epsilon}\left[\frac{\partial H_y}{\partial x} - \frac{\partial H_x}{\partial y} - \left(J_{source_z} + \sigma E_z\right)\right] \tag{1.18}$$

This system of equations, from (1.13) to (1.18), are very important because they form the basis for the FDTD algorithm for the electromagnetic wave interactions in relation with a general three dimensional object [16], discussed later.

Considering the curl equations (1.1) and (1.2) and using the curl of the curl identity[1] we obtain the wave equations:

$$\frac{\partial^2 E}{\partial t^2} = c_0^2 \frac{\partial^2 E}{\partial x^2} \tag{1.19}$$

$$\frac{\partial^2 H}{\partial t^2} = c_0^2 \frac{\partial^2 H}{\partial x^2} \tag{1.20}$$

where c_0 is the speed of the light in the free space, $c = 1/\sqrt{\mu_0 \epsilon_0}$ [m/s].

1.2 Reverberation chamber features

1.2.1 Plane wave superposition

In order to satisfy the Maxwell's equations it has been chosen a plane wave integral representation for the electric and magnetic field. For an RC, the statistical behavior of fields is taken into account by random variables that represent the plane wave coefficients. The use of a plane wave spectrum for the reverberation chamber was proposed in [7]. The field of a cavity can be analytically represented by an angular spectral expansion of an ensemble plane waves (PWS)

$$\mathbf{E}(\mathbf{r}) = \iint_{4\pi} \mathbf{F}(\Omega) \exp(\jmath \mathbf{k}\cdot\mathbf{r})\, d\Omega \ . \tag{1.21}$$

The electric field $\mathbf{E}(\mathbf{r})$ of a region, without sources can be represented as an integral of plane waves: where $\mathbf{F}$ is the angular spectrum and the Ω the angle that includes both the elevation and azimuth angles referring to Figure 1.1, α and β respectively, and $d\Omega = \sin\alpha d\alpha d\beta$; $\mathbf{k}$ represents the vector wavenumber:

$$\mathbf{k} = -k(\hat{x}\sin\alpha\cos\beta + \hat{y}\sin\alpha\sin\beta + \hat{z}\cos\alpha), \ . \tag{1.22}$$

The geometry for a component, Figure 1.1, is given by

$$\mathbf{E}(\mathbf{r}) = \int_0^{2\pi}\int_0^{\pi} \mathbf{F}(\alpha\beta) \exp(\jmath \mathbf{k}\cdot\mathbf{r}) \sin d\alpha d\beta \ . \tag{1.23}$$

The angular spectrum is

$$\mathbf{F}(\Omega) = \hat{\alpha} F_\alpha(\Omega) + \hat{\beta} F_\beta(\Omega) \tag{1.24}$$

where α and β are unit vectors orthogonal each other and to k. Both F_α and F_β are complex and can be written as

$$F_\alpha(\Omega) = F_{\alpha r}(\Omega) + \jmath F_{\alpha_J}(\Omega) \ \ , \ \ F_\beta(\Omega) = F_{\beta r}(\Omega) + \jmath F_{\beta_J}(\Omega) \tag{1.25}$$

[1] $\nabla \times (\nabla \times A) = \nabla(\nabla \cdot A) - \nabla^2 A$

The **F** can be deterministic or random. However, for the field generated inside the RC **F** is considered to be a random variable. In the RC the ensemble is due to the chamber's realization, i.e. stirrer positions when a mechanical stirring technique is used. Appropriate statistical assumptions for such a field are

$$\langle F_\alpha(\Omega)\rangle = \langle F_\beta(\Omega)\rangle = 0 \tag{1.26}$$

$$\begin{aligned}
&\langle F_{\alpha r}(\Omega_1)F_{\alpha J}(\Omega_2)\rangle = \langle F_{\beta r}(\Omega_1)\beta_J(\Omega_2)\rangle = \\
&\langle F_{\alpha r}(\Omega_1)F_{\beta r}(\Omega_2)\rangle = \langle F_{\alpha r}(\Omega_1)F_{\beta J}(\Omega_2)\rangle = \\
&\langle F_{\alpha J}(\Omega_1)F_{\beta r}(\Omega_2)\rangle = \langle F_{\alpha J}(\Omega_1)F_{\beta J}(\Omega_2)\rangle = 0 \ ,
\end{aligned} \tag{1.27}$$

$$\begin{aligned}
&\langle F_{\alpha r}(\Omega_1)F_{\alpha r}(\Omega_2)\rangle = \langle F_{\alpha J}(\Omega_1)\alpha_J(\Omega_2)\rangle = \\
&\langle F_{\beta r}(\Omega_1)F_{\beta r}(\Omega_2)\rangle = \langle F_{\beta J}(\Omega_1)F_{\beta J}(\Omega_2)\rangle = C_E\delta(\Omega_1-\Omega_2) \ ,
\end{aligned} \tag{1.28}$$

$$\langle F_\alpha(\Omega_1)F^*_\beta(\Omega_2)\rangle = 0 \ , \tag{1.29}$$

$$\langle F_\alpha(\Omega_1)F^*_\alpha(\Omega_2)\rangle = \langle F_\beta(\Omega_1)F^*_\beta(\Omega_2)\rangle = 2C_E\delta(\Omega_1-\Omega_2) \ , \tag{1.30}$$

where δ is the Dirac function, $C_E = E_0^2/(16\pi)$ [V/m^2] is a constant, $<.>$ denotes the ensemble average, $(\Omega_1-\Omega_2)$ represents the difference between two sets of random plane waves and * denotes the complex conjugate. basically, results of these relations mean that the field is due by several rays with random phase, the in-phase and quadrature components with orthogonal polarizations of the angular spectrum are uncorrelated, how indicated by the δ function of (1.28). In order to derive statistical properties of the field we can start with

$$\langle \mathbf{E}\rangle = \iint_{4\pi}\langle \mathbf{F}(\Omega)\rangle \exp(\jmath\,\mathbf{k}\cdot\mathbf{r}d\Omega = 0 \tag{1.31}$$

that is the random polarization property. Thus, the mean value of electric field is null. From the square of the absolute value of electric field is given by

$$|\mathbf{E}| = \iint_{4\pi}\iint_{4\pi}\mathbf{F}(\Omega_1)\cdot\mathbf{F}^*(\Omega_2)\exp[\jmath\,(\mathbf{k_1}-\mathbf{k_2})\cdot\mathbf{r}]d\Omega_1 d\Omega_2 \tag{1.32}$$

and manipulating 1.32 is obtained

$$\begin{aligned}
&\langle|\mathbf{E}|^2\rangle = 4C_E\iint_{4\pi}\iint_{4\pi}\delta(\Omega_1-\Omega_2)\exp[\jmath\,(\mathbf{k_1}-\mathbf{k_2})\cdot\mathbf{r}]d\Omega_1 d\Omega_2 = \\
&= 4C_E\iint_{4\pi}d\Omega_2 = 16\pi C_E \equiv E_0^2
\end{aligned} \tag{1.33}$$

Equation (1.33) gives the spatial uniformity property. Similarly can be derived the mean square values for the Cartesian components of electric field as

$$\langle |E_x|^2 \rangle = \langle |E_y|^2 \rangle = \langle |E_z|^2 \rangle = \frac{E_0^2}{3} \ , \tag{1.34}$$

this denotes the ideal isotropy properties. From (1.26) follows

$$\langle E_{xr} \rangle = \langle E_{xJ} \rangle = \langle E_{yr} \rangle = \langle E_{yJ} \rangle = \langle E_{zr} \rangle = \langle E_{zJ} \rangle = 0 \ , \tag{1.35}$$

then by the variance theorem yields

$$\sigma^2 \equiv \frac{E_0^2}{6} \ , \tag{1.36}$$

where σ^2 is the variance. The maximum entropy method can be adopted to derive the probability density function (pdf) from (1.35) and (1.36), i.e. considering the complex Cartesian components E_{xr} with zero mean the maximum entropy points out the pdf $f(E_{xr})$ in order to maximize the entropy given by

$$-\int_{-\infty}^{+\infty} f(E_{xr}) \ln [f(E_{xr})] \, dE_{xr} \ , \tag{1.37}$$

then

$$\int_{-\infty}^{+\infty} f(E_{xr}) dE_{xr} = 1 \ . \tag{1.38}$$

After the maximization the result is the non-unique Gauss normal distribution

$$f(E_{xr}) = \frac{1}{\sqrt{2\pi}\sigma} \exp\left[-\frac{E_{xr}^2}{2\sigma^2} \right] \ . \tag{1.39}$$

The same probability is applied to others real and imaginary parts of electric field components. Upon the spherical to rectangular transformation of the angular spectrum is possible to prove the complex field uncorrelation for all the components

$$\langle (E_{xr})(E_{xJ}) \rangle = 0 \ . \tag{1.40}$$

Since the Gauss normal distributed with zero mean and same variance the pdf of the field magnitude and squared magnitude (intensity and power) becomes χ and χ^2 with appropriate degree of freedom (*dof*). In particular for the magnitude of a Cartesian component χ distributed with two *dof*, a Rayleigh distribution [17]

$$f(|E_x|) = \frac{|E_x|}{\sigma^2} \exp\left[-\frac{|E_x|^2}{2\sigma^2} \right] \ , \tag{1.41}$$

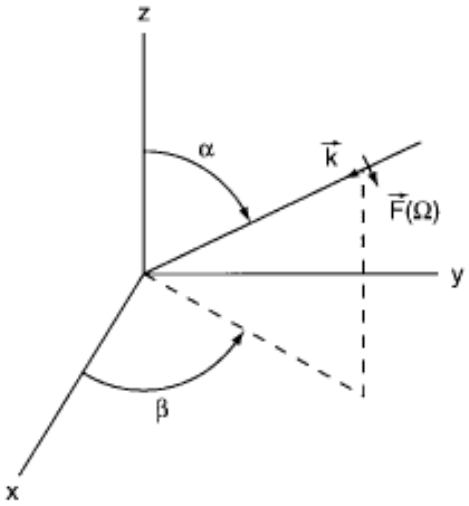

FIGURE 1.1: Reference system of the $\mathbf{F}(\Omega)$ components.

with σ^2 denotes the variance of the Cartesian components. Then, the squared magnitude of the Cartesian component is χ^2 distributed with two *dof*, an exponential distribution

$$f(|E_x|^2) = \frac{1}{2\sigma^2}\exp\left[-\frac{|E_x|^2}{2\sigma^2}\right], \tag{1.42}$$

the eq. (1.41) and (1.42) were validated by observations and measurement [18–20]. Furthermore, the total electric field magnitude $|E|$ is χ distributed with six *dof* with the following pdf

$$f(|E_x|) = \frac{|E|^5}{8\sigma^6}\exp\left[-\frac{|E|^2}{2\sigma^2}\right], \tag{1.43}$$

while the squared magnitude of the total electric field is χ^2 distributed with six *dof* with the following pdf

$$f(|E_x|^2) = \frac{|E|^4}{16\sigma^6}\exp\left[-\frac{|E|^2}{2\sigma^2}\right]. \tag{1.44}$$

The dual probability density functions, and previous results, for the magnetic field can obtained by, i.e.

$$\langle H_{xr}^2 \rangle = \frac{E_0^2}{6\eta^2} \equiv \sigma_H^2 \tag{1.45}$$

replacing E by H and σ and σ_H.

1.2.2 Modal description

Modes within a rectangular cavity are determined by the boundary conditions. For a deterministic analysis it is possible to use the modal approach. This kind of description is

not rigorous, but useful for our scope. In a rectangular resonator, without losses with dimensions a, b and c representing the length, width and height respectively, the electromagnetic field is stationary and solving the transverse wave equation the wavenumber is given by [21]:

$$k_{l,m,n} = \sqrt{\left(\frac{l\pi}{a}\right)^2 \left(\frac{m\pi}{b}\right)^2 \left(\frac{n\pi}{c}\right)^2} \tag{1.46}$$

where l, m and n are non-negative indexes of modes, related to the Cartesian components $\hat{x}$, $\hat{y}$ and $\hat{z}$ respectively. The propagation starts above the cut-off frequency of the cavity, evaluated by:

$$f_{l,m,n} = \frac{1}{2\sqrt{\mu\epsilon}} \sqrt{\left(\frac{l}{a}\right)^2 \left(\frac{m}{b}\right)^2 \left(\frac{n}{c}\right)^2} \,. \tag{1.47}$$

When indexes l, m and n are not-null the mode degeneracy occurs, modes with five components. Conversely, if at least one index is null will exist three field components, summarized in Table 1.1. The total modal density $N(k)$ of a cavity can be obtained as a linear combination of the densities $N_i(k)$

$$N(k) = N_1(k) + N_2(k) + N_3(k) + N_4(k) + N_5(k) \tag{1.48}$$

Alternatively, an approximated definition for the evaluation of the overall modal density is given by the Weyl's law [22]:

$$N_s(f) = \frac{8\pi V f^3}{3c^3} - (a+b+c)\frac{f}{c} + \frac{1}{2} \tag{1.49}$$

where c is the speed of the light in the vacuum. This law can be adopted also for a not-rectangular cavity [23]. In spite of many studies have been directed to give a more rigorous definition of the LUF based on the Weyl's law and by a physical point of view, the LUF is still evaluated by empirical approach [11]. This empirical law "separates" the overmoded from the undermoded regime is from 3 to $6 \times f_0$ where f_0 represents the frequency of the fundamental mode[2].

Mode family	**Cartesian field components**	**Modal density**
TM_{lmn}	E_x, E_y, E_z, H_x, H_y	$N_1(K)$
TE_{lmn}	E_x, E_y, H_x, H_y, H_z	$N_2(K)$
TM_{lm0}	E_z, H_x, H_y	$N_3(K)$
TE_{0mn}	E_x, H_y, H_z	$N_4(K)$
TM_{l0n}	E_y, H_x, H_z	$N_5(K)$

TABLE 1.1: Modal structure for a static cavity, and densities.

[2] TE_{101}

1.2.3 Quality factor

Further attained the regime of well-operating condition the quality factor (Q) can be evaluated. For an unstirred cavity the Q (dimensionless) is defined by [19]

$$Q = \omega \frac{U}{P_d} \tag{1.50}$$

where ω is the angular frequency, U the energy stored and P_d the total dissipated power. The energy U can be expressed as a product of

$$U_s = W \cdot V \tag{1.51}$$

where W is the energy density and V the volume of the cavity. The energy density in a RC is statistically uniform because of the field homogeneity

$$W = \epsilon_0 E^2 \tag{1.52}$$

where ϵ_0 is the electrical permittivity of the vacuum and E^2 is given by the ensemble average over the chamber's realization, i.e. stirrer rotation. The power density can be rewritten as

$$S_C = \frac{E^2}{\eta} = \sqrt{\frac{\epsilon_0}{\mu_0}} E^2 = c\,W \tag{1.53}$$

where μ_0 is the magnetic permeability in the free-space and c is the speed of the light in the vacuum; S_C [W/m^2] and W [J/m^3]. Losses within an enclosure is mainly due to the power dissipated by the metallic boundaries (P_{d1}), power absorbed by internal objects (P_{d2}), power leaking through apertures (P_{d3}) and the power dissipated by antennas (P_{d4}). Considering these four contribute averaged over the lossy objects within the RC. Losses due to the aperture can be evaluated in a similar way, defining before the equivalent transmission cross section σ_L, averaged over 2π steradians hemisphere that surrounds the aperture. A factor of $1/2$ has to be accounted, so the result is

$$P_{d3} = \frac{\langle \sigma_L \rangle S_c}{2} \quad . \tag{1.54}$$

The third term is given by

$$Q_3 = \omega \frac{U_S}{P_{d3}} = \omega \frac{2V}{\langle \sigma_L \rangle c} = \frac{4\pi V}{\lambda \langle \sigma_L \rangle} \tag{1.55}$$

If the RC is well shielded this term should not be taken into account. At low frequency the power dissipated on the antenna loads become dominant. The received power can be found by

$$P_{d4} = S_C \langle A_l \rangle \tag{1.56}$$

where $\langle A_l \rangle$ represents the effective area of an isotropic radiator

$$\langle A_l \rangle = \frac{m\lambda^2}{8\pi} \tag{1.57}$$

where m is the mismatching antenna factor ($m = 1$ for matched load) and the relative Q_4 is given by

$$Q_4 = \frac{16\pi^2 V}{m\lambda^3} \tag{1.58}$$

if there are N identical receiving antennas we have to multiply (1.57) and divide (1.58) by N. We can note that this contribute $\propto f^3$ is dominant at low frequency.

Considering a coupled RC, the power transmitted by an external source is given by the equivalent cross section σ_L

$$P_T = \frac{S_i \langle \sigma_L \rangle}{2} \tag{1.59}$$

where S_i is the incident power density through the aperture; at the stationary state the P_T must to be the same of the dissipated power P_d

$$P_d = \omega \frac{U_S}{Q} \ , \tag{1.60}$$

which respects the power conservation principle. The balance equation give

$$S_C = \left(\frac{\langle \sigma_t \rangle Q\lambda}{4\pi V} \right) S_i \tag{1.61}$$

then considering S_C to be uniform so the shielding effectiveness (SE) for the aperture can be defined by the following expression

$$SE = 10\log \frac{S_i}{S_C} = 10\log \left(\frac{4\pi V}{\langle \sigma_t \rangle \lambda Q} \right) \ . \tag{1.62}$$

It is noticing that a lossy cavity has a higher shielding effect compared to a cavity with a high Q-factor. In order to highlight the effect of losses consider before a lossless cavity except the aperture, it means $P_{d1} = P_{d2} = P_{d4} = 0$ and

$$Q = Q_3 = \frac{4\pi V}{\langle \sigma_L \rangle \lambda} \tag{1.63}$$

then substituting (1.63) in (1.61) yields

$$S_C = \frac{\langle \sigma_t \rangle}{\langle \sigma_L \rangle} S_i \ . \tag{1.64}$$

Introducing the power balance $P_T = P_d$ by using (1.58) (1.51) and (1.53) we obtain

$$P_T = \frac{2\pi V S_C}{\lambda Q} \tag{1.65}$$

and

$$S_C = \frac{P_T \lambda Q}{2\pi V} \ , \tag{1.66}$$

and the received power is

$$P_r = S_C \langle A_l \rangle = S_C \left(\frac{\lambda^2}{8\pi} \right) = \left(\frac{\lambda^3 Q}{16\pi^2 V} \right) P_T \tag{1.67}$$

at the end the Q-factor is given by [11]

$$Q = \frac{16\pi^2 V}{\lambda^3 \eta_{TX} \eta_{RX}} \left(\frac{P_r}{P_T} \right) \tag{1.68}$$

where $e\,t\,a_{TX}$ and η_{RX} are antenna coefficients representing their efficiency, for the transmitting and receiving respectively. In Chapter 6 is described the setup for the SE evaluation of different elements, and the nested reverberation chamber as well.

1.2.4 Uncorrelated stirrer positions

In order to create a random field within the RC there are several stirring techniques [24, 25]:

- mechanical stirring
- frequency stirring
- source stirring
- positioning stirring
- "wall" stirring
- combination of them.

FIGURE 1.2: Picture of the Ancona's RC.

The mechanical stirring is the most common, it is basically a metallic, non-symmetric structure placed inside the RC that continuously rotates. By rotating, the stirrer provides to increase the set of excites modes[3], for each position the set of excites mode should not

[3] different for each stirrer position due to the fact that changes the boundary condition

be the same, otherwise two close positions that do not exhibit an appreciable different means that they are correlated and the stirrer performance is low. The stirrer performance are evaluated by the number of uncorrelated stirrer positions, discussed later. In this sense, a well-operated stirrer improves the chaoticity of the field within the RC. More than one stirrer could be used at the same time both in synchronous or interleaved way. During the experimental measurements the stirrer can be used in two modality [26]:

- tuned mode: where the frequency sweep is completed for each stirrer position (step by step)
- stirring mode: opposite to the tuned mode the stirrer rotates continuously for each frequency of the band.

The shape and dimension of the stirrer are very important parameter and they affect the behavior of the RC, in fact a stirrer should be electrically large corresponding at least to $\lambda/4$. Moreover, like in the acoustic reverberating room, inserting diffractor improves the performance [27, 28]. The most common shape of a stirrer is the z-folded, where a metallic sheet (thin sheet) is bended similar to a "z" (avoiding any symmetries) Figure 1.3. Obviously other shapes have been designed and proposed over the years [27, 29–31] in

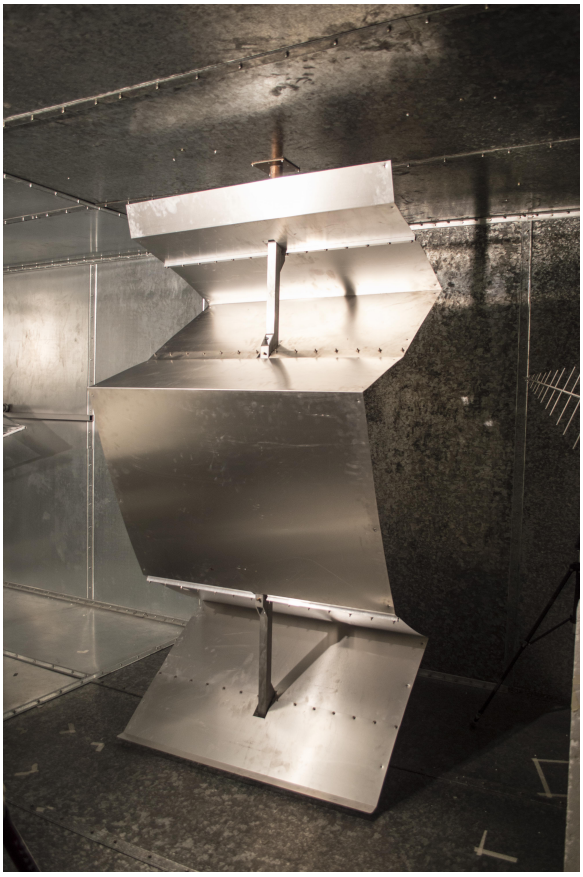

FIGURE 1.3: Picture of the vertical z-folded stirrer of the Ancona's RC.

order to improve the performance, Figures 1.3, 1.4 and 1.5 report some examples. As previously mentioned, the number of uncorrelated stirrer positions (stirrer efficiency)

FIGURE 1.4: Picture of the (temporary) horizontal stirrer of the Ancona's RC.

FIGURE 1.5: Picture of the vertical stirrer of the Nottingham's RC.

is a key parameter in order to evaluate the performance of the considered stirrer and consequently affects the overall behavior of the RC. To this purpose considering many stirrer steps is useful because

- the larger the steps the larger the points used for the statistical analysis, increasing the precision on the mean value of the field

- the larger the steps the greater the ratio between maximum and mean value of the field, in order to achieve the maximum field less power is needed $\left(f(N)=\frac{|E_{MAX}|}{\langle|E|\rangle}\right)$ with N the tuner steps. This feature is relevant about immunity tests,

unfortunately increasing the stirrer steps imply a rise of the measurement time.

Considering that for each stirrer position N samples[4] of the receiving power are acquired by the vector network analyzer (VNA) and stored in an array a

$$a_i = a_{i+kN} \qquad k \in \mathbb{Z}, \ , \tag{1.69}$$

the $i-th$ value of this array is computed by [11]

$$\rho_i = \frac{\sum_{j=0}^{N-1} a_j a_{j+i}}{\sigma_{2a}} \tag{1.70}$$

where $0 \leq i \leq N-1$ and

$$\sigma_{2a} = \frac{1}{N-1} \sum_{j=0}^{N-1} \left(a_j - < a >\right)^2 \tag{1.71}$$

corresponds to the variance of the array a, this method is called auto-correlation function (ACF). Hence, the number of uncorrelated stirrer positions of the stirrer N_{ind} are

FIGURE 1.6: Example of a 1-D correlation. The crosses indicate the uncorrelated states.

given by the ratio between the samples N and the autocorrelation values that are greater than a threshold, which is reported in the standard [11] and is computed by

$$r = \frac{1}{e}\left(1 - \frac{7.22}{N^{0.64}}\right) \tag{1.72}$$

If there are two stirrers (or more set of samples see Figure 2.4 in Chapter 2) that operate in interleaved mode[5] it is possible to adopt the multivariate approach [32]. The multivariate approach is based on the field probed points within the WV. First of all the matrix of the fields (e) is filled

$$\underline{\underline{e}} = \begin{bmatrix} e_1^{(1)} & \dots & e_1^{(N_s)} \\ e_2^{(1)} & \dots & e_2^{(N_s)} \\ \vdots & \ddots & \vdots \\ e_{N_p}^{(1)} & \dots & e_{N_p}^{(N_s)} \end{bmatrix} \tag{1.73}$$

[4] the number of samples depend on the VNA resolution

[5] otherwise if two or more stirrers operate in synchronous way they correspond to a unique stirrer where the total steps are due to the sum of each stirrer.

where the rows represent the probed points on the grid and the columns represent vectors made of stirrer positions. Then, the Pearson correlation coefficient between the stirrer positions field arrays j and k is computed for all the probed points by

$$\rho_{jk} = \frac{\mathrm{Cov}\left(\underline{\underline{e}}^{(j)}, \underline{\underline{e}}^{(k)}\right)}{\sqrt{\mathrm{Var}\left(\underline{\underline{e}}^{(j)}\right)\mathrm{Var}\left(\underline{\underline{e}}^{(k)}\right)}} \tag{1.74}$$

and the correlation matrix is completed as:

$$\underline{\underline{R}} = \begin{bmatrix} \rho_{11} & \rho_{12} & \cdots & \rho_{1N_s} \\ \rho_{21} & \rho_{22} & \cdots & \rho_{2N_s} \\ \vdots & \vdots & \ddots & \vdots \\ \rho_{N_s1} & \rho_{N_s2} & \cdots & \rho_{N_sN_s} \end{bmatrix} \tag{1.75}$$

The last step is to count the uncorrelated stirrer positions by using the same threshold r [11] in this way

$$N_u = \frac{N_s^2}{\#[\underline{\underline{R}} > r]} \ . \tag{1.76}$$

In practice the number of uncorrelated stirrer states is given by the total number of the matrix elements divided by the elements greater than the threshold.

Figure Figure 1.7 shows an example of the autocorrelation whereas Figure 1.7 an example of the correlation matrix.

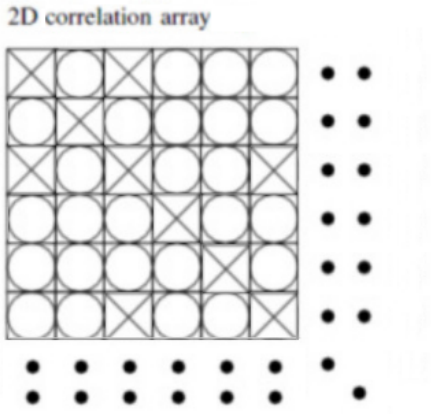

FIGURE 1.7: Example of a 2-D correlation. The crosses indicate the uncorrelated states.

a peculiarity of the correlation matrix is that the evaluation of the uncorrelated states does not depend on the order. More precisely, the same results are obtained if the $p_{i,j}$ are computed following the rows or columns. This property is not true for the autocorrelation function. The multivariate approach is more accurate than the ACF method, but it requires longer time in order to collect fields value to fill the matrix of events.

1.2.5 Field uniformity

The field uniformity is a very important parameter for the validation of the RC and provides to guarantee a correct position of the DUT (within the validated WV). The field is considered uniform if it is below the limit reported in the standard [11] (3 dB above 400 MHz, 4 dB at 100 MHz decreasing linearly to 3 dB at 400 MHz, and within 4 dB below 100 MHz). The standard deviation, reported in eq. (1.77), provides the values within the tolerance accepted by the normative [11]. The standard deviation [dB] is expressed by:

$$\sigma_{24} = 20\log\left(\frac{\sigma_{24} + \langle E_{x,y,z}\rangle}{\langle E_{x,y,z}\rangle}\right) \tag{1.77}$$

where the σ_{24} is the standard deviation evaluated on 24 probe positions, 8 for each Cartesian component, and $\langle E_{x,y,z}\rangle$ is the arithmetic mean of the normalized E_{MAX} from all the 24 probed positions. The average E-field for all the three Cartesian components was evaluated by:

$$\langle E\rangle_{24} = \frac{\sum E_{x,y,z}}{24} \tag{1.78}$$

where $< . >$ represents the arithmetic mean and and $\sum$ was done by the 24 rectangular probed E-values and

$$\sigma_{24} = \sqrt{\frac{\sum_{m=1}^{8}\sum_{n=1}^{3}\left(E_{m,n} - \langle E\rangle_{24}\right)^2}{24-1}} \tag{1.79}$$

is the standard deviation made by all vectors $\hat{x}$, $\hat{y}$ and $\hat{z}$; m and n denote the probe location 1 to 8 and the axis 1 to 3 respectively.

Chapter 2

The Finite-Difference Time-Domain method

2.1 Introduction

The Finite-Difference Time-Domain (FDTD) is a numerical method able to solve complex problems as the Maxwell's equations in the time domain, i.e. analysis and design of antennas, evaluation of the propagation of signals etc. The FDTD is based on the Yee's algorithm [33], presented the first time in [1] in 1966 and still valid. It is one of the most used/common numerical techniques, in particular thanks to the advent of higher performance computers.

The FDTD method has got pros and cons, as whichever numerical method. Also in the FDTD some approximations were done. The main advantages of the FDTD are:

- is conceptually simple to understand
- take advantage of the time domain, using a broadband signal (Gaussian pulse) it is possible to cover a wide range of frequencies with a single simulation
- E and H fields are evaluated in the considered domain, so it is possible to trace their evolution
- this technique allows us to specify the material at all grid points in the computational domain
- the FDTD code is easily parallelizable with the OpenMP[1] and MPI[2] libraries

whereas, the main disadvantages of this technique are:

- it requires that the whole domain must be gridded and the discretization has to be sufficiently fine in order to take into account the smallest wavelength of the electromagnetic field
- space and time steps have to satisfy the Courant condition [1]
- requires high powerful computers and a large amount of memory

[1] http://www.openmp.org/
[2] http://www.open-mpi.org/

- for a cavity with a high Q-factor implies very long time for simulations.

In the FDTD differential equations are transposed and approximated[3] into finite-difference equations (FDE) for both spatial and temporal derivatives (Ampere's 1.2 and Faraday's 1.1 laws) by means of the Taylor's series expansions [1].

Yee's algorithm, developed by Kane Yee [33], can be highlighted with following steps:

1. replacing the finite differences of the Ampere's and Faraday's laws, discretize the space and time obtaining electric and magnetic field staggered in space and time
2. compute the equations in order to have the "updated equations" that allow us to know the future fields by the past fields (2.9)
3. compute the magnetic fields one time step into the future
4. compute the electric fields one time step into the future
5. repeat step 3 and 4 for all the duration.

The resulting scheme consists by linear equations where future values (t_{i+1}) of the electric/magnetic field are going to be evaluated by their previous values (t_i), already stored in the memory, see (2.9).

The iterative procedure has the 6 Cartesian components of the field. Figure Figure 2.1 shows the elementary cubic cell that forms the Yee lattice [1]. The electric filed is computed at the center of the faces of the cubic cell whereas the magnetic one at the edges. In this way the electric field component is surrounded by four magnetic components and every magnetic component surrounded by four electric ones [1]. Moreover, the electric and magnetic components are evaluated at different time steps, i.e. electric ones at $n \cdot \Delta t$ and the magnetic ones at $(n+1/2) \cdot \Delta t$, where $n = 1,2,3,\cdots$, see Figure 2.2 that shows the leapfrog scheme for the time derivative. Then the whole geometry[4] will be discretized by a 3-D lattice, the cell size is an important parameter because it defines the spatial resolution of the whole simulation. It is worth noticing that a finer cell size shows a better resolution but implies a higher computational burden. On the contrary, a small cell size make worse the resolution and affects the discretization of relative small object.

Starting from the curl equations (1.1) and (1.2) we obtain the following system:

$$\begin{cases} \frac{\partial H_z}{\partial y} - \frac{\partial H_y}{\partial z} = \epsilon \frac{\partial E_x}{\partial t} + \sigma E_x \\ \frac{\partial H_x}{\partial z} - \frac{\partial H_z}{\partial x} = \epsilon \frac{\partial E_y}{\partial t} + \sigma E_y \\ \frac{\partial H_y}{\partial x} - \frac{\partial H_x}{\partial y} = \epsilon \frac{\partial E_z}{\partial t} + \sigma E_z \\ \frac{\partial E_y}{\partial z} - \frac{\partial E_z}{\partial y} = \mu \frac{\partial H_x}{\partial t} + \sigma^* H_x \\ \frac{\partial E_z}{\partial x} - \frac{\partial E_x}{\partial z} = \mu \frac{\partial H_y}{\partial t} + \sigma^* H_y \\ \frac{\partial E_x}{\partial y} - \frac{\partial E_y}{\partial x} = \mu \frac{\partial H_z}{\partial t} + \sigma^* H_z \end{cases} \tag{2.1}$$

[3] after a spatio-temporal quantization

[4] the RC and devices for our case

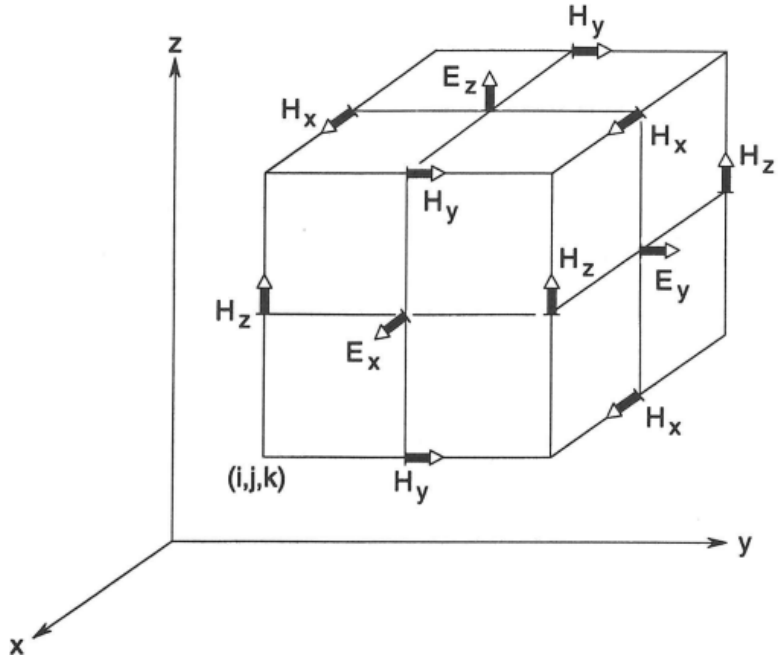

FIGURE 2.1: Elementary cubic (unitary) cell size of the Yee space lattice where the position of the electric and magnetic field components are reported [1].

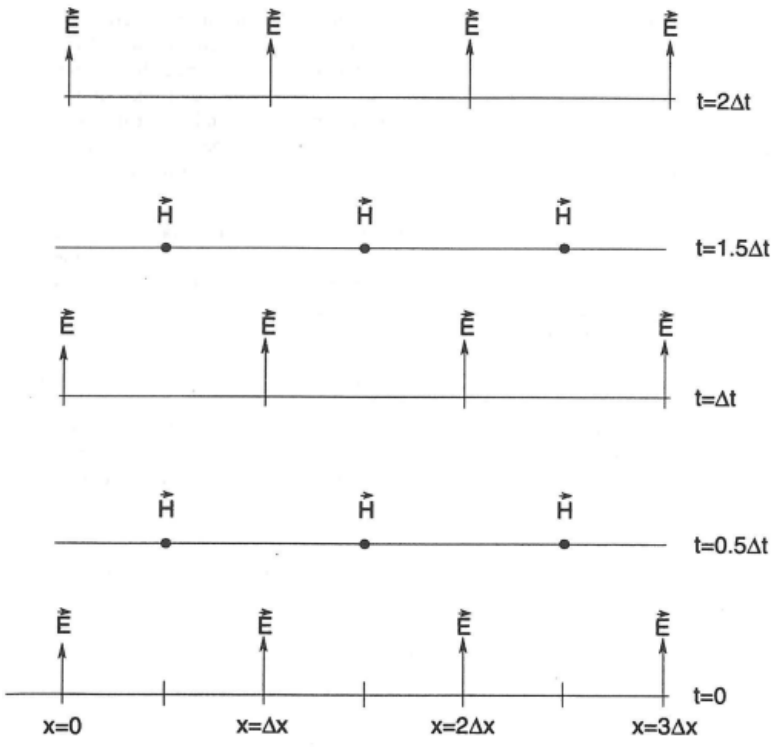

FIGURE 2.2: Space-time scheme of the Yee algorithm [1].

where σ^* is the equivalent magnetic conductivity[5].

[5] added in order to make the system symmetric.

In order to transform the differential equations in finite difference equations we need some steps [16]. Considering the function $u(x,t_n)$ and its expansion about the space point x_0 to the space point $x_0 \pm \Delta x$, the time step (t_n) remains fixed, we have:

$$u\left(x_0 \pm \Delta x\right)|t_n = u|_{x_0,t_n} \pm \Delta x \frac{\partial u}{\partial x}|_{x_0,t_n} + \frac{(\Delta x)^2}{2}\frac{\partial^2 u}{\partial x^2}|_{x_0,t_n} \pm \frac{(\Delta x)^2}{3}\frac{\partial^3 u}{\partial x^3}|_{x_0,t_n} + \frac{(\Delta x)^4}{24}\frac{\partial^4 u}{\partial x^4}|_{xi,t_n} \tag{2.2}$$

where the last term indicates the error. Adding the two expansions of 2.2, referred to $(+\Delta x)$ and $(-\Delta x)$ respectively, we obtain:

$$u\left(x_0+\Delta x\right)|t_n + u\left(x_0-\Delta x\right)|t_n = 2u|_{x_o,t_n} + \frac{(\Delta x)^2}{2}\frac{\partial^2 u}{\partial x^2}|_{x_0,t_n} + \frac{(\Delta x)^4}{24}\frac{\partial^4 u}{\partial x^4}|_{xi,t_n} \tag{2.3}$$

and rearranging the terms:

$$\frac{\partial^2 u}{\partial x^2}|_{x_0,t_n} = \left[\frac{u\left(x_0+\Delta x\right)-2u\left(x_0\right)+u\left(x_0-\Delta x\right)}{\left(\Delta x\right)^2}\right] + O\left[\left(\Delta x\right)^2\right] \tag{2.4}$$

where $O\left[\left(\Delta x\right)^2\right]$ is the notation for the term error. It approaches to zero as the square of the space increment. Adopting another notation for (2.4), that represents the central difference approximation to the second partial space derivative of u with second-order of accuracy (2.4), i for the space position and n for the time step we can rewrite it as:

$$\frac{\partial^2 u}{\partial x^2}|_{x_0,t_n} = \frac{u_{i+1}^n - 2u_i^n + u_{i-1}^n}{\left(\Delta x\right)^2} + O\left[\left(\Delta x\right)^2\right] \tag{2.5}$$

and the for the time derivative of u:

$$\frac{\partial^2 u}{\partial t^2}|_{x_0,t_n} = \frac{u_i^{n+1} - 2u_i^n + u_i^{n-1}}{\left(\Delta t\right)^2} + O\left[\left(\Delta t\right)^2\right] \tag{2.6}$$

Then, substituting (2.5) and (2.6) into the one-dimensional scalar wave equation $\frac{\partial^2 u}{\partial t^2} = c^2\frac{\partial^2 u}{\partial x^2}$ we obtain:

$$\frac{u_i^{n+1} - 2u_i^n + u_i^{n-1}}{(\Delta t)^2} + O\left[(\Delta t)^2\right] = c^2\left\{\frac{u_{i+1}^n - 2u_i^n + u_{i-1}^n}{\left(\Delta x\right)^2} + O\left[\left(\Delta x\right)^2\right]\right\} \tag{2.7}$$

that represents an approximation of the second-order accuracy to the scalar wave equation both in space and time. Disregarding remainders $O\left[\left(\Delta x\right)^2 + \left(\Delta t\right)^2\right]$ and solving for the latest value of u at the point i on the grid we obtain the fully explicit expression for u_i^{n+1} with the second order of accuracy:

$$u_i^{n+1} = \left(c\Delta t\right)^2\left[\frac{u_{i+1}^n - 2u_i^n + u_{i-1}^n}{\left(\Delta x\right)^2}\right] + 2_i^n - u_i^{n-1} \tag{2.8}$$

We can note that on the right side of (2.8) the quantities are known; in fact they were obtained in the previous steps n and $n-1$. In this way the process can be repeated for all space points, this repetition represents the FDTD solution of the scalar wave equation.

A case of special interest is when $c\Delta t = \Delta x$, for its peculiarity this value is called magic time-step. For this value, the solution of the FDTD equation is an exact solution to the differential wave equation; the result is:

$$u_i^{n+1} = \left(u_{i+1}^n - 2u_i^n + u_{i-1}^n\right) + 2_i^n - u_i^{n-1} = u_{i+1}^n + u_{i-1}^n - u_i^{n-1}, \quad . \tag{2.9}$$

Finally, considering the function $u(x,t) = F(x+ct) + G(x-ct)$ as the one-dimensional scalar wave equation solution with F and G are taken as arbitrary functions and knows as propagating-wave solutions.

By using the Yee's notation the volume of the cell is given by

$$\Delta v = \Delta x \cdot \Delta y \cdot \Delta z \tag{2.10}$$

and for a uniform spatial discretization a space point in a rectangular lattice is denoted by:

$$(i,j,k) = (i\Delta x, j\Delta y, k\Delta z) \tag{2.11}$$

with Δx, Δy and Δz are the lattice space increment about the $\hat{x}$, $\hat{y}$ and $\hat{z}$ directions respectively. Then, considering any function of space and time $F(x,y,z,t)$ after its discretization over the space and time we obtain

$$F|_{i,j,k}^n = F(i\Delta x, j\Delta y, k\Delta z, n\Delta t) \tag{2.12}$$

where Δt is the time increment. With the new notation the partial derivatives of 2.1 with the proper incremental ratios yield:

$$\begin{cases} \frac{\partial F}{\partial x} = \frac{F|_{i+1,j,k}^n - F|_{i,j,k}^n}{\Delta x} + O((\Delta x)^2) \\ \frac{\partial F}{\partial y} = \frac{F|_{i,j+1,k}^n - F|_{i,j,k}^n}{\Delta y} + O((\Delta y)^2) \\ \frac{\partial F}{\partial z} = \frac{F|_{i,j,k+1}^n - F|_{i,j,k}^n}{\Delta z} + O((\Delta z)^2) \\ \frac{\partial F}{\partial t} = \frac{F|_{i,j,k}^{n+1} - F|_{i,j,k}^n}{\Delta t} + O((\Delta t)^2) \end{cases} \tag{2.13}$$

Avoiding the second-order $O((\Delta)^2)$ terms, the error does not exceed than the squared increment; if Δx, Δy and Δz are inhomogeneous the error comes to the first order[6] $O((\Delta))$. The next step is to apply of this formalism to (2.1), considering the fourth equation we obtain:

$$\frac{\partial E_y}{\partial z} - \frac{\partial E_z}{\partial y} = \mu \frac{\partial H_x}{\partial t} + \sigma^* H_x \tag{2.14}$$

and substitute the partial derivatives yields to

$$\frac{1}{\mu_{i,j,k}} \left(\frac{E_y|_{i,j,k+\frac{1}{2}}^n - E_y|_{i,j,k-\frac{1}{2}}^n}{\Delta z} - \frac{E|_{i,j+\frac{1}{2},k}^n - E_z|_{i,j-\frac{1}{2},k}^n}{\Delta y} - \sigma_{i,j,k}^* H_x|_{i,j,k}^n \right) = \frac{H_x|_{i,j,k}^{n+\frac{1}{2}} - H_x|_{i,j,k}^{n-\frac{1}{2}}}{\Delta t} \tag{2.15}$$

[6] relevant where a subgridding is applied

where it is noticing that the terms on the left hand have field components computed at time step n whereas in the right hand the magnetic components is not computed yet (not stored in the memory) and it can be computed through a semi-implicit technique:

$$H_x|_{i,j,k}^{n} = \frac{H_x|_{i,j,k}^{n+\frac{1}{2}} - H_x|_{i,j,k}^{n-\frac{1}{2}}}{2} \tag{2.16}$$

and substituting in (2.15) yields

$$\begin{aligned} H_x|_{i,j,k}^{n+\frac{1}{2}} &= \left(\frac{1-\frac{\sigma^*_{i,j,k}\Delta t}{2\mu_{i,j,k}}}{1+\frac{\sigma^*_{i,j,k}\Delta t}{2\mu_{i,j,k}}}\right) H_x|_{i,j,k}^{n-\frac{1}{2}} + \left(\frac{\frac{\Delta t}{\mu_{i,j,k}}}{1+\frac{\sigma^*_{i,j,k}\Delta t}{2\mu_{i,j,k}}}\right) \cdot \\ &= \left(\frac{E_y|_{i,j,k+\frac{1}{2}}^{n} - E_y|_{i,j,k-\frac{1}{2}}^{n}}{\Delta z} - \frac{E_z|_{i,j+\frac{1}{2},k}^{n} - E_z|_{i,j-\frac{1}{2},k}^{n}}{\Delta y}\right) \end{aligned} \tag{2.17}$$

With the same procedure it is possible to obtain the other field components w.r.t (2.1):

$$\begin{aligned} H_y|_{i,j,k}^{n+\frac{1}{2}} &= \left(\frac{1-\frac{\sigma^*_{i,j,k}\Delta t}{2\mu_{i,j,k}}}{1+\frac{\sigma^*_{i,j,k}\Delta t}{2\mu_{i,j,k}}}\right) H_y|_{i,j,k}^{n-\frac{1}{2}} + \left(\frac{\frac{\Delta t}{\mu_{i,j,k}}}{1+\frac{\sigma^*_{i,j,k}\Delta t}{2\mu_{i,j,k}}}\right) \cdot \\ &= \left(\frac{E_z|_{i+\frac{1}{2},j,k}^{n} - E_z|_{i-\frac{1}{2},j,k}^{n}}{\Delta x} - \frac{E_x|_{i,j,k+\frac{1}{2}}^{n} - E_x|_{i,j,k-\frac{1}{2}}^{n}}{\Delta z}\right) \end{aligned} \tag{2.18}$$

$$\begin{aligned} H_z|_{i,j,k}^{n+\frac{1}{2}} &= \left(\frac{1-\frac{\sigma^*_{i,j,k}\Delta t}{2\mu_{i,j,k}}}{1+\frac{\sigma^*_{i,j,k}\Delta t}{2\mu_{i,j,k}}}\right) H_z|_{i,j,k}^{n-\frac{1}{2}} + \left(\frac{\frac{\Delta t}{\mu_{i,j,k}}}{1+\frac{\sigma^*_{i,j,k}\Delta t}{2\mu_{i,j,k}}}\right) \cdot \\ &= \left(\frac{E_x|_{i,j+\frac{1}{2},k}^{n} - E_x|_{i,j-\frac{1}{2},k}^{n}}{\Delta y} - \frac{E_y|_{i+\frac{1}{2},j,k}^{n} - E_y|_{i-\frac{1}{2},j,k}^{n}}{\Delta x}\right) \end{aligned} \tag{2.19}$$

$$\begin{aligned} E_x|_{i,j,k}^{n+\frac{1}{2}} &= \left(\frac{1-\frac{\sigma^*_{i,j,k}\Delta t}{2\epsilon_{i,j,k}}}{1+\frac{\sigma^*_{i,j,k}\Delta t}{2\epsilon_{i,j,k}}}\right) E_x|_{i,j,k}^{n-\frac{1}{2}} + \left(\frac{\frac{\Delta t}{\epsilon_{i,j,k}}}{1+\frac{\sigma^*_{i,j,k}\Delta t}{2\epsilon_{i,j,k}}}\right) \cdot \\ &= \left(\frac{H_z|_{i,j+\frac{1}{2},k}^{n+\frac{1}{2}} - H_z|_{i,j-\frac{1}{2},k}^{n+\frac{1}{2}}}{\Delta y} - \frac{H_y|_{i,j,k+\frac{1}{2}}^{n+\frac{1}{2}} - H_y|_{i,j,k+\frac{1}{2}}^{n+\frac{1}{2}}}{\Delta z}\right) \end{aligned} \tag{2.20}$$

$$\begin{aligned} E_y|_{i,j,k}^{n+\frac{1}{2}} &= \left(\frac{1-\frac{\sigma^*_{i,j,k}\Delta t}{2\epsilon_{i,j,k}}}{1+\frac{\sigma^*_{i,j,k}\Delta t}{2\epsilon_{i,j,k}}}\right) E_y|_{i,j,k}^{n-\frac{1}{2}} + \left(\frac{\frac{\Delta t}{\epsilon_{i,j,k}}}{1+\frac{\sigma^*_{i,j,k}\Delta t}{2\epsilon_{i,j,k}}}\right) \cdot \\ &= \left(\frac{H_x|_{i,j,k+\frac{1}{2}}^{n+\frac{1}{2}} - H_x|_{i,j,k-\frac{1}{2}}^{n+\frac{1}{2}}}{\Delta x} - \frac{H_z|_{i+\frac{1}{2},j,k}^{n+\frac{1}{2}} - H_z|_{i-\frac{1}{2},j,k}^{n+\frac{1}{2}}}{\Delta x}\right) \end{aligned} \tag{2.21}$$

$$
\begin{aligned}
E_z|_{i,j,k}^{n+\frac{1}{2}} &= \left(\frac{1-\frac{\sigma^*_{i,j,k}\Delta t}{2\epsilon_{i,j,k}}}{1+\frac{\sigma^*_{i,j,k}\Delta t}{2\epsilon_{i,j,k}}}\right) E_z|_{i,j,k}^{n-\frac{1}{2}} + \left(\frac{\frac{\Delta t}{\epsilon_{i,j,k}}}{1+\frac{\sigma^*_{i,j,k}\Delta t}{2\epsilon_{i,j,k}}}\right) \cdot \\
&= \left(\frac{H_y|_{i+\frac{1}{2},j,k}^{n+\frac{1}{2}} - H_y|_{i-\frac{1}{2},j,k}^{n+\frac{1}{2}}}{\Delta x} - \frac{H_x|_{i,j+\frac{1}{2},k}^{n+\frac{1}{2}} - H_x|_{i,j-\frac{1}{2},k}^{n+\frac{1}{2}}}{\Delta y}\right)
\end{aligned}
\tag{2.22}
$$

For the E_x, E_y and E_z the $\sigma E^{n+1/2}$ term due to the electric losses is evaluated by using a semi0implicit procedure such as (2.16). Equations (2.17), (2.18), (2.19), (2.20), (2.21), (2.22), with the boundary conditions, allow for the computation of the electric and magnetic fields from the previous values and from the surrounding magnetic and electric fields.

2.2 Numerical dispersion and stability

The FDTD causes a non-physical dispersion due to the propagation through the discrete lattice region. This affects the phase velocity of the modes occouring a deviation from c of a quantity that depends on the wavelength and by the direction of propagation within the grid. If the spatial resolution increases the dispersion significantly will decrease. Effects due to the numerical aether can originate distortion, delays. The numerical dispersion play a key role when an electrically large structure is modeled. In order to avoid these artificial dispersions first of all proper values for the spatial and time steps have to be choose. Considering the compact form of the Maxwell's equations for a source-free region with $\mu = 1$, $\epsilon = 1$, $\sigma = 0$ and $\sigma^* = 0$ we have

$$
\jmath\nabla \times (\mathbf{H} + \jmath\mathbf{E}) = \frac{\partial}{\partial t}(\mathbf{H} + \jmath\mathbf{E}) \tag{2.23}
$$

where $\jmath = \sqrt{-1}$ and introducing the complex vector $\mathbf{V} = \mathbf{H} + \jmath\mathbf{E}$ yields

$$
\jmath\nabla \times \mathbf{V} = \frac{\partial \mathbf{V}}{\partial t} \ . \tag{2.24}
$$

Being the region uniform linear and isotropic, considering a plane wave field:

$$
\mathbf{V}|_{i,j,k}^{n} = \mathbf{V_0} e^{t(\omega n\Delta t - \hat{k}_x i\Delta x - \hat{k}_y j\Delta y - \hat{k}_z k\Delta z} \tag{2.25}
$$

in the Yee stace-time lattice yields

$$
\begin{aligned}
\left[\frac{\hat{x}}{\Delta x}\sin\left(\frac{\tilde{k_x}\Delta x}{2}\right) + \frac{\hat{y}}{\Delta y}\sin\left(\frac{\tilde{k_y}\Delta y}{2}\right) + \frac{\hat{z}}{\Delta z}\sin\left(\frac{\tilde{k_z}\Delta z}{2}\right)\right] \times \mathbf{V}|_{i,j,k}^{n} = \\
= \frac{-\jmath}{\Delta t}\mathbf{V}|_{i,j,k}^{n}\sin\left(\frac{\omega\Delta t}{2}\right)
\end{aligned}
\tag{2.26}
$$

where the central finite differences have been used. Performing the operations in (2.26) the V_x, V_y and V_z are obtained by[7]

$$\left[\frac{1}{c\Delta t}\sin\left(\frac{\tilde{\omega}\Delta t}{2}\right)\right]^2 = \\ = \left[\frac{1}{\Delta x}\sin\left(\frac{\tilde{k_x}\Delta x}{2}\right)\right]^2 + \left[\frac{1}{\Delta y}\sin\left(\frac{\tilde{k_y}\Delta y}{2}\right)\right]^2 + \left[\frac{1}{\Delta z}\sin\left(\frac{\tilde{k_z}\Delta z}{2}\right)\right]^2 \tag{2.27}$$

For a 1-D plane waves $\tilde{k}$ is given by

$$\tilde{k} = \frac{2}{\Delta}\arcsin\left(\frac{\Delta}{c\Delta t}\sin\left(\frac{\omega\Delta t}{2}\right)\right) \ . \tag{2.28}$$

The relationship between the phase velocity and the wavenumber is

$$\tilde{v}_p = \frac{\omega}{\tilde{k}} \tag{2.29}$$

and it points out how the spatial resolution influences the numerical phase velocity. Defining the cell density per wavelength as

$$N_y = \frac{\lambda}{\Delta} \tag{2.30}$$

that represents a kind of transition factor between continuous and discrete electromagnetic region. Empirically a good choice is $N_y = 20$, so the inaccuracy provided by the numerical dispersion can be negligible if

$$\Delta \leqslant \frac{\lambda_{min}}{20} \ . \tag{2.31}$$

Equation (2.28) shows a key parameter for this method, the Courant number

$$S = \frac{c\Delta t}{\Delta} \tag{2.32}$$

In order to choose Δt we consider (2.27) and solve it for $\tilde{\omega}$

$$\tilde{\omega} = \frac{2}{\Delta t}\arcsin(\xi) \tag{2.33}$$

where

$$\xi = c\Delta t\sqrt{\frac{1}{(\Delta x)^2}\sin^2\left(\frac{\tilde{k_x}\Delta x}{2}\right) + \frac{1}{(\Delta y)^2}\sin^2\left(\frac{\tilde{k_y}\Delta y}{2}\right) + \frac{1}{(\Delta z)^2}\sin^2\left(\frac{\tilde{k_z}\Delta z}{2}\right)} \tag{2.34}$$

From (2.34)

$$0 \leq \xi \leq c\Delta t\sqrt{\frac{1}{(\Delta x)^2} + \frac{1}{(\Delta y)^2} + \frac{1}{(\Delta z)^2}} \equiv \xi_{limit} \tag{2.35}$$

[7] setting the determinant of the system equal to zero

The maximization of ξ is obtained by:

$$\begin{aligned} \tilde{k}_y &= \pm\frac{\pi}{\Delta x} \ , \\ \tilde{k}_x &= \pm\frac{\pi}{\Delta y} \ , \\ \tilde{k}_z &= \pm\frac{\pi}{\Delta z} \ . \end{aligned} \tag{2.36}$$

If ξ exceed the unity due to Δt, the numerical wavenumber becomes complex driving to the instability [16], yielding a multiplicative factor $(\Delta t)^{-n}$ in (2.25). The stability condition is given by

$$\xi_{limit} \leq 1 \tag{2.37}$$

hence

$$\Delta t \leq \frac{1}{c\sqrt{\frac{1}{(\Delta x)^2}+\frac{1}{(\Delta y)^2}+\frac{1}{(\Delta z)^2}}} \ . \tag{2.38}$$

For a cubic cell[8]

$$\begin{aligned} \Delta t \leq \frac{1}{c\sqrt{\frac{1}{(\Delta)^2}+\frac{1}{(\Delta)^2}+\frac{1}{(\Delta)^2}}} &= \frac{\Delta}{c\sqrt{3}} \\ S = \frac{c}{\Delta}\frac{\Delta}{c\sqrt{3}} &= \frac{1}{\sqrt{3}} \end{aligned} \tag{2.39}$$

and the stability factor S is

$$S = \frac{c}{\Delta}\frac{\Delta}{c\sqrt{3}} = \frac{1}{\sqrt{3}} \ . \tag{2.40}$$

There will be divergence if $S > 1$.

Moreover, after the choice of the cell size the domain is going to be discretized but obviously it is impossible to consider an infinite domain. The domain of computation must be truncated, to this purpose have been developed some techniques available in the literature. The grid truncation is known as absorbing boundary conditions (ABC) problem and the most common are the Mur's ABS [34] and the perfectly matched layer (PML) formulations. Despite the PML, introduced by Berenger, is more complicated than others is better in terms of performance [35–37].

The choice of the "shape"[9] of cells for the mesh is a key feature when the FDTD will be implemented. The simplest choice is to consider cubic cells (uniform mesh) in order to facilitate the implementation of the FDTD code and in addition to make the FDTD execution faster w.r.t. other configuration, i.e. subgridding [38, 39], non-cubic cells [40]. The finer the cell size the better approximation of the objects but implies a longer computational time e.g. in a 3-D domain a cell size reduced by a factor 2 corresponds to an increment of 8 times the memory needed and 16 times the computational time [41]. The cell size must be smaller enough in order to avoid anisotropy issues and of course

[8] $\Delta x = \Delta y = \Delta z$

[9] cubic, hexagonal, non-orthogonal, etc.

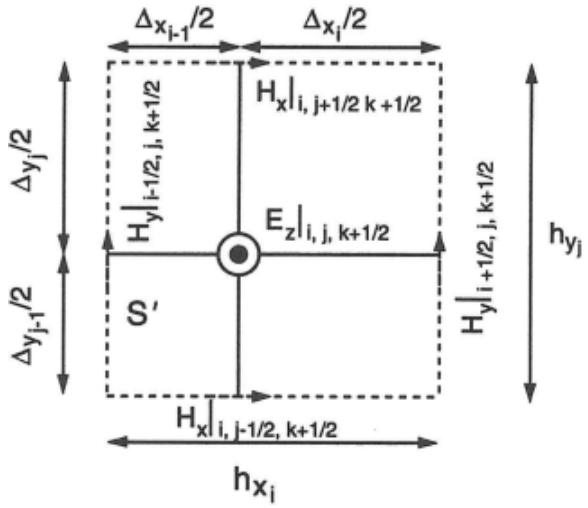

FIGURE 2.3: Example of non-uniform orthogonal cubic cell.

to respect the stability criterion. Therefore, it is obvious that subgridding a defined region or all the domain yields a finer resolution and allows to take into account variations of the structure that occurs within the (desired) Yee cells [42]. This involves to increase (drastically for big domain) the complexity of the code and the computational burden, i.e. memory requested, time step reduced means greater computational time, stability problem, etc. On the contrary, the subgridding or a non-uniform mesh arises necessary when the geometry details have to be modeled (locally or global). Many works in the literature are addressed on the study of these techniques, or a combination of them, i.e. the discontinuous-Galerkin time-domain (DGTD) [43–50]. Our FDTD code is implemented by using uniform cubic cells (staircase approximation), note that the accuracy of the method discussed previously does not include the inaccuracies introduced by the mesh [51, 52].

2.3 Code implementation

Basically, our homemade code[10] (that implements the FDTD) simulates the whole RC and is divided in three modules gathered in a single *job*. The three modules are:

1. the electromagnetic solver (the FDTD technique)
2. the Fast Fourier transform (FFT)[11] in order to obtain the frequency domain behavior
3. the statistical module, which is used to obtain the RC features, i.e. number of uncorrelated stirrer position/frequencies/spatial points, field uniformity, etc.

[10] developed by our group during these years

[11] On the FERMI/MARCONI supercomputer is available the FFTW library (http://www.fftw.org/) in order to perform the FFT

The code accounts well for the received power of the antennas (both T_x and R_x) because transmission lines are simulated connected to the antennas [16, 53] and it allows to recover the scattering parameters (S_{21} and S_{11}). In the simulations the

The cavity was excited by a Gaussian pulse modulated by a sinusoid, in order to cover the all band with a single FDTD simulation. The pulse excitation is:

$$V(t) = Ae^{\frac{(t-t_0)^2}{2\sigma^2}}\sin(\omega t) \tag{2.41}$$

where

$$\sigma = \frac{\sqrt{6}}{\pi(f_{max} - f_{min})} \tag{2.42}$$

and A indicates the amplitude of the pulse whereas $\omega = \pi(f_{max} - f_{min})$ with respect to the minimum and maximum frequency values set on the simulation. The FFT was evaluated by a step $\Delta f \approx 38$ kHz.

The FDTD is an electromagnetic solver well suited for a parallel implementation, such as the computation of the six components of the electromagnetic field. Moreover, the RC as well could be interpreted in a parallel way. In fact, considering a mode stirred RC, each stirrer position corresponds with a chamber realization, consequently each realization is a single *run* on the code, and obviously, each run is independent of the others. In parallel computing this structure is called "embarrassingly parallel", which means that little efforts are needed to divide the whole problem into many parallel tasks and the communication between these parallel tasks is very limited. In particular:

- in the time-domain(when FDTD and FFT were performed), each stirrer position can run on a different MPI process, (are independent by the stirrer position)
- in the frequency domain (when statistical analysis were performed), each frequency can run on a different MPI process (each frequency block is independent)

Each MPI process correspond to a single node on the old machine (FERMI), whereas in the new machine (MARCONI) we are able to increase the number of MPI processes in each node, in our case, after some attempts we fixed four MPI processes for each node. Subsequently, inside each node the FDTD was parallelized again by using OpenMP in order to compute the electromagnetic field values. Therefore the FDTD C-code is hybrid, using both MPI and OpenMP. Here is reported piece of the FDTD code used to compute the magnetic field:

```
/* COMPUTE THE MAGNETIC FIELD */
void
compute_h (struct_fieldEM * field, struct_fdtd * fdtd, struct_grid * grid)
{
  register int i, j, k;
  #pragma omp parallel for default(none) \ shared(griglia, campo, fdtd) \ private(i,j,k) \ num_threads(RCFDTD_THREADS)



 for (i = 0; i < grid->dimxm1; i++)
  for (j = 0; j < grid->dimym1; j++)
   for (k = 0; k < grid->dimzm1; k++)
   {
    field->Hx[i][j][k] += (fdtd->coef4z_1[k] * (field->Ey[i][j][k + 1] - field->Ey[i][j][k])) -
                          (fdtd->coef4y_1[j] * (field->Ez[i][j + 1][k] - field->Ez[i][j][k]));
```

```
    field->Hy[i][j][k] += (fdtd->coef4x_1[i] * (field->Ez[i + 1][j][k] - field->Ez[i][j][k])) -
                          (fdtd->coef4z_1[k] * (field->Ex[i][j][k + 1] - field->Ex[i][j][k]));

    field->Hz[i][j][k] += (fdtd->coef4y_1[j] * (field->Ex[i][j + 1][k] - field->Ex[i][j][k])) -
                          (fdtd->coef4x_1[i] * (field->Ey[i + 1][j][k] - field->Ey[i][j][k]));
  }
}
```

24 where *#pragma* denotes OpenMP directives.

In our code it is possible to arrange the data (field values picked up on the WV) in a 3-D array considering different chamber's realizations, Figure 2.4. In this way by using the

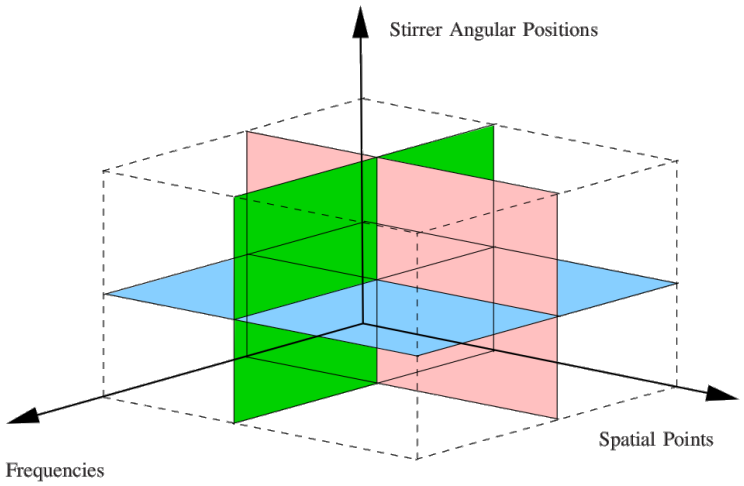

FIGURE 2.4: Scheme of the data arranging in the code implemented by Ancona's group. Angular positions are the stirrer positions/steps whereas spatial points are a defined number of points defined within the WV.

multivariate approach [32] where choosing and combining two of the three realizations it is possible to evaluate the third as:

- the uncorrelated stirrer positions adopting:
  - spatial correlation matrix (for each frequency)
  - frequency correlation matrix (for each spatial point)
- uncorrelated spatial points adopting:
  - spatial correlation matrix (for each stirrer position)
  - stirrer position correlation matrix (for each spatial point)
- uncorrelated frequencies adopting:
  - stirrer position correlation matrix (for each frequency)
  - frequency correlation matrix (for each stirrer position).

2.4 Effect of losses

Losses of an RC can be caused by many mechanisms [19] such as antenna losses originated by the antenna total efficiency [54,55], losses of the walls due to the finite conductivity, leakages in joints/screws/door, losses due to the antenna's tripod, cable inserted to connect antennas to the VNA ports, devices under test (DUTs), rubber cable jackets, finner stirrer conductivity. Localized losses are difficult to take into account in a rigorous way and not efficient in numerical simulations. Moreover, the discretization of the whole chamber and devices with uniform cells does not assist to well account the localized losses in objects with a complex geometry. It is more convenient consider distributed losses with an effective equivalent conductivity σ_v, it facilitates not only the implementation of the problem but also improves the efficiency and performance when the code run on supercomputers [56,57]. In fact, for the wall losses we have to consider the existing relationship between the tangential components of electric and magnetic field:

$$\mathbf{E_{tan}} = Z_s \mathbf{J_s} = Z_s \mathbf{n} \times \mathbf{H_{tan}} \tag{2.43}$$

then, considering a good conductor with σ_w the internal impedance is

$$Z_s \simeq \sqrt{\frac{j\omega\mu}{\sigma_w}} = R_s + j\omega L_s \tag{2.44}$$

where the resistance of the surface is

$$R_s \omega L_s = \frac{1}{\sigma_w \delta} \tag{2.45}$$

and

$$\delta = \frac{1}{\sqrt{\pi f \mu \sigma_w}} \tag{2.46}$$

is the skin depth. At a fixed frequency both R_s and L_s can be treated as a constant and applying the inverse Fourier transform (IFT) we get the time-domain FDTD constant surface impedance boundary conditions [16]:

$$\mathbf{E_{tan}}(t) = \left(R_s + L_s \frac{\partial}{\partial t} \right) \mathbf{n} \times \mathbf{H_{tan}}(t) \, . \tag{2.47}$$

that was implemented in [58] and the advantages of this method are: ease and velocity. For a broadband excitation this method returns the exact value at the considered center frequency [59]. On the contrary, in our code walls and objects are simulated as perfect ideal conductor (PEC) $(E_{tan} = 0)$. This choice permits to maximize the speed up of the code and to simplify the accounting of losses, now distributed losses within the volume of the RC, call it volumetric losses which a conductivity: σ_v. The conductivity (σ_v) of each FDTD cell could be set to the chosen value. This procedure is included in the FDTD development and it does not need more computational resources [16].

As shown in [60, 61], losses could be taken into account in a temporal simulation

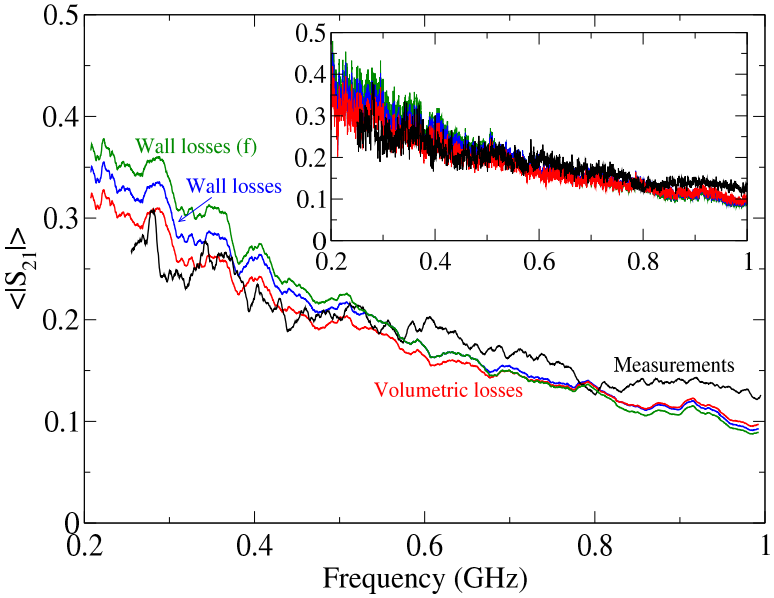

FIGURE 2.5: Simulated transmission coefficient amplitude S_{21} of the measurement (black) simulation with both wall (blue) wall with frequency dependence (green) and volumetric (red) losses. A sliding average window over 40 and 400 frequency points was applied for the measured and simulated data respectively, main graph whereas the inset reports raw data.

by tailored filter applied to the response of a lossless cavity, previously evaluated by an FDTD simulation. Moreover, wall losses should be evaluated for each frequency over the whole band, this is another weakness of this choice.

In this thesis, apart where specified, results were obtained by using volumetric losses, and simulate walls, stirrers, antennas (discone) and spheres as (PEC). The staircase approximation weakly affects the reflection coefficient of antennas because the wavelength is greater than the cell size, i.e. $\lambda/20$ at 0.5 GHz (related to the following simulated results). Despite we considered volumetric losses in the simulations, a comparison between the use of wall and volumetric losses were done [62, 63]. Values for the two conductivities were evaluated with different procedures. It was not applied a rigorous procedure in order to reach the best fit value for σ_v (compared to the experimental results), but several attempts were done until the "best" value was reached, just by a visual inspection [64]. For our chamber (Ancona's RC) the values of the conductivities are: $\sigma_w = 5000$ [S/m] and $\sigma_v = 10^{-5}$ [S/m] for wall and volumetric losses respectively.

In Figure 2.5 it is reported the comparison between simulated and measured S_{21} of Ancona's RC. The measurement is the black curve, whereas the others are from simulations. In particular the red curve was obtained by considering volumetric losses, the blue for wall losses considering the constant surface impedance and the green[12] curve again wall losses but evaluated with a variable surface impedance. Resistance and inductance of (2.47) were evaluated at the center frequency (blue curve) but actually they are frequency dependent. For a better evaluation the whole band was divided in five

[12] obtained by concatenating the considered subbands, Table 2.1

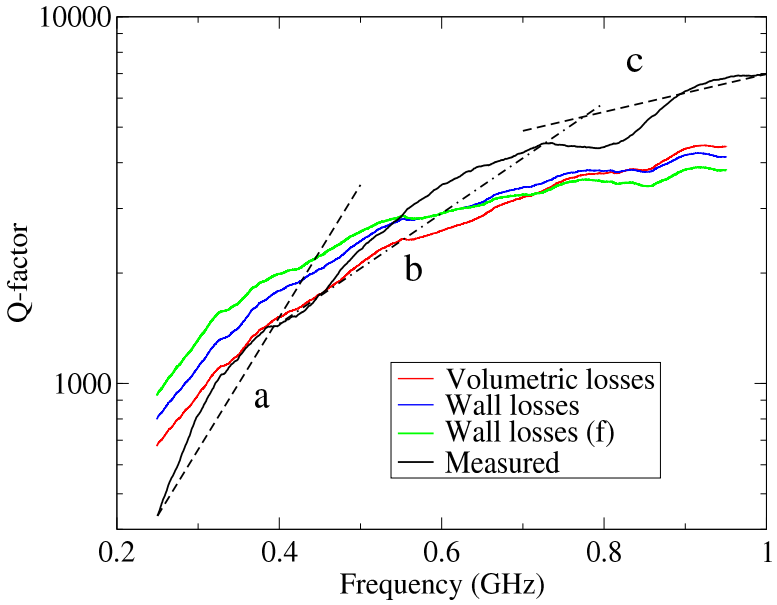

FIGURE 2.6: Comparison of the Q-factor. Dashed lines represent the theoretical proportional frequency law of the Q-factor (w.r.t. our values). In particular, the a segment represents the f^3 trend, the b segment follows a f^2 trend and the c segment a linear behavior with the frequency f.

TABLE 2.1: Subbands and intermediate frequency for parameter evaluations.

Band (MHz)	f_0 (MHz)
200–375	300
375–525	450
525–675	600
675–825	750
825–1000	900

subbands reported in Table 2.1. It is worth noticing that in order to obtain "best" results (more accurate) the R_s and L_s should be evaluated for many frequencies, this choice increases the complexity and time of simulations. However, Figure 2.5 points out that volumetric losses fit quite well the experimental data, the value of the equivalent conductivity is $\sigma_v = 10^{-5}$ [S/m][13]. Indeed, the blue and green curve are perfectly overlapped at 600 MHz, in fact in blue curve the R_s and L_s were evaluated at the fixed frequency of 600 MHz and a conductivity of 5000 [S/m].

One of the most parameter used to evaluate if the distributed losses is an acceptable approach is the Q-factor. Figure 2.6 reports the Q-factor evaluated by the three methods and compared to the experimental results. Curves match well at about 600 MHz, the frequency chosen for the evaluation of σ_w. The plot also reports the slope of the

[13] this value was retrieved after several attempts

Q-factor, $\approx f^3$ at low frequency (antenna's losses are dominant), further the slope reduces to f around 1 GHz whereas wall losses dominates at high frequency[14] and the slope approaches to $\sqrt{f}$. The slope of obtained (simulated) Q-factor follows the slope of experimental results both at low frequency and high frequency.

These results show that the use of equivalent volumetric losses (distributed within the volume of the chamber) is acceptable artifact w.r.t. the use of wall losses that allows to improve the simulations performance on supercomputers.

[14] for Ancona's chamber at frequencies much higher than 1 GHz)

Chapter 3

Chaotic reverberation chamber

The RC, as previously introduced in previous Chapter 1, is widely used in EMC tests. The smallest dimension of the cavity is larger w.r.t. the minimum wavelength at the LUF. Depending on the type of test (and devices under test – DUTs) the LUF is a constraint that must be satisfied in order to meet the operational requirements [11] to ensure a reliable test. The main efforts during these years were focused to improve the RC's behavior, i.e. an existing large chamber that has to well operate close or better just below the LUF.

There are different possibilities in order to attain this purpose:

- improve the stirring performance, with a proper design of stirrer/s with specific shape and dimension
- by using more stirrers or mixing more stirring techniques at the same time
- deforming the shape/geometry of the chamber
- enlarge the dimensions of the RC, but obviously it is not the best solution.

This chapter initially treats a brief introduction to the quantum chaos where deformed cavity was studied [65–68]. Afterwards a brief description of the most relevant works available in the literature and then simulated results obtained during the last two years (partially spent at the University of Nottingham, UK) of hard work are reported.

The earlier idea was concentrated to characterize chaotic[1] cavity by the presence of curved diffractors (spheres) just as function of their radius. Meanwhile new results came out, it was noticed that not only the dimensions play a relevant role about the evaluation of the new geometry. Others parameters must be taken into account during the analysis, i.e. the placement inside the chamber, the kind of diffractor and losses introduced by them.

3.1 A brief introduction to the quantum chaos

The quantum chaos studies dynamical systems in terms of the quantum mechanics, which describes the behavior of the matter into the molecular and atomic (sub-atomic) levels. In fact, the quantum chaos approach is applied in the study of molecular, atomic

[1] the adjective "chaotic" means: derived by structure studied in the quantum chaos literature

and nuclear systems as well as microwave resonators, where energy levels play an important role to the characterization/study of these systems, e.g. evaluating the statistics of energy levels. According to the quantum mechanics, energy levels are described by the eigenvalues of a Hermitian operator H [69], more precisely called Hamiltonian. The Hamiltonian is represented by a matrix with finite dimension.

By the following equation:

$$H\psi_i = E_i\psi_i \tag{3.1}$$

it is possible to evaluate eigenvalues and eigenfunctions of the system. This operator (H) is represented by a matrix filled by random variables belonging to a predetermined distribution with appropriate statistical hypotheses.

We can have the Poisson distribution

$$p(s)ds = e^{-s}ds \tag{3.2}$$

where $s = S/D$ is the relative mean spacing [69]. Afterwards is reported just few words for a better comprehension about the statistics of energy levels. Considering the the energies $E_1, E_2, ...$ of the system in the interval δE with $E_1 \leqslant E_2$, and $S_1, S_2, ...$ their distances, we have $S_i = E_{i+1} - E_i$; whereas D denotes the mean spacing, namely the average value of S_i; we can define the relative spacing as $s_i = S_i/D$. The probability density function $p(s)$ could be defined as the probability $p(s)ds$ that any spacing s_i will have a value between s and the next spacing $s+ds$. When the positions of energy levels are not correlated the probability that any E_i will be within E and $E+dE$ is independent of E and is $\rho\, dE$, where $\rho = D^{-1}$ represents the average number of levels in a unit interval of energy. Then, to establish the probability of a spacing S given at the level E we want to evaluate the probability of having no level in the interval $(E, E+S)$ and one level in the interval $(E+S, E+S+dS)$. To this purpose the S interval is divided into n parts, equals each others, Figure 3.1. Due to the independence of levels, the probability of having no levels in $(E, E+S)$ is given by the product of probabilities of no having no level in any of these n parts.

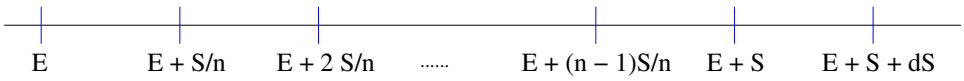

FIGURE 3.1: Energy interval divided in n parts.

For a large n, the ratio (S/n) becomes small and we can write $(1-\rho S/n)^n$ and its limit for $n \to \infty$ is

$$\lim_{n\to\infty}\left(1-\rho\frac{S}{n}\right)^n = \mathrm{e}^{-\rho S}\ . \tag{3.3}$$

Therefore, the probability that a level in dS at $E+S$ is given by $\rho\, dS$, whereas considering an E level, the probability that there is no level in $(E, E+S)$ and one level in dS at $E+S$ is

$$e^{-\rho S}\rho\, dS \tag{3.4}$$

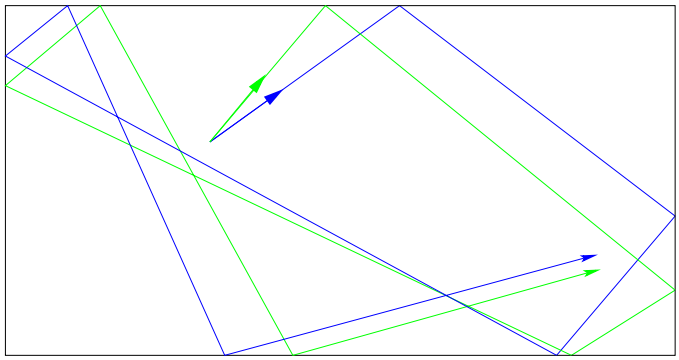

FIGURE 3.2: Sketch of a 2-D regular cavity.

or equivalently

$$p(s)ds = e^{-s}ds \tag{3.5}$$

as defined previously the Poisson distribution.

Hamiltonian classic systems (regular) which are integrable follow the Poisson distribution. Conversely, if a system (chaotic) displays a classical chaos behavior, it follows a Wigner distribution. The Wigner probability density function for a spacing is:

$$p(s) = \frac{\pi s}{2} e^{-\frac{\pi}{4}s^2} \tag{3.6}$$

where s is the relative spacing defined as S/D.

In this field the RMT [69–71] plays a key role because the statistical properties of many systems without a defined Hamiltonian could be predicted by using random matrices using an appropriate distribution. Moreover, RMT could also be useful in order to predict the statistical properties of eigenvalues of chaotic systems with a know Hamiltonian.

Physicists have been studied properties of these systems [13, 65, 72–78], where the shape of the cavity or enclosure was modified. The new geometry improves the field disorder within it, because the non-parallel walls permits to break the symmetry, in terms of ray's trajectories.

In fact, inside a regular (rectangular) cavity the rays follow a close path each other, due to the reflection by walls. On the contrary, in a chaotic cavity rays have a greater random incidence and after a certain number of reflections the whole volume of the cavity will be covered; this behavior is called ray's divergence. As example in Figure 3.2 is reported a 2-D regular cavity (same issue for a 3-D cavity) where two rays, starting from the same point inside the cavity, were launched at slightly different direction remain close each other geometrically, this involves that only certain region will be filled and the energy remain localized.

Modifying the shape of the cavity, i.e. tilting their walls as reported in Figure 3.3, the same rays reported in the previous case (launched at slightly difference from the same starting point) now they exhibit a chaotic behavior, the rays diverge geometrically and the energy will be spread over the whole volume of the cavity after a certain number of reflections, Figure 3.7. Figure 3.7 shows a typical chaotic system where alternation of

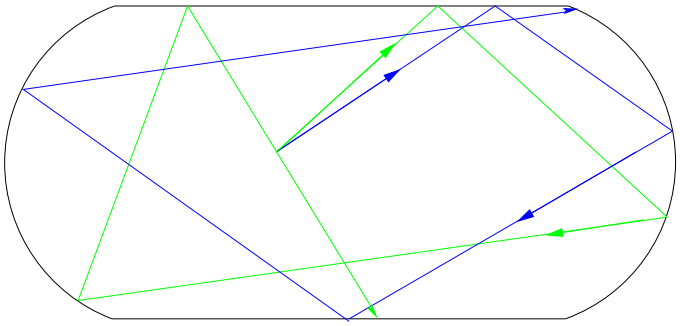

FIGURE 3.3: Sketch of a 2-D chaotic cavity where two walls were tilted in order to improve the ray's divergence.

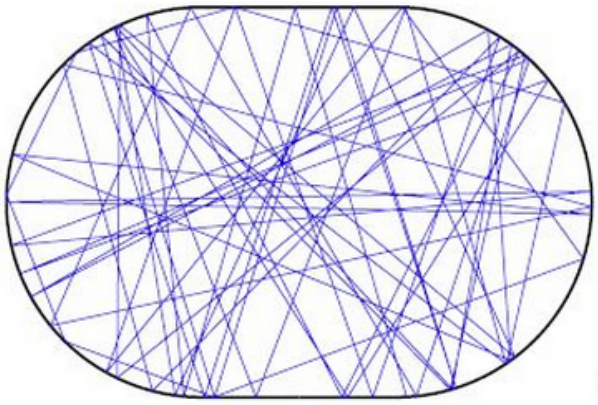

FIGURE 3.4: Sketch of 2-D chaotic dynamical system after a certain number of ray's reflections.

straight and non-straight reflection come in succession.

The Hamiltonian (3.1) of billiards can by substituted by the stationary-state Schrödinger equation

$$-\frac{\hbar}{2m}\nabla^2\psi_n(q) = E_n\psi_n(q) \tag{3.7}$$

where ∇ is the Laplacian operator, ψ the wave function (orthonormal) at the point q, m the mass of the system and $\hbar$ the Planck constant ($\hbar = h/2\pi$). The Dirichlet boundary conditions define:

$$\psi_n(q) = 0 \text{ for } q \notin \Omega\,. \tag{3.8}$$

The free-field Schrödinger equation coincides with the Helmholtz equation

$$\left(\nabla^2 + k^2\right)\psi = 0 \tag{3.9}$$

where $k^2 = \frac{1}{\hbar}2mE_n$.

We can note that for a 2-and-3D billiards with an integrable equation of the motion, the quantum mechanical billiards system can be evaluated. On the contrary, for a chaotic classical system it will not be exactly evaluated and its behavior will be study by the quantum chaos, that identifies the statistical feature of these systems. In particular, chaotic systems exhibit universal properties, i.e. regular and chaotic dynamical

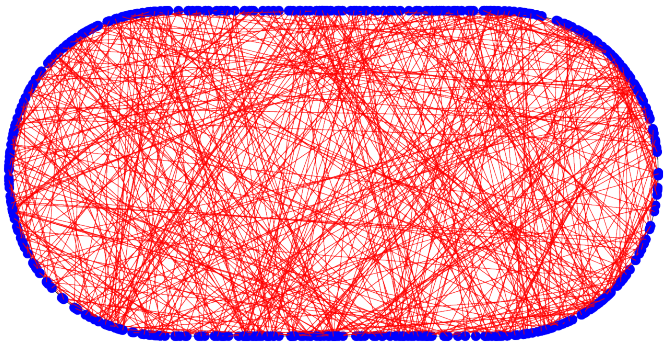

FIGURE 3.5: Sketch of 2-D chaotic dynamical system called Bunimovich stadium, temporal picture after more reflections than depicted in Figure 3.4.

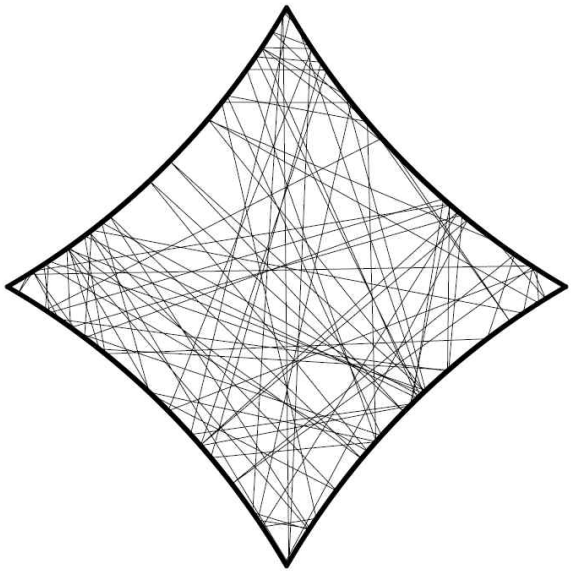

FIGURE 3.6: Example of 2-D chaotic system.

behavior of the underlying classical limit, [12, 79–81].

There were studied many interesting configurations of dynamical systems, i.e. mushroom billiard [82], Sinai billiard [83, 84] and so on.

3.2 Introduction to the chaotic cavities

The frequency range for a well stirred RC is considered above a predetermined limit that corresponds to the LUF (see Chapter 1) and its referred to the value of the fundamental mode of the cavity, given by

$$f_{l,m,n} = \frac{1}{2\sqrt{\mu\epsilon}}\sqrt{\left(\frac{l}{a}\right)^2\left(\frac{m}{b}\right)^2\left(\frac{n}{c}\right)^2} \tag{3.10}$$

where indexes l, m, n that indicate the modes whereas a, b, c represent the dimensions of the cavity; length, width and height respectively. From (3.10) the wavenumber (k) can

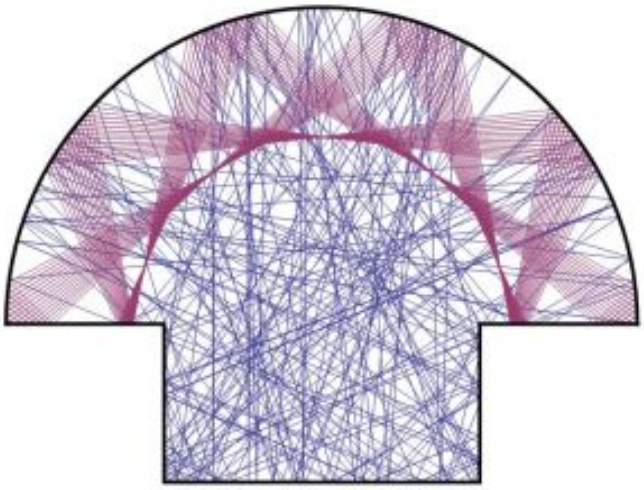

FIGURE 3.7: Example of 2-D chaotic system: mushroom billiard.

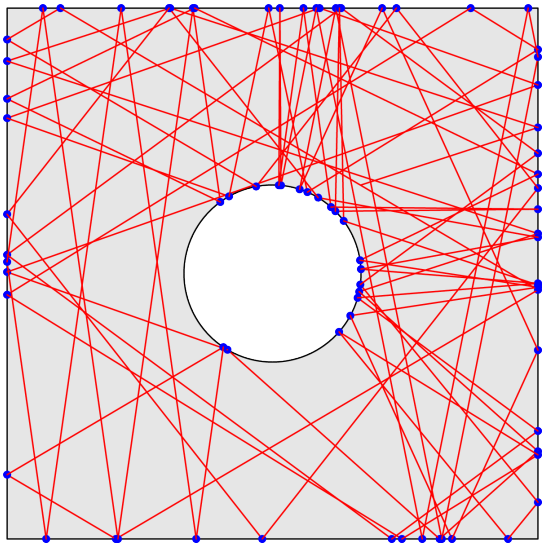

FIGURE 3.8: Example of 2-D chaotic system: Sinai billiard.

be obtained by the relationship $k = 2\pi f / c$, (1.46). For the Ancona's RC the fundamental mode is $f_{1,1,0} = f_0 \approx 45$ MHz. At high frequency, enough far from the LUF, the field will be certainly ergodic.

The idea of improve performance of a rectangular (quasi-cubic) RC was the purpose of several works during past years, in particular focusing at low frequency [23, 85]. In order to achieve this intent many solutions have been explored, i.e. add diffusers within the cavity, design a new shape. A first approach was similar to the solution adopted in acoustic, where the Schroeder diffusers were inserted into the room. The aim of acoustic diffusers is to create an optimal and predictable diffusion of sound waves due to the reflection attained by means of an accurate design of them [86]. As showed in Figure 3.9, the Schroeder diffuser is a structure made by "holes" of different depths; the sound-waves hit the irregular surface of diffusers and they bounce out of each "holes" at slightly time. The dimension of diffusers determine the operating frequency of the structure.

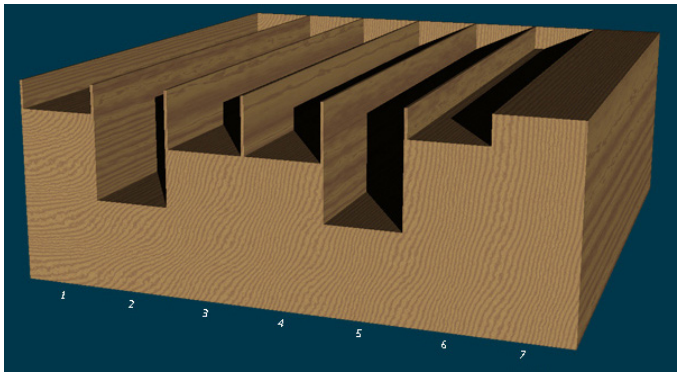

FIGURE 3.9: Example of Schroeder diffuser with seven cells, each of them with different depth.

This kind of diffusers were adopted also in the electromagnetic chamber in order to improve the field diffusion within the RC, i.e. in [87–89]. In addition to the use of acoustic diffusers, another explored solution to break the symmetry is to design a chamber without parallel walls [87, 88, 90].

The mode density of an electromagnetic lossless cavity is given by the generalized Weyl's law [91–95]:

$$\frac{dN(f)}{df} = \frac{8\pi V}{c}\left(\frac{f}{c}\right)^2 - \left[\frac{4}{3\pi}\iint_{S=\partial V}\frac{ds}{\rho(r)} - \frac{1}{6\pi c}\int_{L=\partial S}\frac{[\pi-\varphi(r)]\,[\pi-5\varphi(r)]}{\varphi(r)}dl\right] \tag{3.11}$$

where the variation of modes $dN(f)$ within a frequency interval df depends on the radius of the curvature $\rho(r)$ of the surface element ds which a radius r for an angles ϕ and θ (in spherical coordinates). In [23] was studied the effect of convex, rounded and concave edges of a cavity, in order to facilitate a design of diffractors for a practical use. It was showed that when the modal density increases there will be a lower shift of the "threshold" from the region with a weak modal overlap to the region of moderate overlap. Considering the input due to the quantum chaos, it is possible design other kind of diffractors. In particular spherical-shaped diffractors were analyzed in many papers [14, 23, 68, 73, 96–98]. The chaotic RC exhibit an improvement of their performance and consequently a reduction of the LUF could be possible [23, 96–100]. A rigorous creation for a physically-motivated definition of LUF are still to be achieved, and constitutes a relevant task to be obtained. During my Ph.D. i focused on effects due to the spherical diffractors. Conversely to other works there are two substantial differences w.r.t. my analysis:

- instead of RMT, FEM or commercial software here the FDTD method have been adopted
- the analysis was carried out by taking into account characteristic parameters used in the EMC instead of a pure physic approach already discussed in many works.

3.3 FDTD simulations

Simulations were performed by means of the FDTD. Figure 3.10 shows the setup of the Ancona's RC which has dimensions $6 \times 4 \times 2.5$ m^3. The investigated band is from 0.2 to 2.0 GHz and the cell size is 1.5 cm which corresponds to $\lambda/10$ at 2.0 GHz. Within the RC there are two discone antenna in order to get the transmission S_{21} and reflection S_{11} scattering parameters. The working volume (red box in Figure 3.10) is composed by 125 points each of them equispaced by 30 cm where field values were picked up. The area

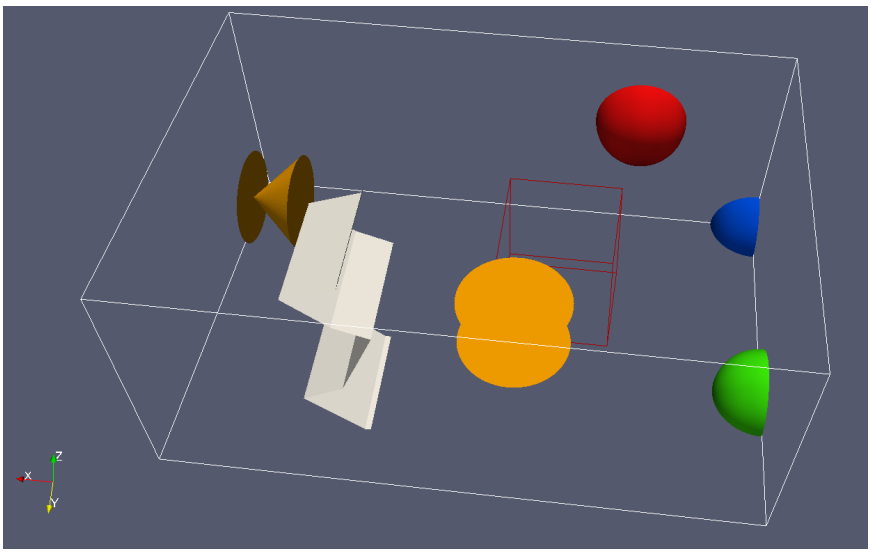

FIGURE 3.10: Setu-up of the simulated RC equipped by a z-folded vertical stirrer, two antennas T_x and R_x respectively and diffractors. The red box represents the working volume.

of the WV is $1.20 \times 1.20 \times 1.20$ m^3, which preserves the distance from the walls, antennas and diffractors reported in the standard [11]. The field mixing is due by a vertical z-folded stirrer, 256 positions have been considered; a shift of 1.4° for each step. Geometry of the rectangular chamber was modified by means of spherical diffractors (spheres). They can be placed in different position along the chamber's perimeter, on a corner (blue sphere), between two walls (green sphere) or on a single wall (red sphere) of the chamber, see Figure 3.10.

In addition to spherical diffractors it is possible to simulate other kind of diffractors, i.e. spherical caps or mushroom-shaped diffractors depending on the length of penetration through the RC.

For each kind of diffractor the proper volume and surface is computed by following formulas:

- hemisphere, Figure 3.11
- spherical cap, Figure 3.12
- spherical mushroom, Figure 3.13.

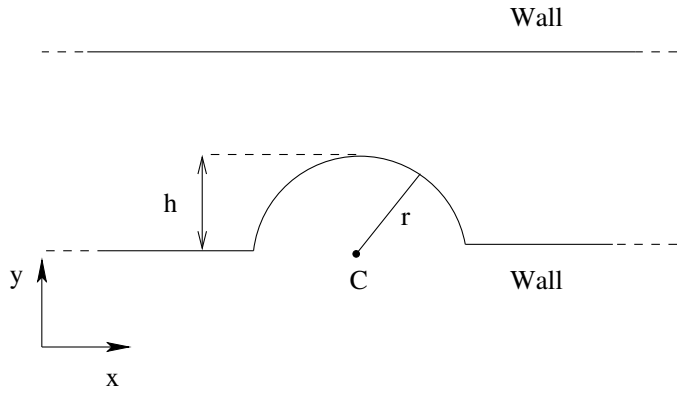

FIGURE 3.11: Kind of diffractor: hemisphere with $h/r = 1$. C indicates its center, r the radius and h the length of penetration through the RC.

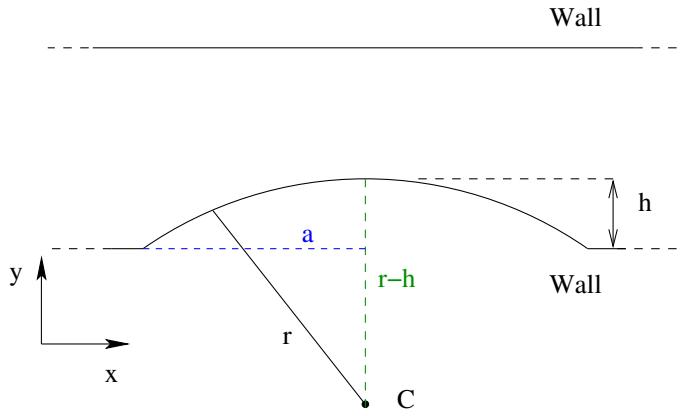

FIGURE 3.12: Kind of diffractor: spherical cap with $h/r < 1$. C indicated its center, r the radius and h the length of penetration through the RC.

Figure 3.15 shows a comparison between different kind diffractors. For a better comparison each of them was placed in the same position, i.e. on a wall of the chamber. As expected the mushroom-shaped diffractor exhibits a better performance in terms of uncorrelated frequencies, in fact this configuration has a larger penetration through the chamber and facilitates the field diffusion w.r.t. others configurations. In this thesis results are focused just on hemispheres, further analysis with spherical caps and mushroom is ongoing. Diffractors can be placed within the RC in different positions, see Figure 3.14, or a combination of them. In particular:

A) on a corner – corresponding to an eighth of the whole sphere

B) between two walls – corresponding to a quarter of the whole sphere

C) on a wall – corresponding to half sphere.

Of course, it is possible to simulate a whole sphere within the RC, but this configuration was discarded because it is not a practical choice for real test when DUT will be insert in the WV.

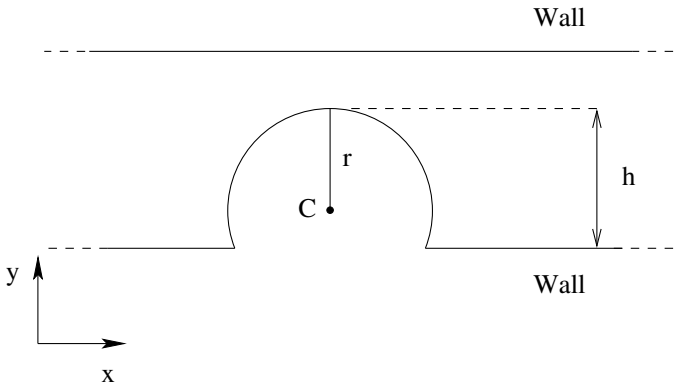

FIGURE 3.13: Kind of diffractor: spherical mushroom with $h/r > 1$. C indicated its center, r the radius and h the length of penetration through the RC.

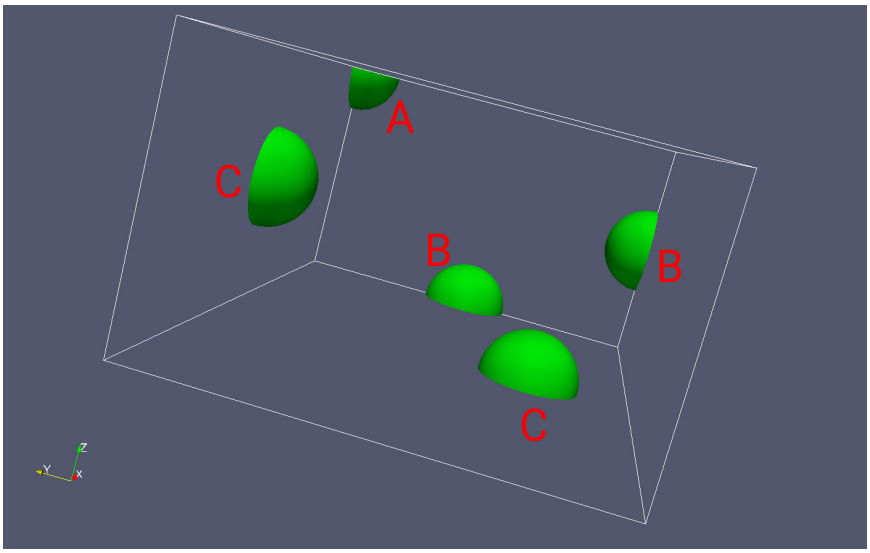

FIGURE 3.14: Possible ways where diffractors can be placed along the perimeter of the chamber.

Each position of spheres points out a different behavior, i.e. half sphere (on a wall) has higher impact on the performance w.r.t. a sphere on a corner or between two walls, as showed in Figure 3.16.

Different configurations of the loaded[2] chamber have been simulated, see Table 5.1. In the simulations spheres are centered far enough each others, means that they are not overlapped. Moreover, considering spheres only on a single wall of the RC, results showed that their placement along the wall do not affect the behavior but taking care that they do not overlap each others and they have to maintain their shape, i.e. half sphere must not become an eighth or quarter of sphere, Figure 3.17.

After a first and brief evaluation we are going to deeply analyses how diffractors affect the modal density and the characteristic parameter of the RC for a practical use, i.e. uncorrelated stirrer positions, field uniformity (σ_{24}). Moreover, adding objects inside

[2] by spherical diffractors

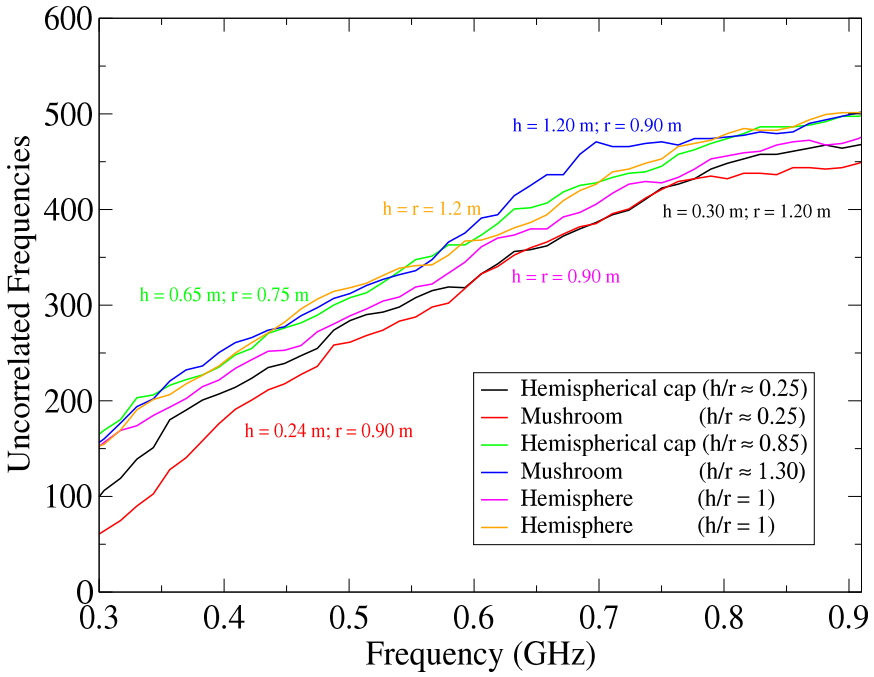

FIGURE 3.15: Comparison of different kind of diffractors, evaluated by the number of uncorrelated frequencies evaluated by means of the multivariate approach.

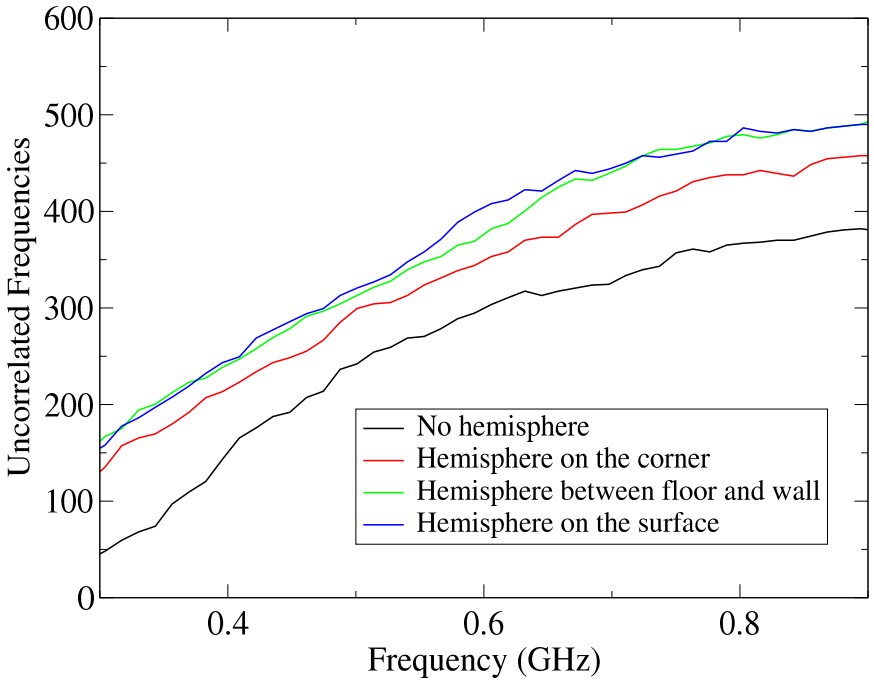

FIGURE 3.16: Number of uncorrelated frequencies for different positioning of a single hemisphere inside the RC evaluated by means of the multivariate approach.

the RC the Q-factor has to be evaluated. As showed in Chapter 1, the Q-factor can be evaluated:

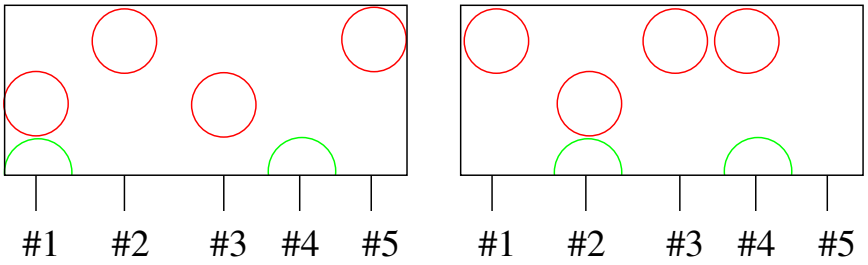

FIGURE 3.17: Different placement for the same number, dimension and type of spheres along the same wall of the chamber. The enumerations #1...#5 denote five centers for spheres.

TABLE 3.1: Table which reports the total number of diffractors (# indicates the ordinal counting), their radius, their placement inside the RC and the total volume and surface of the RC. Inserted spheres are not overlapped each others.

Label ID	# Diffractors	r (m)	# 1/8	# 1/4	# 1/2	Volume (m^3)	Surface (m^2)
Empty RC	0	//	/	/	/	60.0	98.00
A)	4	0.50	0	0	4	58.95	101.14
B)	10	0.50	2	4	4	58.29	102.31
C)	20	0.50	1	17	2	56.65	107.80
D)	30	0.50	4	18	8	55.45	110.50
E)	10	0.75	2	4	4	54.25	107.71
F)	8	1.00	0	4	4	47.43	116.84
G)	0	0	0	0	0	54.25	91.83
H)	0	0	0	0	0	47.46	82.88

- analytically by means of formulas for the composite Q-factor [101] (depending on dimension and position of spheres)
- numerically by means of full wave simulations.

Simulations are very useful and customizable[3] because it is possible to consider many configurations otherwise hard to realize in an experimental setup, i.e. simulate the RC with a large number of diffractors.

The Q-factor of a cavity is given to the contribute of more factors, see Chapter1. For numerical analysis the quality factor is computed by [11]:

$$Q = \frac{16\pi^2 V \left\langle |S_{21}|^2 \right\rangle}{\eta_{TX}\eta_{RX}\langle |S_{11}|^2\rangle\langle |S_{22}|^2\rangle}\left(\frac{f}{c}\right)^3 \tag{3.12}$$

with c the speed of light in the vacuum, V the volume of the RC, f the frequency, S_{21} is the complex scattering transmission coefficient, whereas S_{11} and S_{22} are the complex scattering reflection coefficients. The antenna efficency coefficients η_{Tx} and η_{Rx} for the transmitting and receiving antennas respectively, are ≈ 1 because well matched.

[3] a fortiori by using the homemade FDTD code of my group which allows us to implement "easily" new geometries

For analytical analysis when wall losses are dominant, the quality factor can be evaluated by:

$$Q = \frac{3V}{2S\mu_r\delta} \tag{3.13}$$

where V and S are the total[4] volume and total[5] surface of the RC respectively, δ is the skin depth and μ_r the relative magnetic permeability (equal to 1). The value of the conductivity used for analysis was $\sigma = 5000$ S/m (the same used in the FDTD setup when wall losses σ_w have been considered). Actually, the losses mechanism of antennas (dominant at low frequency) has to be considered, and is computed by:

$$Q_a = \frac{16\pi^2 V}{\lambda^3} \tag{3.14}$$

then the total Q-factor is given by

$$Q_{tot}^{-1} = Q^{-1} + Q_a^{-1} \ , \tag{3.15}$$

used later and called Q-model. Remarking that volume and surface of the deformed cavity have to be considered with geometrical corrections, that are known. In particular, keep in mind that the volume and surface of a sphere are $(4/3\pi r^3)$ and $(4\pi r^2)$ respectively, it is possible to compute the whole volume and surface of the chaotic RC by applying following formulas:

$$V^s = V^w - \alpha_i \frac{4}{3}\pi r_i^3 \tag{3.16}$$

and

$$S^s = S^w + \beta_{ai} 4\pi r_i^2 - \beta_{bi}\pi r_i^2 = S^w + \beta_{tot_i}\pi r_i^2 \tag{3.17}$$

where

$$\beta_{tot} = 4\beta_a - \beta_b \tag{3.18}$$

and i represents the $i-th$ sphere or cap, s (sphere) denotes the chaotic cavity and w (without spheres) the empty RC. The term α is a constant and depends by the portion of added volume whereas the term β_{tot} takes into account two different areas, β_a represents the surface added by a sphere whereas β_b the surface (of the chamber) removed (covered by the added sphere) when a sphere was inserted. Assuming that the inserted hemispheres have the same radius and they were placed in the same way i.e. on the corner of the chamber we set:

$$\begin{cases} r_1 = r_2 = r_3 = \cdots = r_n = r \\ \alpha_1 = \alpha_2 = \alpha_3 = \cdots = \alpha_n = \alpha \\ \beta_{a_1} = \beta_{a_2} = \beta_{a_3} = \cdots = \beta_{a_n} = \beta_a \\ \beta_{b_1} = \beta_{b_2} = \beta_{b_3} = \cdots = \beta_{b_n} = \beta_b \ . \end{cases} \tag{3.19}$$

[4] means that the reduction due to spheres is considered

[5] means that the increase and/or reduction due to spheres is considered

Considering k diffractors we can distinguish:

- Sphere on a corner (1/8 of the whole sphere):

$$\begin{cases} \alpha_i = \frac{1}{8} \Rightarrow \alpha = \sum_{i=1}^{k} \alpha_i \\ \beta_a = \frac{1}{8} \\ \beta_b = \frac{1}{4} \cdot 3 \\ \beta = \sum_{i=1}^{k} \beta_{tot_i} \end{cases} \tag{3.20}$$

- Sphere on a surface (1/4 of the whole sphere):

$$\begin{cases} \alpha_i = \frac{1}{2} \Rightarrow \alpha = \sum_{i=1}^{k} \alpha_i \\ \beta_a = \frac{1}{2} \\ \beta_b = 1 \\ \beta = \sum_{i=1}^{k} \beta_{tot_i} \end{cases} \tag{3.21}$$

- Sphere between two surfaces e.g. wall-wall or wall-ceiling/floor (1/2 of the whole sphere):

$$\begin{cases} \alpha_i = \frac{1}{4} \Rightarrow \alpha = \sum_{i=1}^{k} \alpha_i \\ \beta_a = \frac{1}{4} \\ \beta_b = \frac{1}{2} \cdot 2 \\ \beta = \sum_{i=1}^{k} \beta_{tot_i} \end{cases} \tag{3.22}$$

Those relationships are still valid with spherical cap or spherical mushroom, but the geometrical correction coefficients are different, in particular:.

- hemisphere:

$$V = \frac{4}{3}\pi r^3 \quad \text{and} \quad S = 4\pi r^2 \ , \tag{3.23}$$

- spherical cap:

$$\begin{aligned} V &= \frac{\pi}{3} h^2 (3r - h) \quad \text{and} \quad S = \pi\left(a^2 + h^2\right) \\ &\text{where } a = \sqrt{2hr - h^2} \ , \end{aligned} \tag{3.24}$$

- spherical mushroom:

$$\begin{aligned} V &= \frac{4}{3}\pi r^3 - \frac{\pi}{3}(2r - h)^2 (3r - (2r - h)) \quad \text{and} \\ S &= 4\pi r^2 - 2\pi r (2r - h) \ . \end{aligned} \tag{3.25}$$

Figure 3.18 shows the transmission coefficient S_{21} averaged over the stirrer positions. Below 300 MHz the spheres enhance the S_{21} whereas above about 350 MHz there are no significant improvement. On the contrary the larger the number of

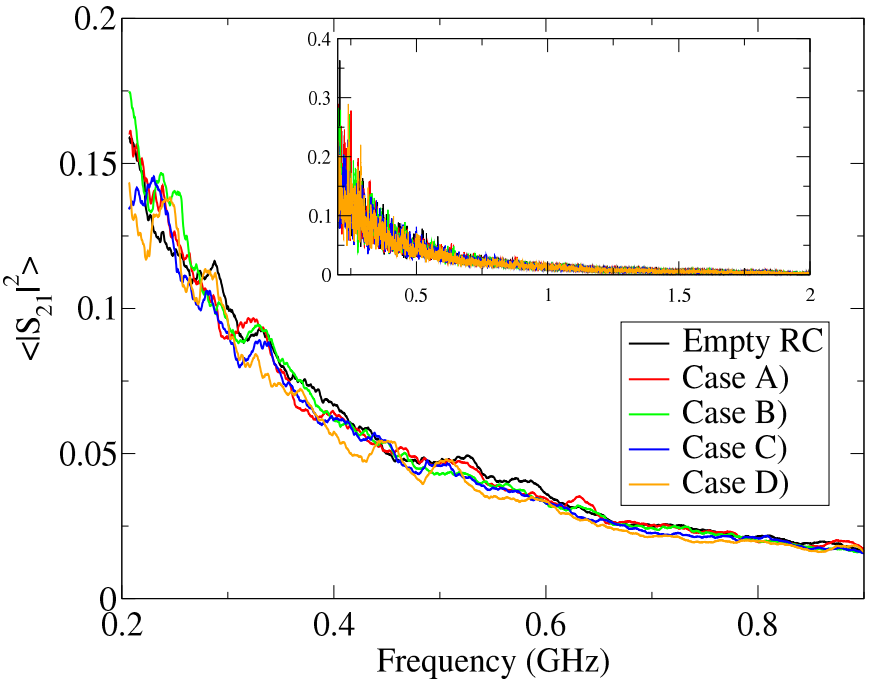

FIGURE 3.18: Simulated transmission coefficient amplitude. The inset reports raw data whereas in the main plot an average sliding window over 400 points has been used.

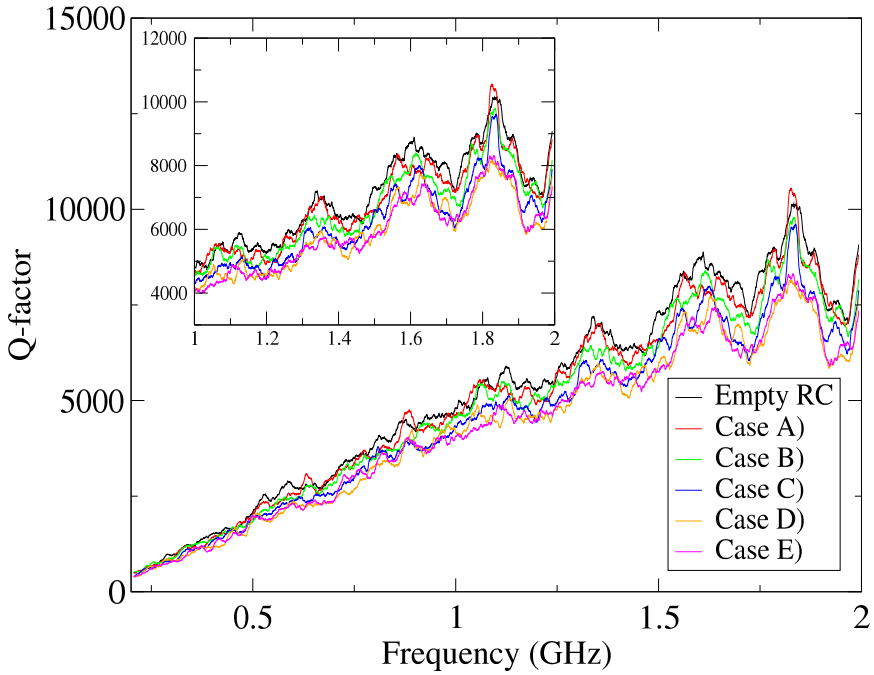

FIGURE 3.19: Simulated quality factor of different configurations. The inset reports a zoom from 1 to 2 GHz. In both plots an average sliding window over 400 point has been used.

spheres the lower the S_{21}. This fact affects the Q-factor computed by 3.12, Figure 3.19.

Moreover, Figure 3.20 reports the number of uncorrelated stirrer positions for different

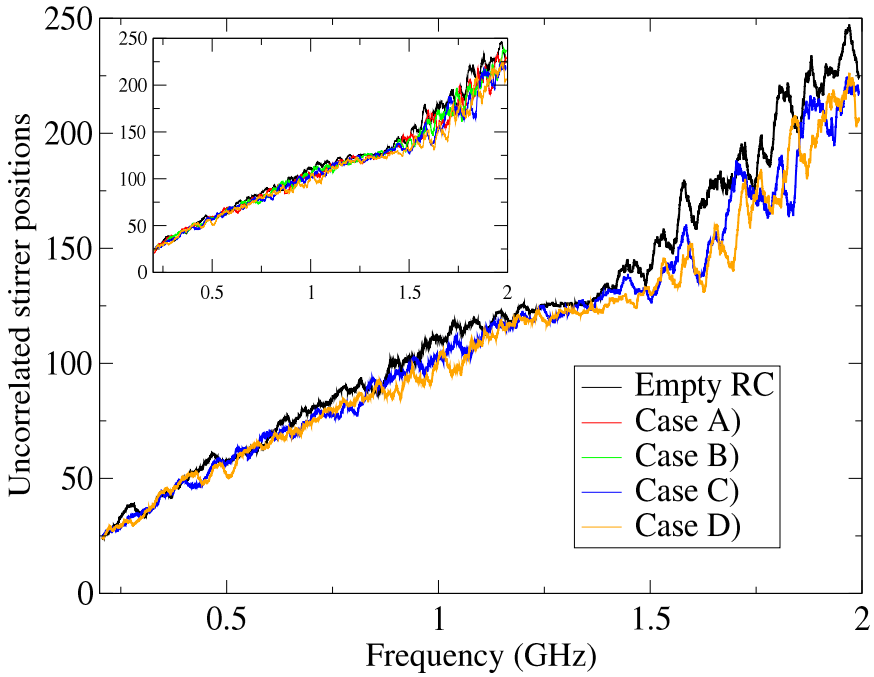

FIGURE 3.20: Simulated number of uncorrelated stirrer positions increasing the number of spheres within the RC. The main plot reports just cases where there is an appreciable difference whereas in the inset are reported all cases.

cases, evaluated by means of the ACF. As the S_{21} and Q they decrease as function of the inserted spheres. At this point, the purpose is to evaluate the improvement due to diffractors and then compare the simulated data with the analytical ones. In this way if analytical results fit the simulated ones, it is possible to evaluate a-priori the behavior of the chamber and/or how many and where diffractors have to be added inside the RC, in order to meet the requirements for a specific application. In Figure 3.21 the field uniformity evaluated by (1.77) is reported. Nevertheless the number of spheres within the RC are consistent, 30, they do not badly affect the behavior of the RC. Considered configurations meet the required values according to the IEC-standard. Increasing the radius of sphere the field uniformity get worse and there are some frequencies that exceed the limit, in some case with larger radius and larger number of spheres the filed uniformity is not acceptable and the RC cannot be used. From the Q-factor we can recover the modal bandwidth defined as

$$B(f) = \frac{f}{Q(f)} \tag{3.26}$$

and the average modal overlap

$$M(f) = m(f)\frac{f}{Q(f)} \tag{3.27}$$

where $m(f)$ denotes the average modal density that can be predicted by the Weyl's law (3.11):

$$m(f) = 8\pi V \frac{f^2}{c^3} \tag{3.28}$$

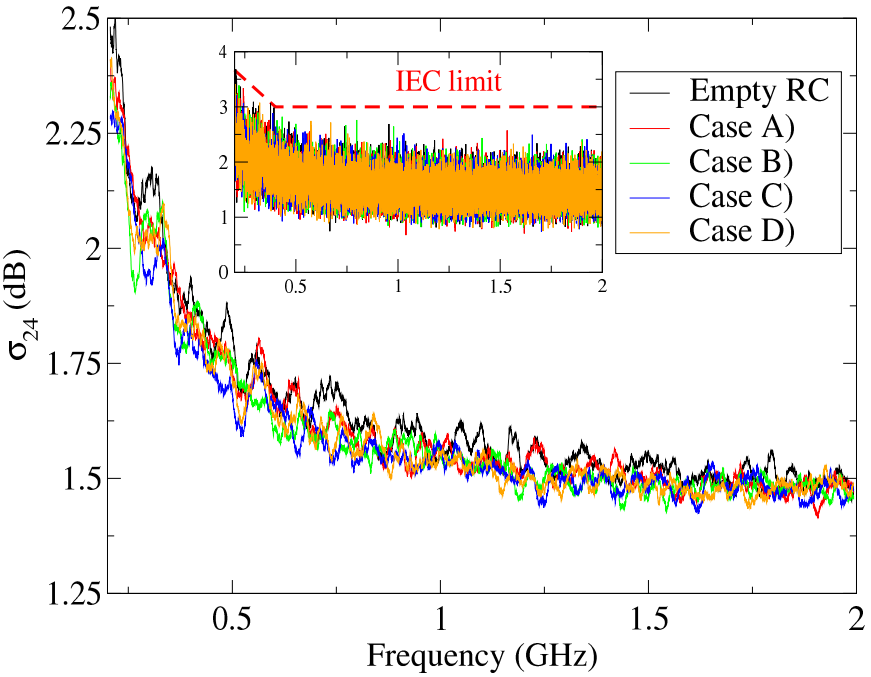

FIGURE 3.21: Field uniformity of different configurations. The inset reports raw data whereas in the main plot a sliding window over 400 frequency point has been used. The red dashed line denotes the IEC-limit.

where c is the speed of the light in the vacuum. Combining (3.27) and (3.28) we can re-write the modal overlap as

$$M(f) = \frac{8\pi V}{Q(f)} \frac{f^3}{c^3} \ . \tag{3.29}$$

It is possible to define the internal power transmission [100] which specifies a fraction of the transmitted power within the RC as:

$$P(f) = \frac{\langle |S_{21}|^2 \rangle}{\eta_{Tx}\eta_{Rx}(1-|S_{11}|^2)(1-|S_{22}|^2)} \tag{3.30}$$

where $< . >$ denotes the ensemble average, η_{Tx} and η_{Rx} the efficiencies of antennas. Combining (3.12) with (3.30) we can express $P(f)$ as

$$P(f) = \frac{Q(f)}{Q_a} \ , \tag{3.31}$$

Figure 3.23 shows a comparison of the simulated K-factor. This parameter quantifies the direct energy between the two antennas [102]. Note that the two Q-factors can be estimated without any information[6] about the chamber. Now it is possible to point out an estimator

$$\bar{M} = \frac{1}{2\pi P(f)} \tag{3.32}$$

[6] S_{21}, pdf, etc

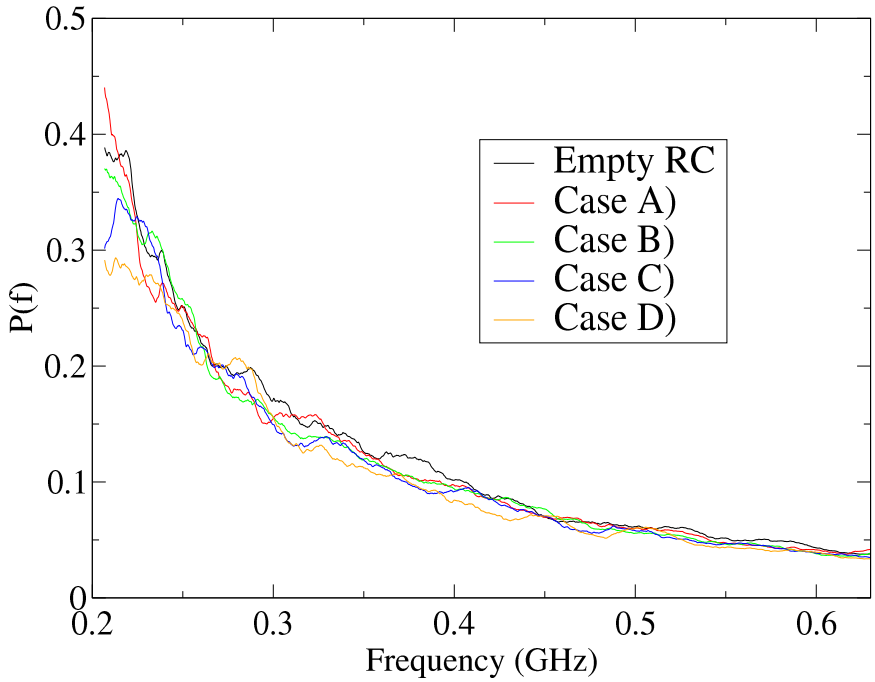

FIGURE 3.22: Internal power transmission for different configurations. Spheres have radius of 0.50 m and Table 5.1 indicates their positioning.

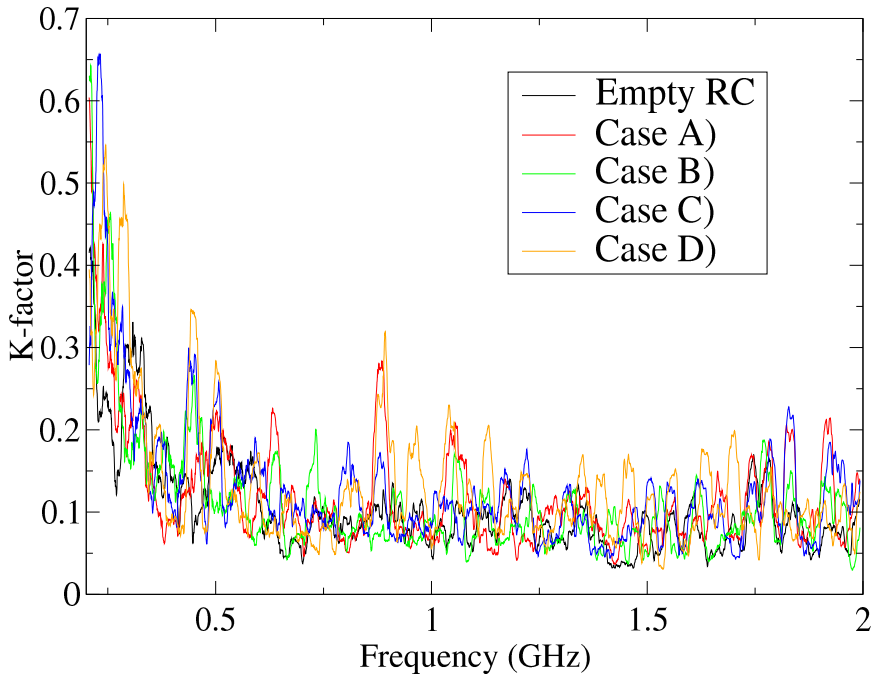

FIGURE 3.23: Simulated K-factor for different configurations. A sliding average window over 400 points has been applied.

which is relevant and easier to evaluate w.r.t $M(f)$ and do not require a-priori information about the cavity. In fact, $\bar{M}$ can be evaluated only by geometrical information, emphasizing the role of diffractors. By means simply geometrical corrections we can evaluate, roughly and fast, the improvement due to spherical diffractors. Figure 3.22 shows a comparison of the $P(f)$, evaluated by (3.30), for different cases where the number of

spheres were increased (with same radius).

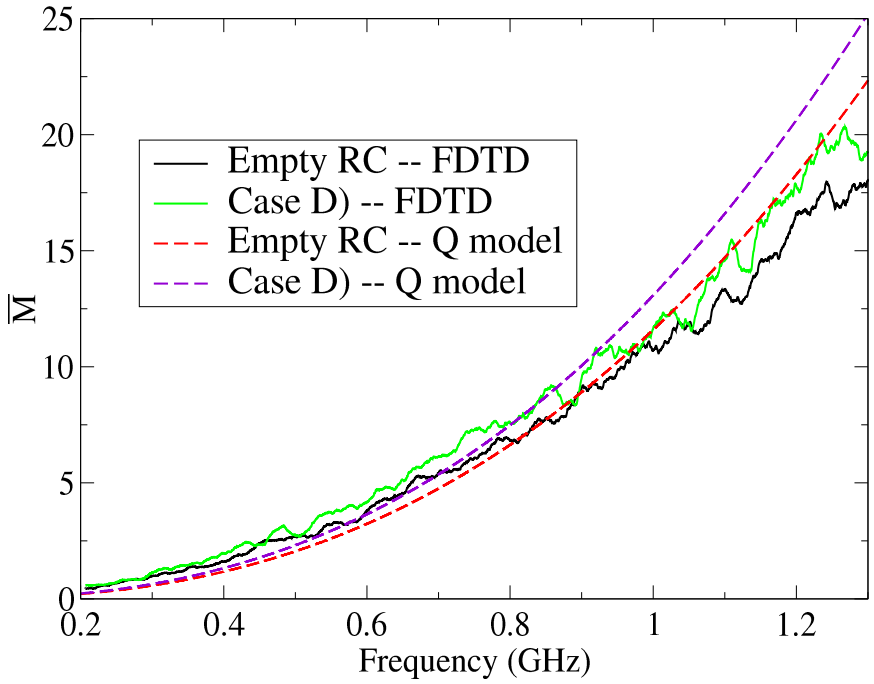

FIGURE 3.24: Comparison of the modal overlap evaluated by (3.32). The $P(f)$ was evaluated by the simulated Q and by the estimated Q_{tot} by using the simplified model.

Figure 3.24 reports the comparison between the modal overlap $\bar{M}$ obtained by (3.32) where the internal power transmission $P(f)$ can be evaluated in two ways: by considering the resulted quality factor (results of FDTD simulation) or considering the Q estimated by (3.15) where geometrical corrections due to spheres have to be considered [7]. Curves of Figure 3.24 can be compared in two ways. The first is between the black (red) curve w.r.t. the green (violet) one and denotes an improvement in terms of modal overlap when spheres were added into the chamber. The second is the comparison between the black (green) curve and green (violet) one where the two ways for the evaluation of the $\bar{M}$ were applied. Namely, adopting the Q due the FDTD simulations (3.12) or the Q_{tot} (3.15) in (3.31) and this result asserts that the simplified model for the Q (3.15) meets the simulated results. In other words by using the Q-model we can estimate the improvement given by spheres without a priori information about the chamber. The model is still valid up to about 1.2 GHz, above the model overestimate the modal overlap, obviously the simulated Q is more accurate. However, this result asserts that if we want to reach a desired improvement we can chose the dimensions, kind and position of curved diffractors just by a simple evaluation of the Q (3.15).

Figure 3.25 reports the comparison of the chaotic chamber E) and F) cases w.r.t. the regular (rectangular) RC with the same "effective" volume. Effective volume means the total (reduced) volume taking into account the presence of spheres. Dimensions of the reduced chamber were chosen in order to maintain the same positions of antenna,

[7] volume reduction for both Q and Q_a and surface reduction for Q

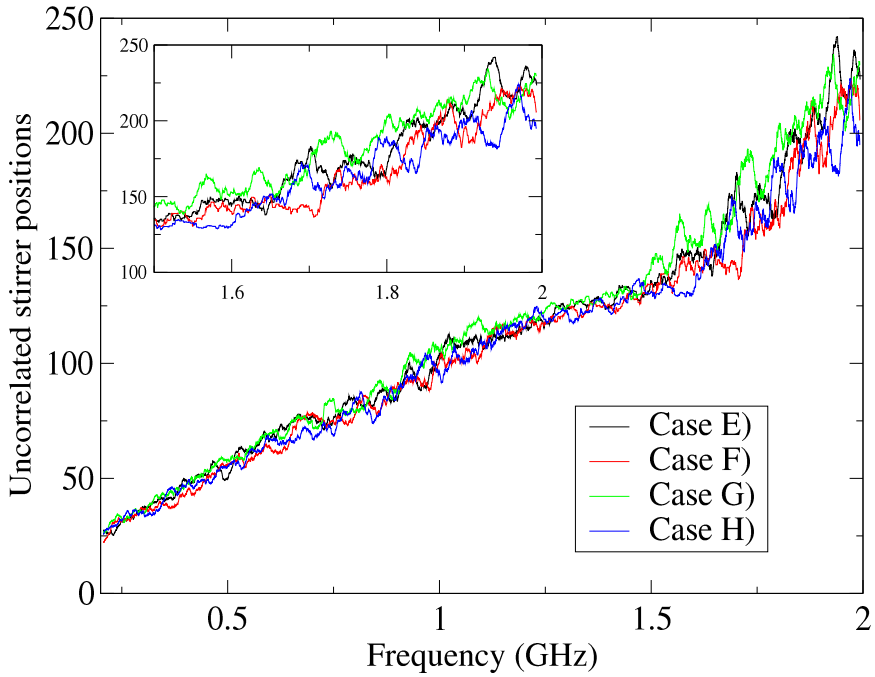

FIGURE 3.25: Uncorrelated stirrer positions of the chaotic RC compared to a rectangular empty RC with the same "effective" volume.

stirrer and WV. The plot has to be read comparing pairs E)-G) and F)-H). We can note that trends remain similar each other, just some peaks are different, probably due to the shift of resonances caused by the variation of the chamber's size.

Moreover, this result suggests us to deeply investigate the effect due to the volume reduction. As stated in previous papers, i.e. [96–98] and the increase of the modal overlap, diffractors increase the behavior of the RC and permits to obtain a shift of the LUF at lower frequencies. At this point, considering characteristic parameters used in EMC i.e. uncorrelated stirrer states (positions) we observed that the lager number of spheres the lower the number of uncorrelated stirrer positions. This is due to the losses that have to be accounted in the simulations, see next section.

Furthermore, to turn the table another possible way to evaluate the improvement due to spheres comparing a smaller chamber equipped by spheres to a larger chamber. If performance will be better or the same the role of spheres will be demonstrated. The trad-off is the available volume, because a smaller chamber (w.r.t. the original one) with spheres will have a limited WV, in some case not sufficient for measurements where DUT has to be tested.

Thanks to the random coupling model (RCM) [103–107] method it is possible to evaluate another estimator due to the ratio between modal densities of the chaotic (with spheres) and the regular (empty) chamber, denoted by M^c and M^r respectively,

$$\frac{M^c}{M^r} \underset{\alpha>1}{\longrightarrow} 1 + \frac{\Delta S^c(r_s, \#N)}{\Delta S^r} \tag{3.33}$$

where the superscript r indicates the regular chamber whereas c the chaotic one, r_s indicates the dependence from the radius of spheres and from $\#N$ which represents the

cardinal number of spheres. The α denotes the loss parameter of the cavity to apply in the RCM, it is necessary in order to describe a chaotic system, it can be evaluated by

$$\alpha = \frac{k^3 V}{2\pi^2 Q} \tag{3.34}$$

where V is the volume of the cavity, Q the quality factor and k the wave number; in a loss environment $\alpha > 1$[8]. It is worth noticing that in (3.33) the ratio depends only by the

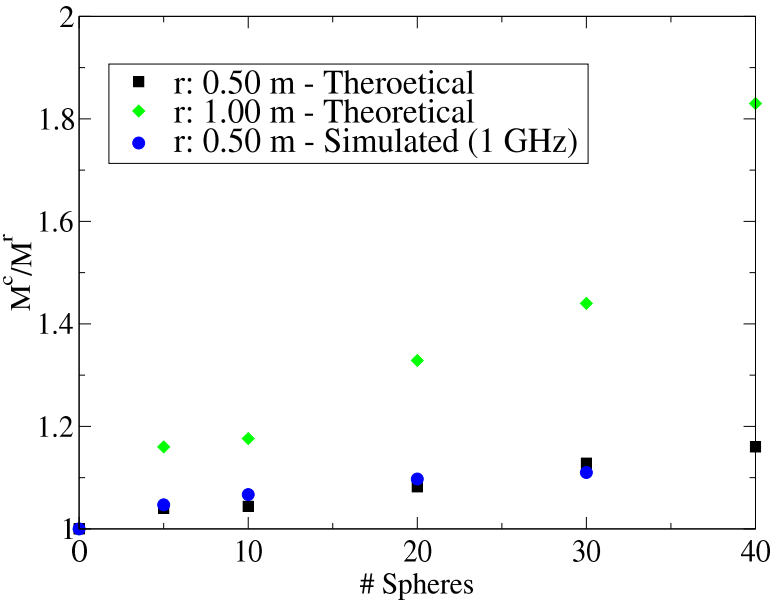

FIGURE 3.26: Comparison between theoretical and simulated ratio of the modal densities as function of number of spheres. The simulated points were picked up at 1 GHz.

surfaces, in particular, ΔS^c indicates the exceeding portion of surface w.r.t. the starting one, whereas ΔS^r consists of the whole surface of the RC. Figure 3.26 reports the trend of the modal densities ratio evaluated by (3.33) as function of the number of inserted spheres. Theoretical point were obtained by calculating the ratio between surfaces whereas the simulated (blue curve) is obtained doing the ratio of M^c and M^r by means the S_{21} and (3.29). Theoretical results meet the simulated one and it is worth noticing the improvement due to spheres, in particular for spheres with radius of 1 m (about 20% for five spheres). Continuing by attempts it is possible to find the right position, dimension and number of spheres that has to be inserted to reach the desired improvement in terms of modes.

Recalling the adoption of the distributed losses within volume of the chamber (Chapter 1) we have to take into account the volume reduction due to insertion of spheres. Due to this observation there are two considerations about the volume reduction:

- reducing the total volume means decrease the "overall losses" (less volume means less cubic cells)

[8] it can be evaluated by the variance of elements that form the normalized impedance matrices of the waveguides connected to the ports of the considered cavity

- insert objects i.e. spheres, affect (increase) the losses of the cavity (expecting a lower Q-factor).

If wall losses were/are considered, it is simple to guess that the complexity of the code increases and the speed-up decreases, i.e. subgridding the contour of spheres by non cubic cells, "find" the conductivity value of spheres[9]. In each simulation the value of σ_v was increased proportionally both to the decrement of the total volume and to the increment of the total surface, the best matching value with experimental results in going to be evaluated. Hypothesis that spheres lower the Q-factor of the RC is reported in the next section.

Although the volume reduction seems to play a relevant role in this analysis, further investigation by a statistical analysis is ongoing, i.e. pdf of the scattering parameters, evaluation of higher order momentum.

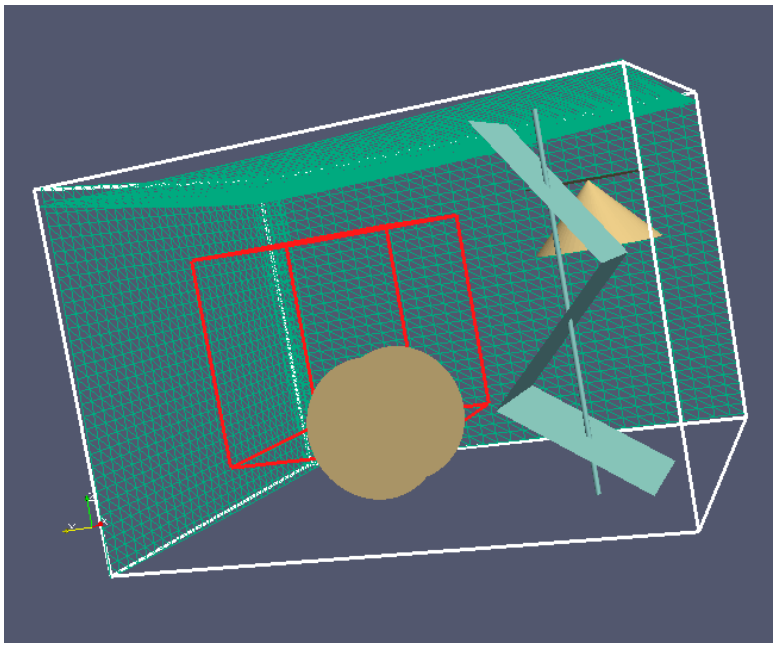

FIGURE 3.27: Side view of the RC with tilted walls (three walls). The red box denotes the WV. The RC was equipped by two discone antennas and a z-folded vertical stirrer.

Another idea was to consider a rectangular RC and tilt their walls Figure 3.27. An improvement to this configuration could be to insert some spheres in order to make the RC fully chaotic at very low frequency.

3.4 Experimental evaluation

In order to confirm the increase of the value for losses (volumetric) in simulations regarding the chaotic RC, few (at the moment) qualitative measurements were performed in the Ancona's RC. Figure 3.28 shows the only sphere placed within the chamber a cor-

[9] spheres simulated as PEC

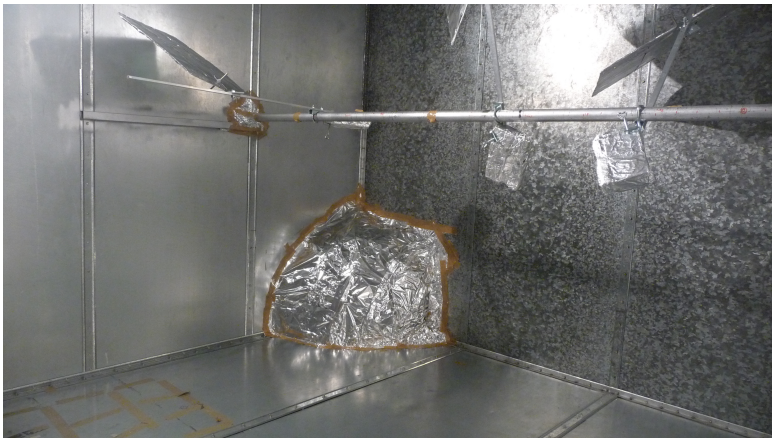

FIGURE 3.28: Picture of the sphere placed on the corner of the RC. The sphere was covered by aluminum. Radius: 0.75 m about.

ner. Its radius is 0.50 m and the contour was covered by aluminum[10]. We considered 360 stirrer positions of the z-folded vertical stirrer only. Two log-periodic antennas collected the S_{21} transmission coefficient reported in Figure 3.29. We can note that at low frequency the S_{21} is slightly higher than the chamber without the sphere. It is important

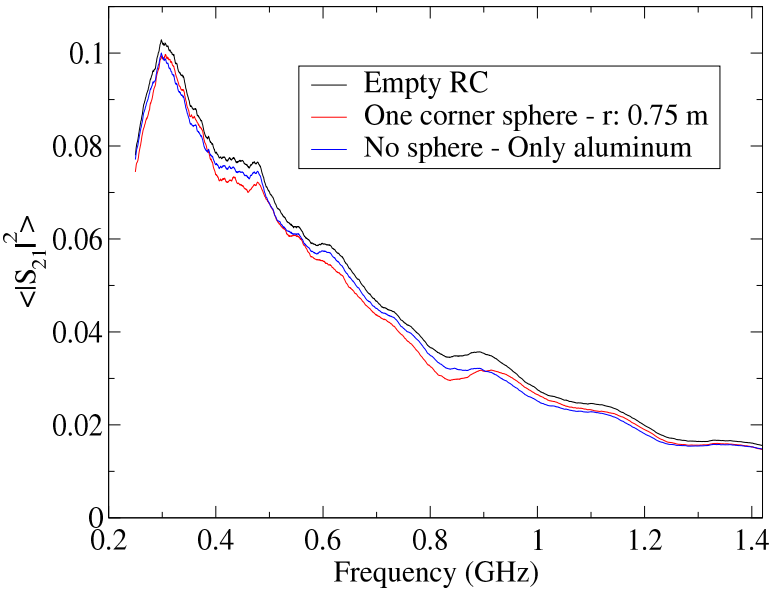

FIGURE 3.29: Measured transmission coefficient S_{21}. An average sliding window over 400 points has been applied.

to remark that the comparison has to be done between the chamber with sphere/s and the empty chamber but with aluminum sheet/s inside; because the insertion of material within the RC affects the Q, Figure 3.30, which is very sensible when the chamber is unloaded. Then is discounted that the RC without anything inside exhibits always better performance. As a consequence of the decrement of S_{21} and the Q, as expected the number of uncorrelated stirrer positions decrease as well [108], Figure 3.31.

[10] it is simply cookie sheets, the same used in the oven

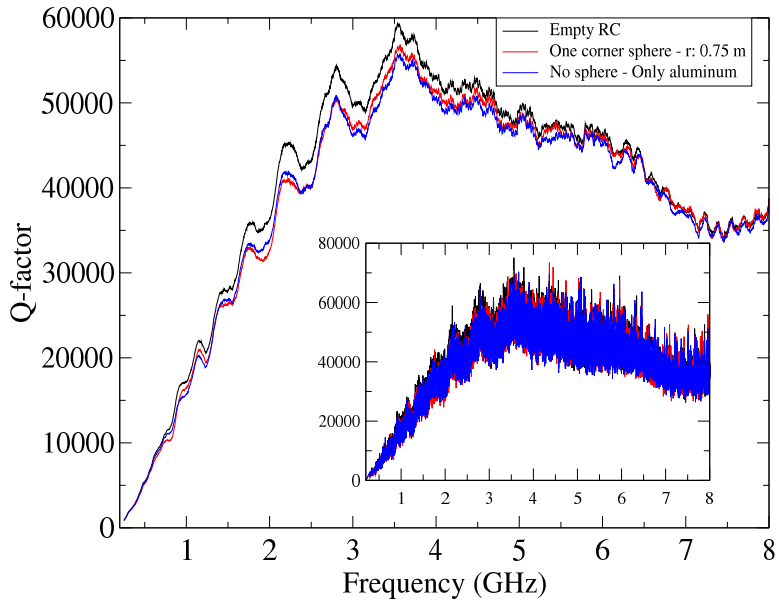

FIGURE 3.30: Measured quality factor. The inset reports the raw data whereas in main plot an average sliding window over 400 points has been applied.

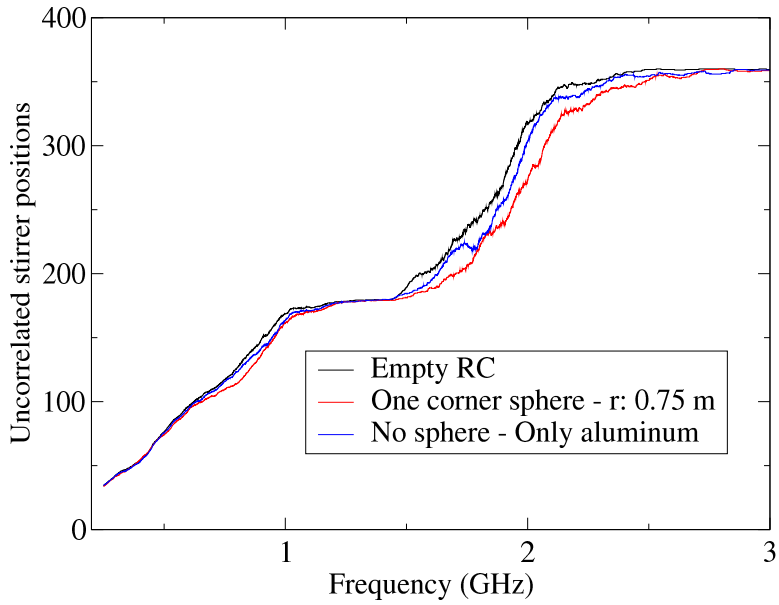

FIGURE 3.31: Measured uncorrelated stirrer positions. A sliding window average over 400 points has been applied.

Chapter 4

Enhancing the stirrer performance

4.1 Introduction

In Chapter 3 has been evaluated the improvement of chamber's performance by modifying its shape. Conversely, here are reported results obtained by considering a new stirrer's shape. Performance of a stirrer depends on its shape, dimension and position in the chamber [29, 109–113]. Moreover, it is possible to combine more stirrer concurrently [26, 27, 114–116]. During my Ph.D. in collaboration with my Ancona's group and L. R. Arnaut a new helically shaped stirrer has been proposed. This stirrer was completely made step by step and two analyses were done. The first one was done considering an helical path along the stirrer axis whereas in the second case an actual helically-shaped stirrer was evaluated.

4.2 Setup description

Figure 4.1 shows a sketch of the measurement setup. Within the RC there are two log-

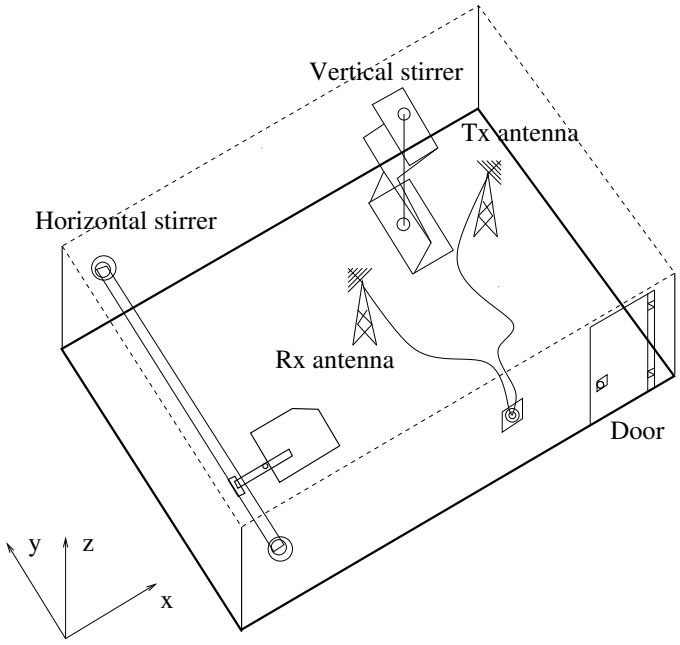

FIGURE 4.1: Sketch of the measurement set-up. Just one paddle is mounted in this representation.

periodic antennas in order to collect the S_{ij} parameters. The investigated band is from 0.25 to 6.5 GHz, which is divided in several subbands of 400 MHz where 1601 frequency point were acquired (every 250 kHz). and two stirrers. The z-folded vertical stirrer remains fixed at 0° during all measurements, it is used just as a kind of diffuser. The horizontal stirrer indeed is formed by a variable number of paddles, from one to six, mounted on the stirrer axis properly equispaced. Paddles are equal each other and its shape is reported in Figure 4.2. The dimensions of a paddle are:

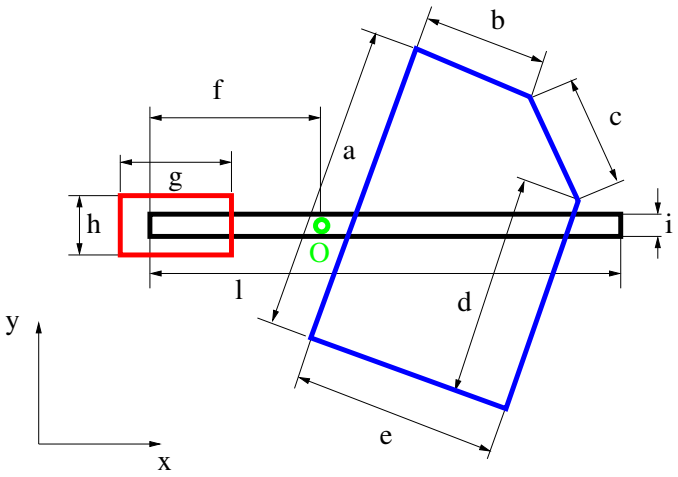

FIGURE 4.2: Sketch of the measurement set-up.

- $a = 0.675$ m
- $b = 0.410$ m
- $c = 0.170$ m
- $d = 0.510$ m
- $e = 0.570$ m
- $f = 0.500$ m
- $g = 0.240$ m
- $h = 0.055$ m
- $i = 0.020$ m
- $l = 1.140$ m
- paddle made by silhouette of corrugated cardboard with dimensions: $0.675 \times 0.570 \times 0.050$ m^3
- "cornered" steel plate with an azimuthal angle of 45° with dimensions: $0.040 \times 0.090 \times 0.030$ m^3
- aluminum hollow alloy bar with dimensions: $1.140 \times 0.020 \times 0.010$ m^3

- aluminum coated brick with dimensions: $0.250 \times 0.120 \times 0.060$ m^3
- steel clamp with eighth of 0.075 m.

The red box in Figure 4.2 represents the counterweight used to correctly balance the paddle over the stirrer axis, the green circle denotes the point where the paddle is fixed on the stirrer axis, the blue highlights the aluminum foil that covers the paddle and the black color represents the shaft that connect the foil and the counterweight to the stirrer's axis. Along the horizontal axis it is possible to mount maximum six paddles (see Figure 1.4)

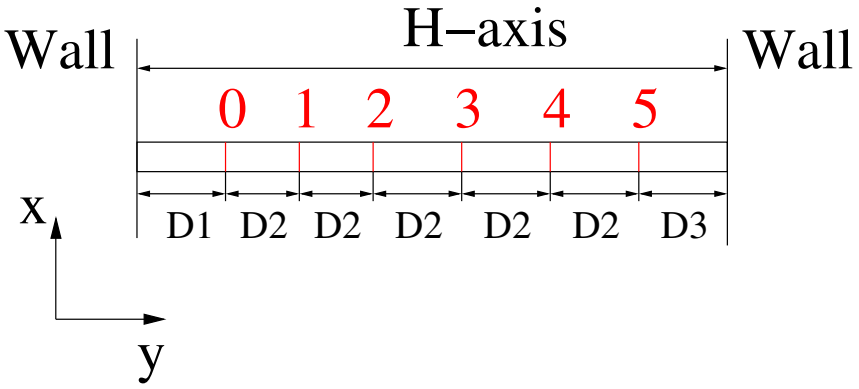

FIGURE 4.3: Sketch of the horizontal stirrer axis. Red numbers denote the position of paddles when all of them (six) were mounted.

equispaced by $D2 = 0.50$ m, Figure 4.3. The entire length of the axis is 4 m whereas the distance from the walls are $D1 = 0.67$ and $D3 = 0.33$ m. The analysis was conducted in two ways:

1) mounting a single paddle on the stirrer axis the helical stirring is given by simultaneous translatory and rotational deviation of the paddle along the axis (helical stirring)

2) considering the whole stirrer composed by paddles (helical stirrer).

4.2.1 Helical stirring

Basically, the helical stirring process was implemented combining both rotational and axial translation by several steps. The finer the step the better the resolution and the longer the measurements campaign. The goal of this study was to highlight the effect due to the path geometry that follows an arbitrary stirrer, it is a dynamic way opposite to the static one [23, 117–119]. The helical path (due to one paddle mounted on the axis) is showed in Figure 4.3. Along the horizontal axis it is possible to mount maximum six paddles (see Figure 1.4).

Each measurement lasted about 4 or 20 hours, depends on the number of considered steps. To ensure that oscillations after each movement of the paddle along the axis do not affect the results a dwell time of 6 s was set. The finer resolution was fixed every 6.25 cm that implies 45 translatory stir circles combined to the cylindrical tuning. For

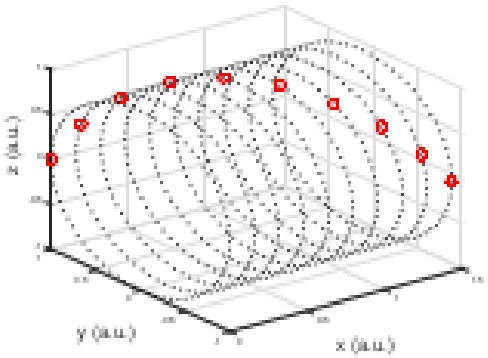

FIGURE 4.4: Representation of the path (red dots) followed by the paddle during the whole rotation.

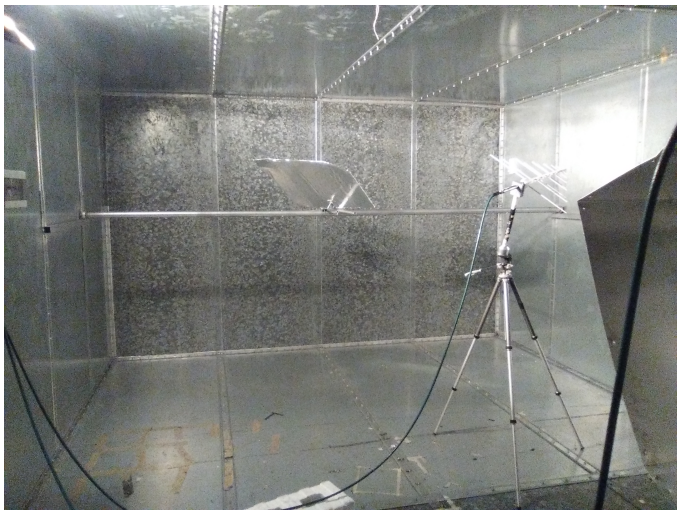

FIGURE 4.5: Setup of the emulated helical stirring. The paddle is mounted on the center just for a better view, actually its position along the axis was translate in many points.

each position along the axis a full rotation of the blade was performed, i.e. for 72 steps by 5° the cylindrical tuning results a set of 45×72 states. Afterwards, increasing the initial phase angle θ_i ($= 0$ at the beginning) stir helices were obtained Figure 4.6. Figure 4.6

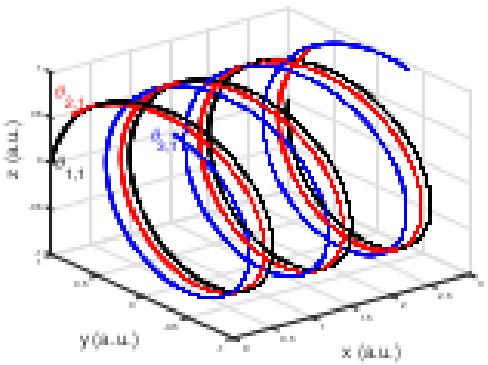

FIGURE 4.6: Example of three helical turns that generate three stirrer realization. In particular, $\theta_0 = 0°$ (clack curve), $\theta_1 = 40°$ (red curve) and $\theta_2 = 110°$ (blue curve).

reports the number of

Figure 4.4 shows the route followed by the paddle (Figure 4.5). Now, considering the paddle mounted at the first point along the horizontal axis, i.e. at 0.67 m from the left wall (Figure 4.3) with the elevation angle equal to 45°, the whole helical stirring is given by the collection of the following paddle positions equispaced by a determined distance with an elevation angle increased by 5°[1] for each step. The exact sampling scheme for all the possible helices is reported in [115]. Here is not reported the detailed description of the method and the experimental results, well explained in the paper but improvement due to this configuration.

The analysis was done by considering the Pearson autocorrelation coefficient ρ of the $|S_{21}|^2$, the mean value of the maximum-to-average ratio and the minimum-to-average-ratio of both $|S_{21}|$ and $|S_{21}|^2$; also the effects of chirality were explored. The peculiarity of these results is the were obtained by measurements (by-passing theoretical models); they provide directly to assert that helical stirring exhibits better performance w.r.t. circular stirring. However, a comparison with theoretical probability density functions were done.

Experimental results pointed out that helical stirring reduces auto- and cross-correlation leading a better stirring method, in particular w.r.t. a circular stirring at low frequencies. For a better design of this kind of solution parameters to take into account are radius of the blade, its angular step and size, the pitch that depends on the required frequency range. Conversely, helical stirring occupies larger volume w.r.t. circular stirring. Interesting results are reported in [115] and some animations for a better comprehension of the geometry are available here.

4.2.2 Helical stirrer

Conversely to the analysis done in the previous paragraph, here was considered the whole stirrer made by different configurations of paddles (Figure 1.4 shows the horizontal stirrer with 6 paddles). The helically shaped stirrer, but it consists by more than one paddles at the same time. Paddles are made by the same material and have the same dimension, Figure 4.2. The investigated band is from 0.25 to 1.25 GHz and the acquisition step by the VNA is 250 kHz (1601 point in subbands of 400 as in the foregoing setup). Performance of this geometry were evaluated by means of the number of uncorrelated stirrer positions, by the ACF [11]. Figure 4.7 reports the number of uncorrelated stirrer positions N_{ind} for the horizontal stirrer when one or more paddles (up to 6) were mounted on its axis. Paddles were mounted by a shift of 60° each other along the horizontal stirrer axis. The red curve represents the N_{ind} of the vertical stirrer in the same chamber. Adding paddles we reached the saturation (72 stirrer positions) at lower frequencies. There are not significant benefit using 5 or 6 paddles. It is evident that increasing the paddles gives a relevant improvement of this parameter, this means that the helical stirrer improves the

[1] 5° for 72 stirrer positions whereas 1° for 360 stirrer positions

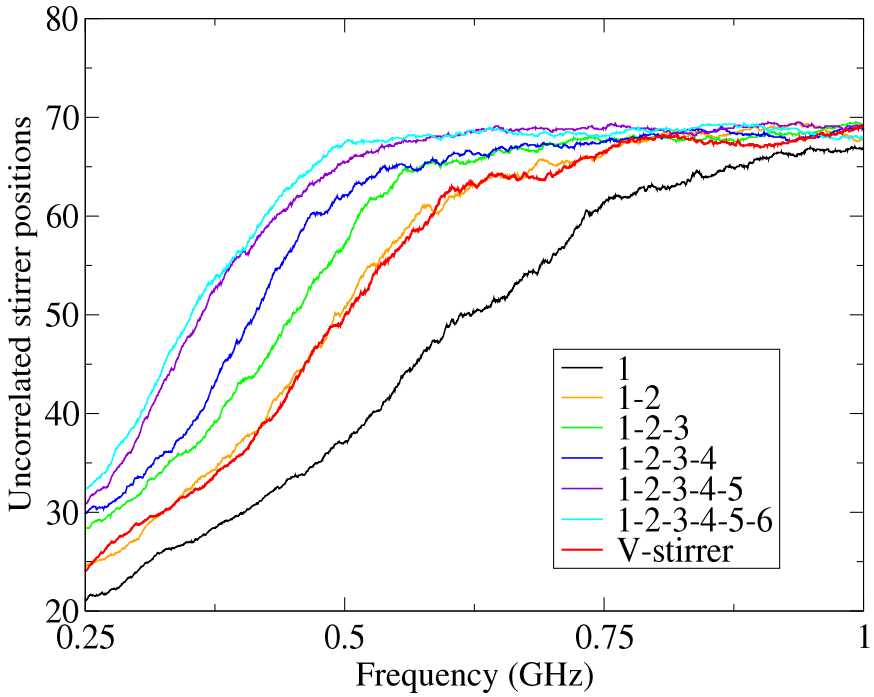

FIGURE 4.7: Number of uncorrelated stirrer positions when the number of paddles were increased. Comparison with the vertical stirrer (red curve) is showed. A sliding average window over 400 frequency points has been used.

capability of the stirrer to well operate at low frequency range w.r.t. other existing stirrer (the z-folded in this case). Figure 4.8 reports the Q-factor for the horizontal stirrer

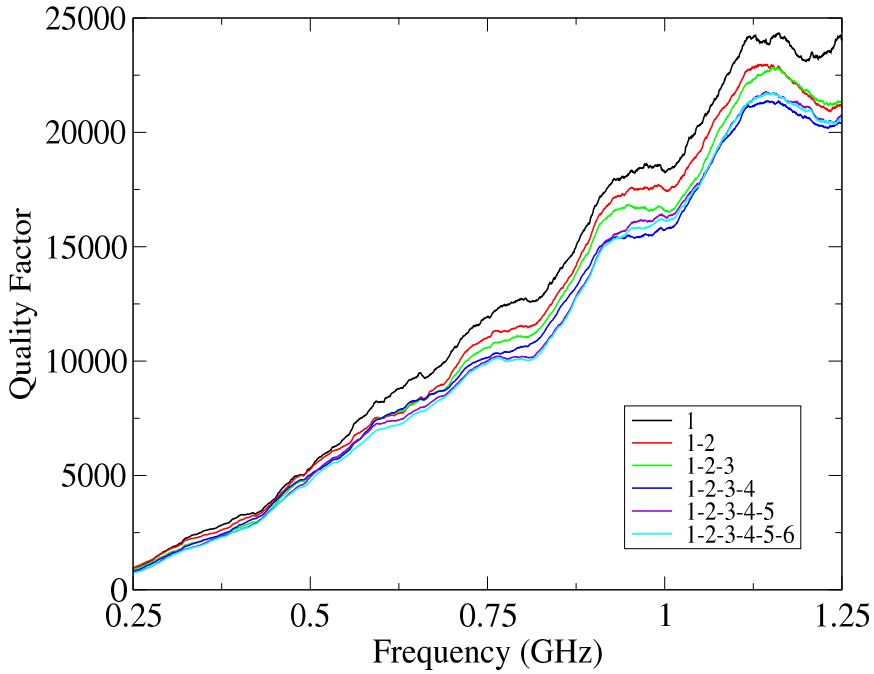

FIGURE 4.8: Measured quality factor of the chamber with different configurations, from one up to six paddles. A sliding average window over 400 frequency points has been applied.

composed by different number of paddles. As expected, the larger number of paddles the lower the Q, because adding objects (paddles surface and counterweight) inside the chamber involves to the increase of ohmic losses. The position of paddles does not affect the Q, that depends only by the inserted material. Moreover, was evaluated the effect due to combinations of pairs, triplets and four paddles mounted along the axes, varying their positions. As expected there were no relevant variations, in fact in [111] the same behavior was observed. However, if two paddles are titled each other, the more the tilting the more the uncorrelated stirrer position. Figure 4.9 is a picture of the horizontal stirrer with two paddles shifted by 40° whereas Figure 4.10 reports the number of uncorrelated stirrer positions for different cases. It is worth noticing that increasing the tilting angle

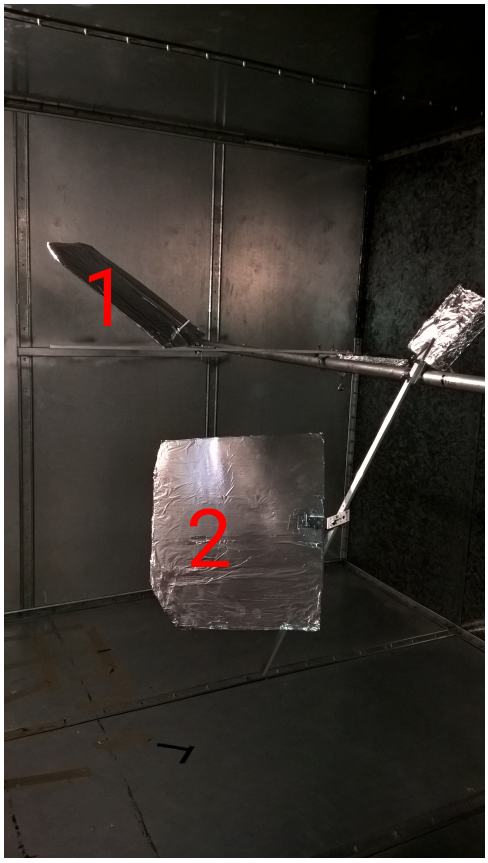

FIGURE 4.9: Picture of the horizontal stirrer with two paddles mounted on it. Paddle #1 is fixed at 0° whereas #2 is fixed at 40°.

between the paddles arise the stirring effect. In other words it is convenient to create a staggered stirrer instead of increase its length and maintain them aligned, obviously considering the same number of paddles. This feature is clear at low frequency as well.

These analyses show that the helical stirring/stirrer is able to improve performance, evident in the low frequency range where, usually, the stirrer optimization is worth noticing. Required specifications can be attained by choose the dimension of paddles/stirrers. The trade-off is the volume consuming, that can be stringent is some application. Moreover, the volume play a key role, because there will be an "optimal" stirrer for each specific chamber. In other words, there is an operating "limit" for the designed stirrer,

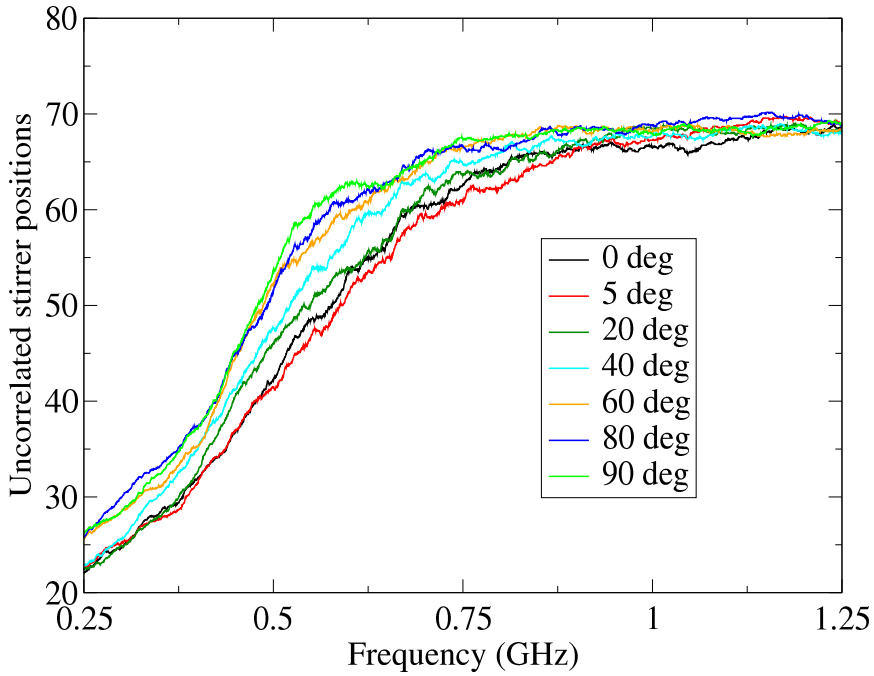

FIGURE 4.10: Number of uncorrelated stirrer positions of two close paddles when they were shifted incrementally. The tilting angles are reported in the label.

below this limit the stirrer does not perform well. On the contrary, when the stirrer becomes small w.r.t. chamber's dimensions its effect is not relevant and becomes inappropriate, see Figure 4.11 [112]. Having a tailored stirrer (shape, dimensions) its a constraint that should be satisfied in order to obtain reliable results. Figure 4.11 reports the optimal

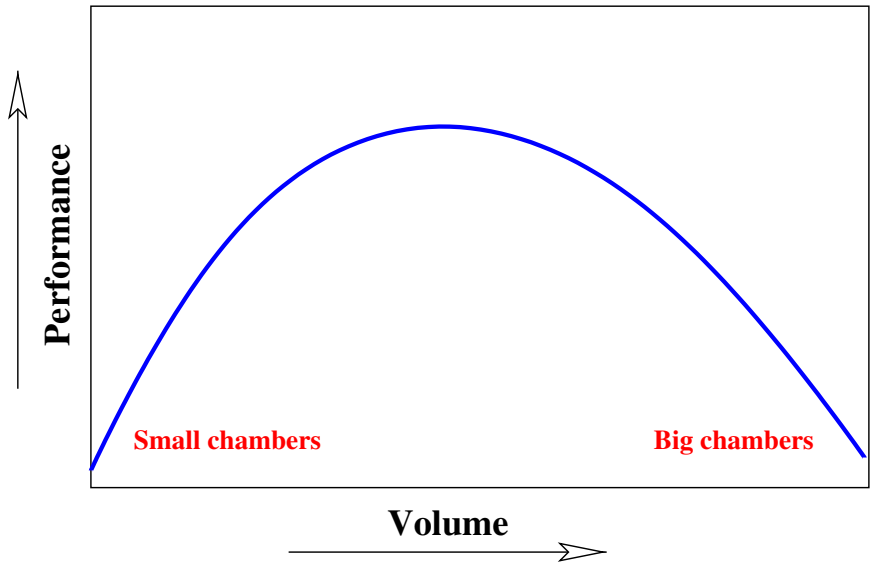

FIGURE 4.11: Estimation of the trend performance for a stirrer within a small/big chamber. The abscissa denotes the performance whereas the ordinate denotes the expected performance.

behavior of a stirrer w.r.t. the volume of the chamber. There will be an "optimal" (indicated by maximum value of the curve) value of the volume for a specified stirrer and vice

versa.

Further evaluations/optimization is ongoing by numerical simulations that allow: save time w.r.t experimental measurements and analyze many configurations hard to try in the laboratory[2].

4.3 Ongoing works

During my PhD some stirrers' shape have been evaluated. The purpose of this analysis was to design a proper (mechanical) stirrer that enhances the performance of the chamber, hopefully focusing on the low frequency (w.r.t the chamber's dimensions) range. Figure 4.12 shows a possible configuration of a new-shaped stirrer. The horizontal stirrer is placed close to the ceiling. It is helically shaped and rotates along the $\hat{y}$ and $\hat{z}$ Cartesian directions. A part the dimension, the pitch between two adjacent helices is a key parameter. This configuration is under investigation and preliminary results show a very good performance, at low frequency as well. The problem is that exhibits a large occupied volume and from a practical point of view it need a consistent support in order to hold its weight.

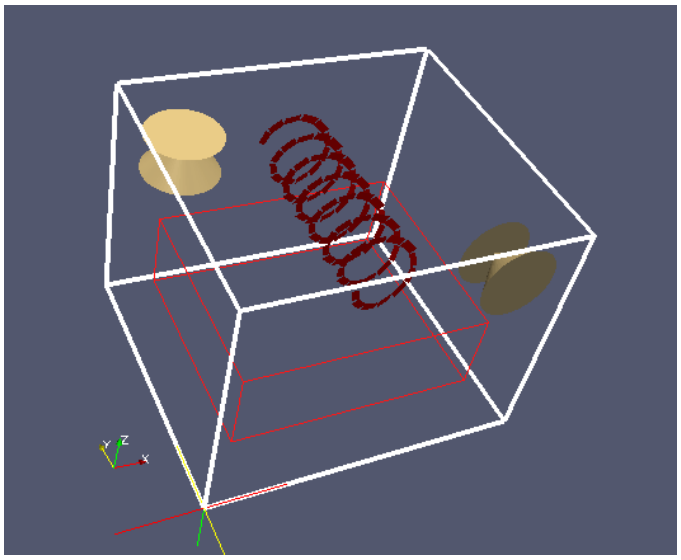

FIGURE 4.12: Prototype of the helical stirrer with two axes rotations. The red box represents the WV.

[2]waste of time and money customize an already existing RC for every stirrer's shape (think to buy new controller/motor for the stirrer)

Chapter 5

Reverberation chamber for emulate real multipath propagating environments

5.1 Introduction

The reverberation chamber, apart for EMC tests, is used for replicate real environments which exhibit a Rician propagation channel [120–123]. Emulate this propagation conditions is very useful in order to test wireless devices inside the RC [124–127] instead of for example on-site measurements where move all necessary instrumentations could be hard. The ability of control the power delay profile (PDP) of the chamber plays a key role for the replication of the desired environment. Desired environment because loading conveniently the chamber, according to the standard [128, 129] it is possible to replicate the chosen one. Experimental results have been addressed to this purpose [122, 123], namely relate the RMS time delay spread (τ_{RMS}) to a loaded chamber. The τ_{RMS} defines the testing condition [128, 129]. Ensured the correct emulation of the real environment the chamber is ready for tests and some applications are described in [102, 130–134].

The use of RC for wireless measurements can be summarized (roughly) in this comparison:

- conducted tests are repeatable but antennas are not included in tests, i.e. not useful for measurements regarding smartphone
- in over-the-air (OTA) tests antennas are included in tests and devices which have integrated antennas, moreover very useful for MIMO test.

Moreover, the possibility of reproduce specific environments allow to test not only wireless devices but also performance of the communication standard, i.e. the evaluation of 4G-LTE and 5-G standards in particular conditions/scenarios. I was engaged in these activities collaboration with the Ancona's group and Telecom Italia. The characterization of the RC is only the first step before performing reliable measurements.

During my visiting at the University of Nottingham, measurements were done in order to characterize its RC for further activities.

5.2 Setup description

For the emulation of real-life environments the Ancona's RC was used. Preliminary measurements were done in the Nottingham's RC as well. The setup of the Ancona's RC is described in previous Chapters of this thesis. In these measurements, both stirrer were used in synchronous way, 20 stirrer positions in total. The investigated band is from 50 MHz to 8.5 GHz putting together many (169) subbands of 50 MHz. In each subband 1601 frequency points were acquired. With these values the band was sampled by steps of 31.5 kHz, this choice is needed in order to correctly perform an Inverse Fourier transform (IFT) to get the chamber's response [135]

$$h(t) = IFT[s_{21}] \tag{5.1}$$

without aliasing, in compliance to the sampling theorem. Measurements were repeated for N stirrer positions, achieving:

$$PDP(t) = \left\langle \left| h(t) \right|^2 \right\rangle_N \quad , \tag{5.2}$$

where $\langle . \rangle$ denotes the ensemble average over N stirrer positions. From the PDP we can evaluate the RMS time delay spread

$$\tau_{RMS} = \frac{\sqrt{\int_0^\infty (t-\tau_{ave})^2 PDP(t)dt}}{\int_0^\infty PDP(t)dt} \quad , \tag{5.3}$$

where

$$\tau_{ave} = \frac{\int_0^\infty tPDP(t)dt}{\int_0^\infty PDP(t)dt} \quad . \tag{5.4}$$

When we apply 5.2, a threshold of -30 dB is considered, as described in [136]. The amount of absorbers placed within the RC is strictly related to the required performances, such as the quality factor value, the LUF, the chamber time response [120, 137, 138] and the statistics of the RC.

5.3 Results

The PDP of the chamber depends not only by the number of absorbers put in the chamber but also on their positioning. In fact, absorbers on vertical position have larger surface to the RC field so they have more impact on the overall behavior.

Figures 5.1, 5.2, 5.3 and 5.4 show different loaded configuration of the RC. There were used three kind of absorbers, the ANW-77 flat absorber, VHP-18-NRL (big pyramidal) and VHP-8-NRL (small pyramidal). The quality factor of the previous configurations is reported in Figure 5.5. Absorbers in the center of the RC and in vertical position have a higher impact on the overall absorbing decreasing the Q and consequently the decay

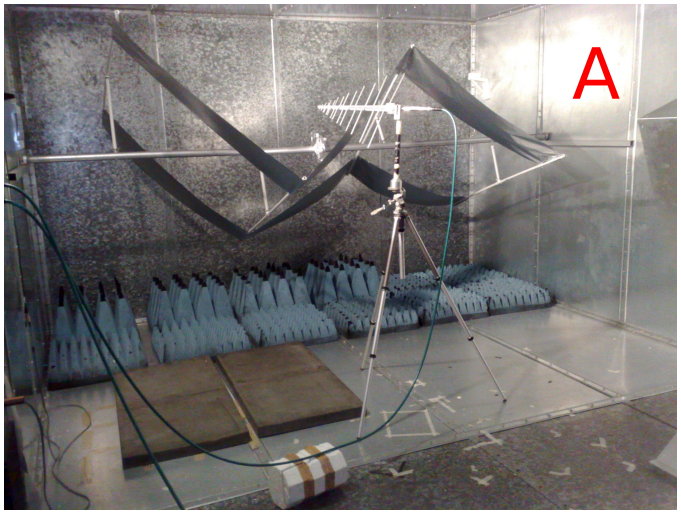

FIGURE 5.1: Absorbers are placed on the floor along a single side of the RC.

FIGURE 5.2: Absorbers placed on the center of the RC and along its perimeter.

TABLE 5.1: Time delay spread of the analyzed configurations.

Delay spread (ns)	A	B	C	D
Average	167.15	125.53	116.4	118.98
RMS	273.70	351.11	223.24	592.33
Average – threshold -30 dB	160.23	119.69	112.93	105.60
RMS – threshold -30 dB	125.86	78.46	72.04	70.06

time, due to the relationship:

$$\tau = \frac{Q}{\omega} \tag{5.5}$$

where the Q was computed by (3.12). Table 5.1 reports the measured time delay spread of the RC for $\#A$, $\#B$, $\#C$ and $\#D$ configurations. Table 5.2 reports typical values of real scenarios as function of the time delay spread [128]. Comparing obtained values for the

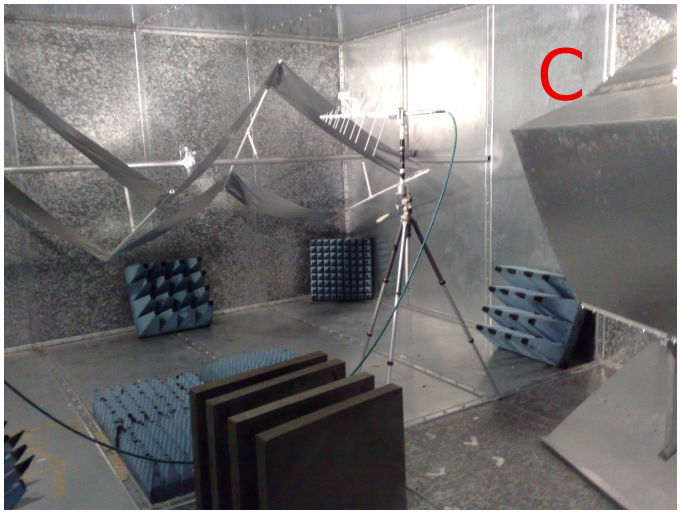

FIGURE 5.3: Absorbers placed along the perimeter, on the center of the RC, horizontal and vertical position.

FIGURE 5.4: Absorbers placed on the corners and on the center of the RC. This configuration is called “barrier”.

τ_{RMS} with values reported on the standard [128] the Urban Micro environment (NLOS)[1] was obtained with the $\#A$ setup and th Suburban Macro (NLOS) by the $\#C$ configuration. It is possible to reach lower value of τ_{RMS} by adding absorbers inside the chamber.

In order to estimate the needed number of absorbing material for a desired τ_{RMS}, FDTD simulations can be used. As discussed in Chapter 2, our FDTD uses uniform cubic cell, but the absorber inserted in the measurements are pyramidal. Pyramidal absorber were simulated by stratified structure Figure 5.6 whereas the ANW-77 absorber was simulates just by one sheet because it is flat and does not need further approximation. Cell size is 1.5 cm, the dimension of the pyramidal absorber (VHP-8) are:

- $a = 0.60$ m $= 41$ cells
- $b = 0.60$ m $= 41$ cells

[1] non line-of-sight, whereas LOS stands for line-of-sight

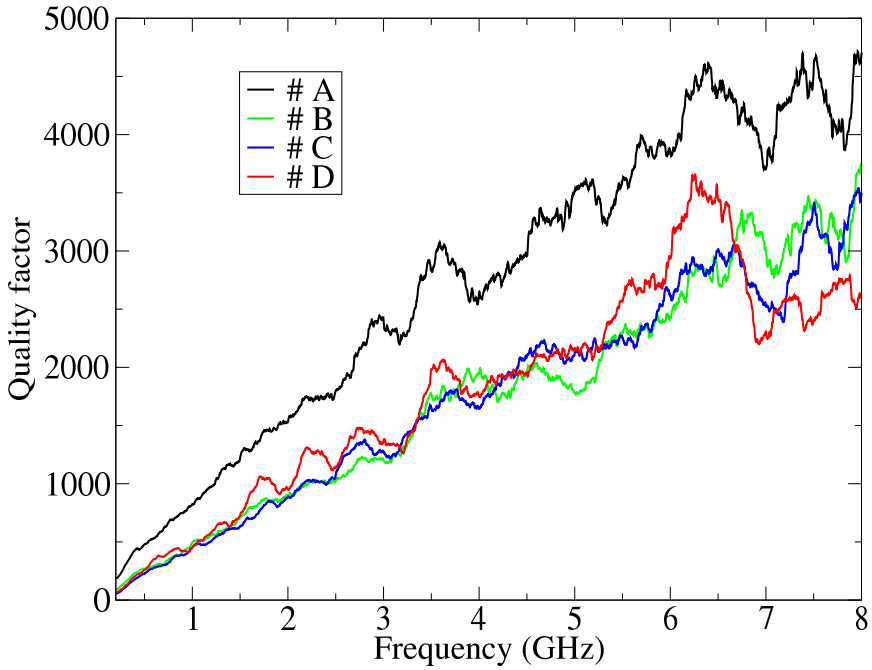

FIGURE 5.5: Measured Q-factor of different configurations of absorbers within the RC. An average sliding window over 400 frequency points have been applied.

TABLE 5.2: Values of the time delay spread according to ITU guidelines.

Scenario		Ds (ns)
Indoor Hotspot	LOS	20
	NLOS	39
Urban Micro	LOS	65
	NLOS	129
	O-to-I	49
Suburban Macro	LOS	59
	NLOS	75
Urban Macro	LOS	93
	NLOS	365
Rural Macro	LOS	32
	NLOS	37

- $c = 0.06$ m $= 4$ cells
- $d = 0.03$ m $= 2$ cells
- $e = 0.60$ m (square panel)
- $f = 0.24$ m .

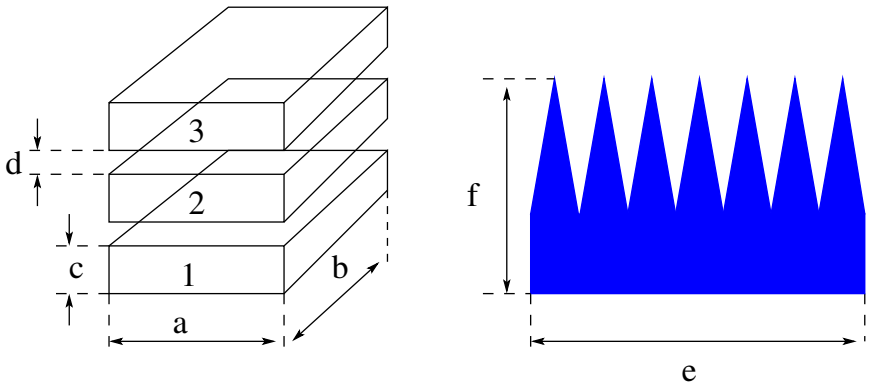

FIGURE 5.6: Sketch of the stratified structure adopted to simulate the VHP-8 pyramidal absorbers.

TABLE 5.3: Values for the simulated pyramidal absorbers. Permittivity and conductivity of each layer both VHP-8 and VHP-18.

Layer number	1	2	3	4	5	6
ϵ_r (VHP-8)	1.2	1.5	1.7	-	-	-
σ (S/m) (VHP-8)	0.01	0.05	0.08	-	-	-
ϵ_r (VHP-18)	1.2	1.5	1.7	1.9	2.2	2.5
σ (S/m) (VHP-18)	0.01	0.05	0.08	0.1	0.12	0.14

The adoption of a layered model for simulate the behavior of absorbers is given for two reasons: the staircase approximation and because the permittivity of the absorbers is unknown. In Table 5.3 are reported values of permittivity and conductibility of simulated absorbers (VHP-8 and VHP-18[2]). Figure 5.7 shows a comparison between measured and simulated PDP for the barrier case $(\#D)$, and we can note the reliability of the model for the absorber. Values chosen and then reported in Table 5.3 were evaluated after several attempts, because the factory that produces absorbers does not publish their electromagnetic properties. Moreover, those parameters are frequency dependant, there is different concentration of absorbing material on the edge w.r.t. the base. This is very complex to predict and taking into account in the simulations. These issues justify the layered model. The simulated PDP results a RMS delay spread value of 79 ns, that compared to the experimental one equal to 70 ns demonstrates the reliability of the simulation code. Moreover, we checked the ACS of a single absorber and a comparison between simulation and measurement is reported in Figure 5.8. The PDP of a reverberation chamber can be adjusted in order to emulated the desired environment. The FDTD allows to save time and money, very useful and reliable for preliminary analysis.

[2]VHP-18 has the same square dimensions w.r.t. VHP-8 but is higher

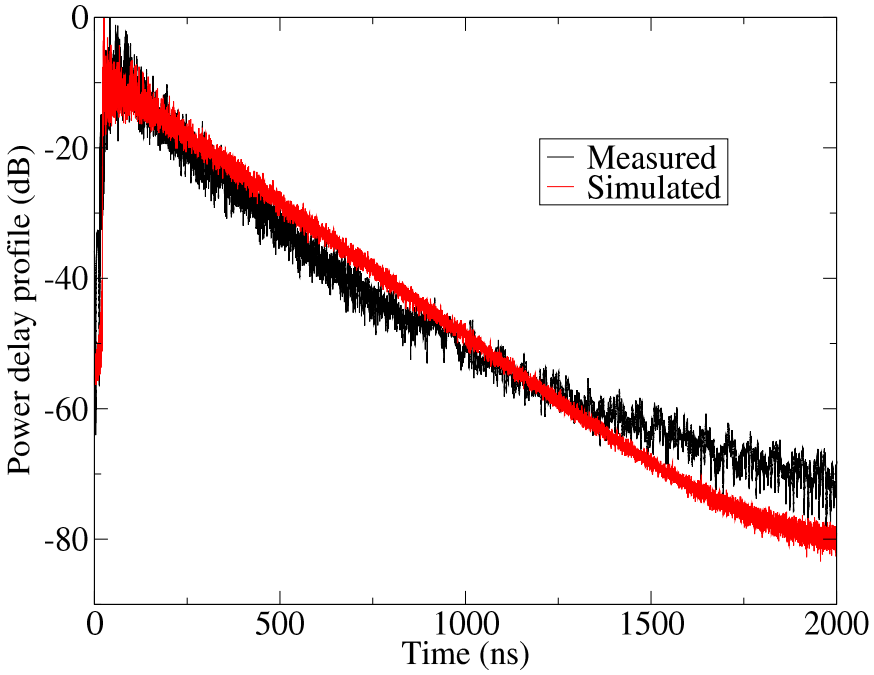

FIGURE 5.7: Measured and computed PDP for the barrier of absorbers inside the larger chamber.

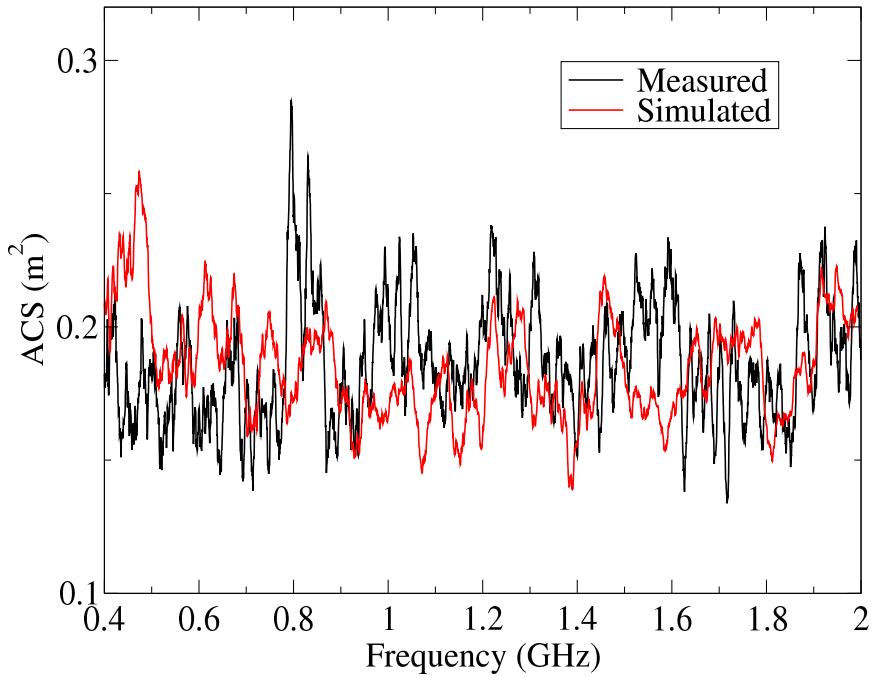

FIGURE 5.8: Comparison of the measured and simulated ACS for a single VHP-8 absorber.

Chapter 6

Shielding effectiveness measurements

6.1 Introduction

The reverberation chamber is also used to determine the shielding effectiveness (SE [dB]), i.e. enclosures, samples material for specific purposes. In the EMC the SE is a relevant parameter to take into account during the design and test of circuitry of in general electronic devices. In fact, electronic devices have to be immune to electromagnetic interferences (EMI) from external sources. The effects due to interferences cause malfunctioning or disruption (worst case) to the victim device. The SE is not only associated to electronic device but also at dedicated environment, i.e. shielding room for medical purpose where interferences are not permitted [139–144]. In order to obtain shielding environment it is possible to cover the existing building/environment (not a smart solution) or using conductive texlite [145] or build the structure/walls directly with these materials [146, 147]. During my Ph.D., in collaboration with my group, G. Gradoni from University of Nottingham, the SIMAU group of UNIVPM, D. Micheli, R. Pastore and A. Vricella from Università di Roma "La Sapienza" different sample of concrete composites were analysed, in terms of SE[1]. Concrete composites were filled by different conductive elements, i.e. metallic fibers, and with different concentrations w.r.t. the weight of the concrete and dimensions [148, 149].

6.2 Setup and nested reverberation chamber

In order to ensure that the sample under test was invested by a random excitation coming from many and random polarizations and incidence angles [150], to this purpose the nested reverberation chamber was used. To evaluate the SE and the absorption cross section (ACS [m^2]) of a material can be adopted a traditional approach based on measurements by waveguides [151, 152]. The use of the nested reverberation chamber was already adopted in [153, 154]. Basically a larger chamber was used to create a Rayleigh distributed field that excites the target sample which is mounted on the aperture of the smaller chamber (nested RC). Figure 6.1 shows the measurements setup where the larger

[1] mechanical properties were evaluated in other laboratories, we conducted the electromagnetic analysis

(outer) chamber, the smaller (inner) chamber and the aperture are highlighted. Both

FIGURE 6.1: Setup picture for the evaluation of the SE. In this picture the aperture was open and no samples are mounted on it.

FIGURE 6.2: Metallic "T" holder.

vertical and horizontal stirrer were used in synchronous way, 72 stirrer positions. The nested has dimensions $1.3 \times 0.9 \times 0.8$ m^3 whereas the aperture is 270×170 mm^2. The sample under test is mounted on a metallic "T" shaped structure, Figure 6.2. The "T" has play a duple role:

- the inner edge helps to improve the contact with the concrete Figure 6.3
- the outer edge is useful to insert a multi-hole frame that permits to force the sample on the underlying gaskets Figure 6.5.

The role played by the multi hole-frame is relevant because there will be a very good contact between the edges of the "T" holder and the aperture perimeter in order to avoid any

FIGURE 6.3: Picture of the metallic "T" holder filled by concrete.

field leakages (note also the use of gaskets), Figure 6.5 shows a mounted sample on the aperture ready for the test. Two log-periodic antennas were used in the outer chamber whereas a horn and a discone antennas were placed within the nested. The investigated

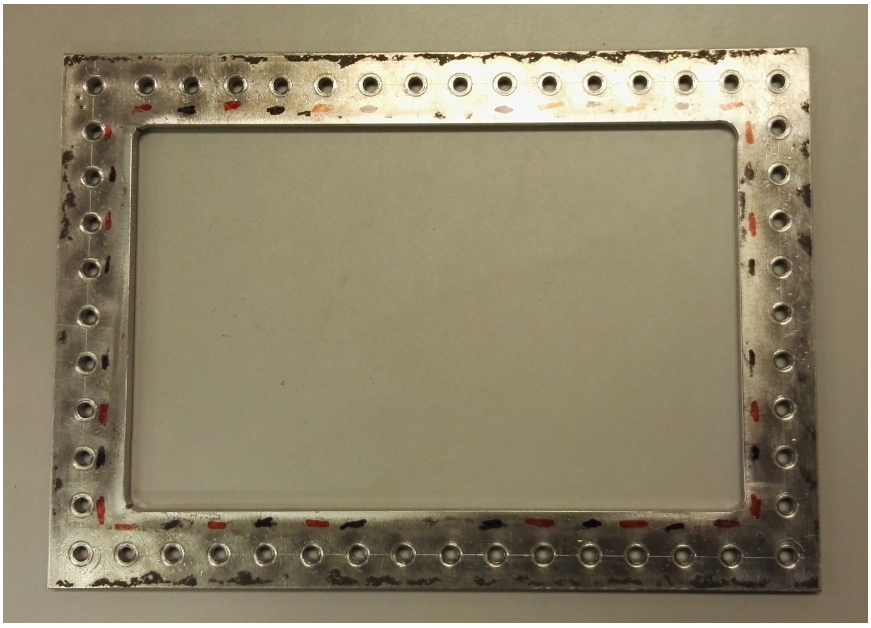

FIGURE 6.4: Multi hole-frame.

band is from 0.80 to 8.4 GHz divided in subbands of 400 MHz where 1601 points were acquired, corresponding to a frequency step of about 250 kHz. Scattering parameters were acquired by means of a 4-port VNA[2]. Antennas in the outer chamber are denoted by 1 and 2, whereas antennas within the inner chamber are denoted by 3 and 4 as showed in Figure 6.6.

[2]Agilent E5071

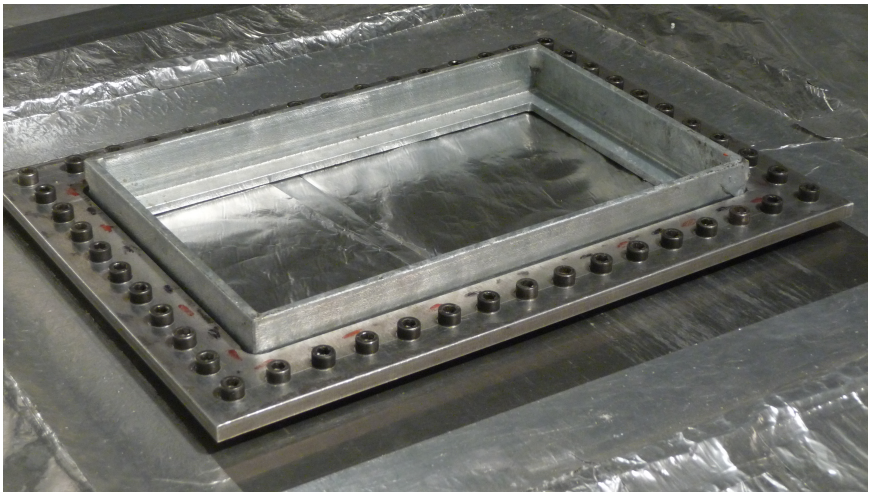

FIGURE 6.5: Picture of the sample mounted on the aperture. Gaskets are not visible because covered by the "T" holder. In this case an aluminum foil covers the aperture in order to evaluate the maximum achievable SE (called floor level in next results).

Chamber's realizations of outer chamber were given by the stirrer positions whereas in the inner chamber a frequency stirring over 400 frequency points was applied (corresponding to a chamber realization). Frequency stirring was adopted because place a stirrer or made a source stirring in the nested chamber is not ease to realize.

6.3 Shielding effectiveness and absorption cross section

The definition of the SE is simply (see Chapter 1) the ratio between the received signal (from a transmitter) without the shield to the received signal inside the shield. It can be computed by the ration of the averaged transmission cross sections of the aperture with $\sigma_{t,S}$ and without the $\sigma_{t,NS}$ sample/object under test.

$$SE = 10\log_{10}\frac{\langle\sigma_{t,NS}\rangle}{\langle\sigma_{t,S}\rangle} \tag{6.1}$$

The transmission cross sections were averaged over incident angles and polarizations. Result is equal to one (0 dB) when nothing is mounted on the aperture. Transmission cross section in a nested reverberation chamber is determined with following formulas.

$$\langle\sigma_{t,S}\rangle = \frac{\langle S_{in,S}\rangle}{\langle S_{o,S}\rangle}\frac{2\pi V}{\lambda Q_{in,S}}, \quad \text{and} \quad \langle\sigma_{t,NS}\rangle = \frac{\langle S_{in,NS}\rangle}{\langle S_{o,NS}\rangle}\frac{2\pi V}{\lambda Q_{in,NS}} \tag{6.2}$$

where S_{in} denotes the averaged scalar power densities in the inner chamber with (S) and without sample (NS) whereas S_o is the averaged scalar power densities in the outer chamber with (S) and without sample (NS). Q_{in} denotes the Q-factors with (S) and without the sample (NS), V the volume of the inner chamber and λ the wavelength,

and are evaluated by

$$Q_{in,NS} = \frac{16\pi^2 V}{\lambda^3}\frac{\langle P_{rQ,in,NS}\rangle}{P_{tx,in,NS}} \text{and} \quad Q_{in,S} = \frac{16\pi^2 V}{\lambda^3}\frac{\langle P_{rQ,in,S}\rangle}{P_{tx,in,S}} \quad . \tag{6.3}$$

The power density S can be expressed as

$$\langle S\rangle = \frac{8\pi}{\lambda^2}\langle P\rangle \tag{6.4}$$

the ratio of the of the power through the effective area of the receiving antenna. in terms of the averaged measured power through the effective area of the receiving antenna. Averaged powers $Pr_{in,S,NS}$ and $Pr_{o,s,NS}$ are referred to the inner and outer chambers with and without the sample (for these parameters the source is always in the outer chamber). $Pr_{Qin,S,NS}$ denote the average power in the inner chamber with a sample in the aperture when the transmitting antenna is located in the inner chamber with an output power $P_{tx,in,S}$. The SE was computed by

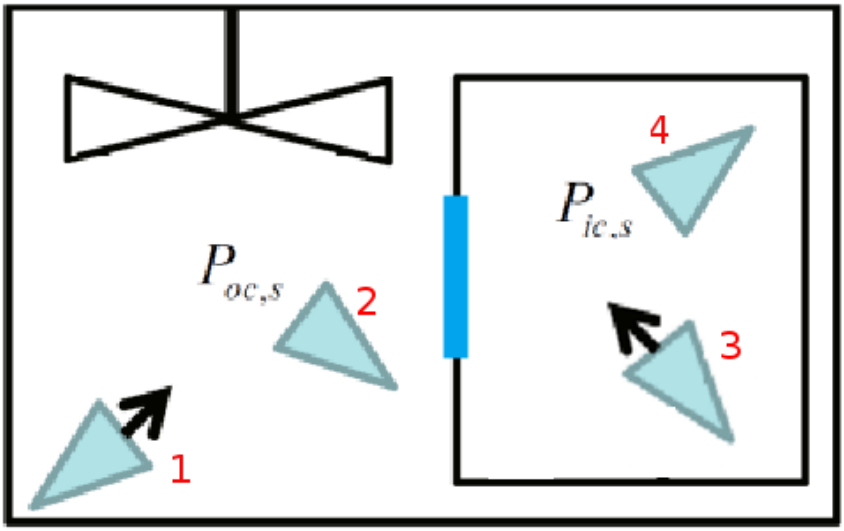

FIGURE 6.6: Simple representation of the antennas positioning inside both chambers.

$$SE = -10\log\left(\left(\frac{P_{41,S}}{P_{41,NS}}\right)\left(\frac{P_{21,NS}}{P_{21,S}}\right)\left(\frac{P_{43,NS}}{P_{43,S}}\right)\right) \tag{6.5}$$

where $P_{i,j}$ is the power received by antenna i when antenna j transmits. The terms in 6.5 represent respectively: the first ratio denotes the variation of the power received of the inner chamber when the outer chamber is fed due to the insertion of the sample (S) w.r.t. when no sample is mounted on the aperture (NS). Second and the third terms denote the ratio return the quality factor variation due to the sample insertion in the outer and inner chamber. Due to the fact that the VNA directly measures the scattering parameters,

the evaluation was done by using

$$SE = -10\log\left(\frac{<|S_{21}|^2_{NS}><|S_{41}|^2_{S}><|S_{43}|^2_{NS}>}{<|S_{21}|^2_{S}><|S_{41}|^2_{nS}><|S_{43}|^2_{S}>}\right) \tag{6.6}$$

where $<.>$ denotes the ensemble average over the chamber's realizations. Terms of 6.6 are useful for take into account the variations of the Q for both chambers (outer and inner) due by the presence of the sample. The presence of material under test has a large contribute to the evaluation of the SE, in fact sample losses i.e. absorption effects, affects the Q and the power density inside both chambers.

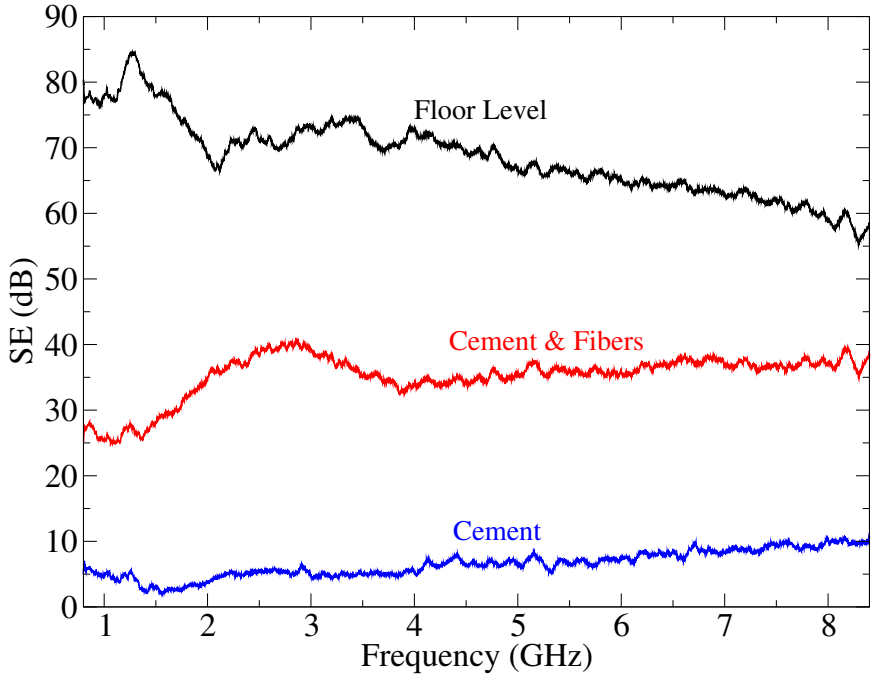

FIGURE 6.7: Measured shielding effectiveness.

Figure 6.7 shows a comparison between two different samples w.r.t the floor level. The floor level is achieved by covering the aperture by an aluminum sheet and in theory is the maximum value attainable for the SE. The samples are referred to a regular concrete (blue curve) and a concrete filled by metallic fibers [149].

Moreover, considering the energy variation it is possible to evaluate the averaged absorption cross section (ACS) for the samples by

$$ACS = \frac{\langle P_S \rangle}{S_i} \tag{6.7}$$

and then

$$ACS = \frac{\omega V}{c Q_s} = \frac{2\pi V}{\lambda Q_s} \ . \tag{6.8}$$

Figure 6.8 reports a comparison of the ACS for the two concrete samples. The ACS of the nester (inner) chamber is given by considering the S_{43} whereas the ACS of the larger

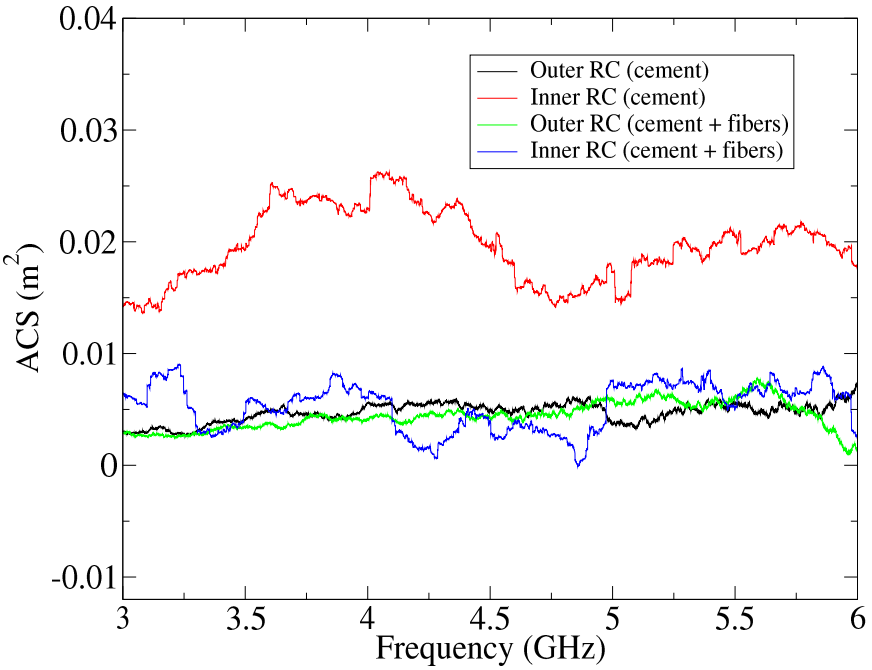

FIGURE 6.8: Comparison of the measured $ACSs$.

(outer) chamber by the S_{21}. In this case it is worth noticing that the ACS of the surface exposed to the outer RC is quite the same for both samples whereas the lower surface of the concrete without fibers has higher ACS. This means that surface exposed to the inner chamber has higher reflection and lower absorption.

Moreover, our FDTD code is able to well estimate the ACS [155].

Concluding, the RC was/is used in order to evaluate the electromagnetic properties (SE, ACS) of concrete samples (in this analysis, but non only concrete, i.e. apertures, enclosures) for preliminary tests. Consequently, other properties have to be analyzed, i.e. mechanical, chemical properties and so on.

Chapter 7

Conclusions

Analysis performed during my Ph.D. (the main items) have been reported in this thesis. Most efforts were addressed in order to improve the performance of an existing RC. Starting from the design of new geometries for the stirrer/s it was chosen to move in another direction because the design of a stirrer is restrictive to the analyzed RC and considering other RCs the dimension and shape of the stirrer can be likely useless. The analysis of a new geometry for the stirrer has been conducted. The homemade helical stirrer shows good performance at low frequency. In order to avoid this "waste" of time (just because too specific) we approached to consider new geometries for the RC. At the end of the analysis carry out after many solutions, it was shown that chaotic RCs improve the overall behavior w.r.t a regular RC. However, there are many factors that one need to control. The number of diffractors has to be relevant, few diffractors have a negligible effect. Dimension (radius) of diffractors is correlated to the number themselves. Considering a larger number of diffractors, i.e. 30 with a radius of 1 m is not recommended because they cover a large portion of the volume reducing the available volume needed to place antennas and devices; taking alway into account, the distance of $\lambda/4$ between walls (spheres' surface) and objects within the RC must be maintained in order to ensure a reliable measurement.

Adding spheres causes a decreasing of the Q-factor because lossy material is inserted into the volume, the higher the Q the more sensitive to the variation of the load. Qualitative measurement was done to check this behavior. In fact, in the simulations stirrer, antennas and spheres were simulated as PEC considering the losses localized in the whole volume of the RC. In this way adding spheres the whole volume decrease and in order to simultaneously compensate effects due to volume reduction and the decrement of the Q-factor value of the distributed losses have to be increased. With these considerations simulated results meet the experimental ones. Other parameters were analyzed. The number of uncorrelated stirrer positions, that decreases according to the lowering of the transmission coefficient S_{21}. Despite the larger number of spheres, regarding the analyzed cases the field uniformity (σ_{24}) respects the limit required by the standard. The main advantage of adding sphere within the RC is given by the improvement of the modal density. This means that a low frequency the exited mode increases. This may lead to getting low the minimum frequency of work (LUF). This analysis can be roughly made

by a priori analysis, starting from the dimensions of the chamber, i.e. volume and surface. Those dimension are easy to obtain by simple geometrical operations. The simply method to evaluate the Q-factor of the chamber is reliable and meet quite well the results obtained by the FDTD simulations. Basically it is possible to determine how many and where one has to place diffractors inside the RC to achieve the desired performance, translate the LUF. This could be a very important and "revolutionary" challenge/objective. Further analysis have to be concluded in order to quantitative quantify the transition between undermoded and ergodic region. Moreover, also the volume reduction of the chamber plays a key role in this analysis and has to be considered.

Future perspectives

Several developments may be addressed to improve the analyzed performed in this dissertation. Related to the FDTD simulations the main issues are the definition of losses for the chaotic cavity. One way could be to proceed with a subgridding to consider the surface of the sphere and compare the benefits to the required computational burden. This solution should eliminate the accuracy errors due to the staircase approximation and facilitates the possibility to run simulations considering localized losses (wall losses) instead distributed losses, which should serve to improve the accuracy of the results. However, as shown in this work, the wall losses must be evaluated for all frequencies of the band, and is not necessarily the best solution. Of course the effect that the volume reduction plays is a relevant issue that needs to be explored.

Another open point is the statistical analysis, i.e. the probability density function (pdf) of S_{21}, the coherence bandwidth or high-order momentum. It was shown that from a practical point of view, a part from the field uniformity other parameters become worse through adding spheres due to both volume reduction and increment of losses, but the modal overlap increases at low frequency. A next step is to evaluate if actually the spectrum becomes irregular. Using the FDTD is difficult to proceed with a classical analysis, i.e. considering the spacing distribution. There are some techniques however the resonances in a cavity such as the RC (at relatively high frequency) are not trivial.

Another task could be to optimize dimensions position and kind (hemisphere/hemispherical cap/mushroom) of diffractors by means of the Cost function.

Additionally, performing measurements with a device present within the working volume, will prove to be a useful comparison and extension of this work.

Bibliography

[1] A. Taflove and M. Brodwin, "Numerical solution of steady-state electromagnetic scattering problems using the time-dependent maxwell's equations," *IEEE Trans. on Microwave Theory and Techniques*, vol. 23, pp. 623–630, Aug. 1975.

[2] P. Corona, G. Latmiral, E. Paolini, and L. Piccioli, "Use of a reverberating enclosure for measurements of radiated power in the microwave range," *IEEE Trans. on EMC*, vol. 18, pp. 54–59, May 1976.

[3] P. Corona, G. Latmiral, and E. Paolini, "Performance and analysis of a reverberating enclosure with variable geometry," *IEEE Trans. on EMC*, vol. 22, no. 1, pp. 2–5, Feb. 1980.

[4] P. Corona, J. Ladbury, and G. Latmiral, "Reverberation-chamber research-then and now: a review of early work and comparison with current understanding," *IEEE Trans. on EMC*, vol. 44, no. 1, pp. 87–94, Feb. 2002.

[5] P. Corona, G. Ferrara, and M. Migliaccio, "Reverberating chambers as sources of stochastic electromagnetic fields," *IEEE Trans. on EMC*, vol. 38, no. 3, pp. 348–356, Aug. 1996.

[6] M. T. Ma, "Understanding reverberating chambers as an alternative facility for emc testing," *Journal of Electromagnetic Waves and Apllications*, vol. 2, pp. 339–351, 1988.

[7] D. A. Hill, "Plane wave integral representation for fields in reverberation chambers," *IEEE Trans. on EMC*, vol. 40, no. 3, pp. 209–217, Aug. 1998.

[8] T. Vanmareke, *Random fields*. Cambridge Mass: MIT Press, 1998.

[9] L. R. Arnaut, "Effect of local stir and spatial averaging on the measurement and testing in mode-tuned and mode-stirred reverberation chambers," *IEEE Trans. on EMC*, vol. 43, no. 3, pp. 305–325, Aug. 2001.

[10] ——, "Compound exponential distributions for undermoded reverberation chambers," *IEEE Trans. on EMC*, vol. 44, no. 3, pp. 442–457, Aug. 2002.

[11] *Electromagnetic compatibility (EMC) - Part 4-21: Testing and measurement techniques - Reverberation chamber test methods*, 2nd ed., International Standards - IEC 61000-4-21, Geneva, Switzerland, Apr. 2011.

[12] M. V. Berry and M. Tabor, "Level clustering in the regular spectrum," *Proceedings of the Royal Society of London A: Mathematical, Physical and Engineering Sciences*, vol. 356, no. 1686, pp. 375–394, 1977. [Online]. Available: http://rspa.royalsocietypublishing.org/content/356/1686/375

[13] M. V. Berry, "Semiclassical mechanics of regular and irregular motion," *Chaotic Behaviour of Deterministic Systems*, 1983.

[14] K. Selemani, J.-B. Gros, E. Richalot, O. Legrand, O. Picon, and F. Mortessagne, "Comparison of reverberation chamber shapes inspired from chaotic cavities," *IEEE Trans. on EMC*, 2015.

[15] A. Cozza, "Probability distributions of local modal-density fluctuations in an electromagnetic cavity," *IEEE Trans. on EMC*, vol. 54, no. 5, pp. 954–967, Oct. 2012.

[16] A. Taflove and S. C. Hagness, *Computational Electrodynamics: The Finite-Difference Time-Domain Method*, 2nd ed. Boston: Artech House, 2000.

[17] L. Isserlis, "On a formula for the product-moment coefficient of any order of a normal frequency distribution in any number of variables," *Biometrika*, vol. 12, no. 134, pp. 134–139, 1918.

[18] J. G. Kostas and B. Boverie, "Statistical model for a mode-stirred chamber," *IEEE Trans. on EMC*, vol. 33, pp. 366–370, Nov. 1991.

[19] D. A. Hill, *Electromagnetic Theory of reverberation chambers.* U. S. Nat. Inst. Stand. Technol. Tech. Note 1506, 1998.

[20] J. Ladbury, G. Koepke, and D. Camell, "Evaluation of the NASA Langley Research Center Mode-Stirrer Chamber Facility," *U.S. Nat. Inst. Stand. Technol. Tech. Note*, p. 1508, 1999.

[21] S. Ramo, J. R. Whinnery, and T. Duzer, *Fields And Waves in Communication Electronics.* John Wiley, 1993, vol. ser. third edition.

[22] J. J. Sakurai, *Modern Quantum Mechanics*, 1st ed. New York: Addison-Wesley, 1985.

[23] L. R. Arnaut, "Operation of electromagnetic reverberation chambers with wave diffractors at relatively low frequencies," *IEEE Trans. on EMC*, vol. 43, no. 4, pp. 637–653, Nov. 2001.

[24] R. Serra, A. C. Marvin, F. Moglie, V. M. Primiani, A. Cozza, L. R. Arnaut, Y. Huang, Y. O. Hatfield, M. Klingler, and F. Leferink, "Reverberation chambers a la carte: An overview of the different mode-stirring techniques," *IEEE Electromagnetic Compatibility Magazine*, vol. 6, pp. 63–78, May 2017.

[25] A. Gifuni, L. Bastianelli, F. Moglie, V. M. Primiani, and G. Gradoni, "Base-case model for measurement uncertainty in a reverberation chamber including frequency stirring," *IEEE Trans. on EMC*, no. 99, pp. 1–9, 2017.

[26] F. Moglie and V. Mariani Primiani, "Analysis of the independent positions of reverberation chamber stirrers as a function of their operating conditions," *IEEE Trans. on EMC*, vol. 53, no. 2, pp. 288–295, May 2011.

[27] L. R. Arnaut, "Effect of size, orientation, and eccentricity of mode stirrers on their performance in reverberation chambers," *IEEE Trans. on EMC*, vol. 48, no. 3, pp. 600–602, Aug. 2006.

[28] ——, "Nonstationary random acoustic and electromagnetic fields as wave diffusion processes," *IEEE Trans. on EMC*, vol. 50, no. 4, pp. 600–602, Aug. 2006.

[29] J. Clegg, A. C. Marvin, and J. F. D. S. J. Porter, "Optimization of stirrer designs in a reverberation chamber," *IEEE Trans. on EMC*, vol. 47, no. 4, pp. 824–832, Nov. 2005.

[30] G. Bosco, C. Picciani, V. M. Primiani, and F. Moglie, "Numerical and experimental analysis of the performance of a reduced surface stirrer for reverberation chambers," in *2012 IEEE International Symposium on Electromagnetic Compatibility*, Pittsburgh, PA, USA, 2012, pp. 156–161.

[31] O. Lundén, N. Wellander, and M. Bäckström, "Stirrer blade separation experiment in reverberation chambers," in *2010 IEEE International Symposium on Electromagnetic Compatibility*, Fort Lauderdale, Florida, USA, 2010, pp. 526–529.

[32] G. Gradoni, V. Mariani Primiani, and F. Moglie, "Reverberation chamber as a multivariate process: Fdtd evaluation of correlation matrix and independent position," *Progress In Electromagnetics Research*, vol. 133, pp. 217–234, 2013.

[33] K. S. Yee, "Numerical solution of initial boundary value problems involving maxwell's equations in isotropic media," *IEEE Trans. on Antennas and Propagation*, vol. 14, pp. 302–307, 1966.

[34] G. Mur, "Absorbing boundary conditions fot the finite-difference approximation of the time-domain electomagnetic field equation," *IEEE Trans. on EMC*, vol. 23, no. 4, pp. 377–282, Nov. 1981.

[35] J.-P. Berenger, "A perfectly matched layer for the absorption of electromagnetic waves," *Journal of computational physics*, no. 2, pp. 185–200, 1994.

[36] ——, "Perfectly matched layer (pml) for computational electromagnetics," *Synthesis Lectures on Computational Electromagnetics*, no. 1, pp. 1–117, 2007.

[37] T. H. Gan and E. L. Tan, "Mur absorbing boundary condition for 2-d leapfrog adi-fdtd method," *IEEE Asia-Pacific Conference on Antennas and Propagation*, Aug. 2012.

[38] G. Gradoni, V. M. Primiani, and F. Moglie, "Accuracy evaluation of the huygens subgridding method," in *Proc. Progress In Electromagnetic Research (PIERS)*, Moscow, Russia, Aug. 2009, pp. 1338–1343.

[39] M. R. Cabello, L. D. Angulo, A. R. Bretones, R. G. MArtin, S. G. Garcia, and J. Alvarez, "A new fdtd subgridding boundary condition for fdtd subcell lossy thin-layer modeling," in *IEEE Int. Symp. on Antennas and Propagation (APSURSI)*, 2016, pp. 2032–2032.

[40] N. Harada and M. Hano, "Pml absorbing boundary condition for noncubic cell time-domain method," *IEEE Microwave and Guded Wave Letters*, vol. 7, no. 10, pp. 335–337, Oct. 1997.

[41] J. Fang, *Time Domain Finite Difference Computation for Maxwell's Equations*. University of California Berkeley: PhD thesis, 1989.

[42] T. G. Jurgens, A. Taflove, K. Umashankar, and T. G. Moore, "Finite-difference time-domain modeling of curved surfaces," *IEEE Trans. on Antennas and Propagation*, vol. 40, pp. 357–366, 1992.

[43] K. Y. Jung, F. L. Teixeira, S. G. Garcia, and R. Lee, "On numerical artifacts of the complex envelope adi-fdtd method," *IEEE Trans. on Antennas and Propagation*, vol. 57, no. 2, pp. 491–498, Feb. 2009.

[44] A. R. Bretones, R. G. Martin, R. G. Rubio, S. G. Garcia, and M. F. Pantoja, "On the simulation of a gpr using an adi-fdtd/momtd hybrid method," Delft, The Netherlands, May 2004.

[45] A. R. Bretones, S. G. Garcia, R. G. Rubion, R. G. Martin, and A. Monorchio, "Time-domain hybrid methods to solve complex electromagnetic problems," vol. 50, Istanbul, Turkey, May 2003.

[46] S. Ramirez-Gallego, S. G. Garcia, J. M. Benitez, and F. Herrera, "Multivariate discretization based on evolutionary cut points selection for classification," *IEEE Trans. on Cybernetics*, vol. 46, no. 3, pp. 595–608, Mar. 2015.

[47] J. Alvarez, L. Angulo, A. R. Bretones, and S. G. Garcia, "A spurious-free discontinuous galerkin time-domain method for the accurate modeling of microwave filters," *IEEE Trans. on MTT*, vol. 60, no. 8, pp. 2359–2369, Jun. 2012.

[48] M. R. Cabello, L. D. Angulo, J. Alvarez, I. D. Flintoft, S. Bourke, J. F. Dawson, R. G. Martin, and S. G. Garcia, "A hybrid crank–nicolson fdtd subgridding boundary condition for lossy thin-layer modeling," *IEEE Trans. on MTT*, vol. 65, no. 5, pp. 1397–1406, Jan. 2017.

[49] J. Alvarez, J. M. Alonso-Rodriguez, H. C. Cobaleda, M. R. Cabello, L. D. Angulo, R. G. Martin, and S. G. Garcia, "Dgtd for a class of low-observable targets: A comparison

with mom and (2,2) fdtd," *IEEE Trans. on Antennas and Propagation*, vol. 13, pp. 241–244, Jan. 2014.

[50] S. G. Garcia, M. F. Pantoja, C. M. de Jong van Coeverden, A. R. Bretones, and R. G. Martin, "A new hybrid dgtd/fdtd method in 2-d," *IEEE Trans. on Microwave and Wireless Comp. Letters*, vol. 18, no. 12, pp. 764–766, Dec. 2008.

[51] A. C. Cangellaris and D. B. Wright, "Analysis of numerical error caused by the stair-stepped approximation of a conductive boundary in fdtd simulations of electromagnetic phenomena," *IEEE Trans. on Antennas and Propagation*, vol. 39, pp. 1518–1525, 1993.

[52] P. Monk and E. Suli, "A convergence analysis of yee's scheme on non-uniform grids," *IEEE Trans. Magnetics*, vol. 30, pp. 3002–3203, 1994.

[53] J. G. Maloney, K. L. Shlager, and J. S. Smith, "A simple FDTD model for transient excitation of antennas by transmission lines," *IEEE Trans. on Antennas and Propagation*, vol. 42, no. 2, pp. 289–292, Feb. 1994.

[54] C. L. Holloway, H. A. Shah, R. J. Pirkl, W. F. Young, D. A. Hill, and J. Ladbury, "Reverberation chamber techniques for determining the radiation and total efficiency of antennas," *IEEE Trans. on Antennas and Propagation*, vol. 60, no. 4, pp. 1758–1770, Apr. 2012.

[55] A. Sharaiha, P. Besnier, and G. Le Fur, "Efficiency measurement of uwb small antennas in reverberation chambers," in *The Second European Conference on Antennas and Propagation, 2007. EuCAP 2007*, Nov. 2007.

[56] F. Moglie and V. M. Primiani, "Reverberation chambers: Full 3D FDTD simulations and measurements of independent positions of the stirrers," in *2011 IEEE International Symposium on Electromagnetic Compatibility*, Long Beach, CA, USA, Aug. 2011, pp. 226–230.

[57] D. Fedeli, M. Iualè, V. M. P. F., and Moglie, "Experimental and numerical analysis of a carousel stirrer for reverberation chambers," in *2012 IEEE International Symposium on Electromagnetic Compatibility*, Pittsburgh, PA, USA, 2012, pp. 228–233.

[58] J. H. Beggs, R. J. Luebbers, K. S. Yee, and K. S. Kunz, "Finite-difference time-domain implemetation of surface impedance boundary conditions," *Trans. Antennas Propag.*, vol. 40, no. 1, pp. 49–56, Jan. 1992.

[59] F. Moglie, "Convergence of the reverberation chambers to the equilibrium analyzed with the finite-difference time-domain algorithm," *IEEE Trans. on EMC*, vol. 46, no. 3, pp. 469–476, Aug. 2004.

[60] G. Orjubin, F. Petit, E. Richalot, S. Mengué, and O. Picon, "Cavity losses modeling using lossless FDTD method," *IEEE Trans. on EMC*, vol. 48, no. 2, pp. 429–431, May 2006.

[61] P. Bonnet, R. Vernet, S. Girard, and F. Paladian, "FDTD modelling of reverberation chamber," *Electronics letters*, vol. 41, no. 20, pp. 1101–1102, 2005.

[62] F. Moglie, L. Bastianelli, and V. Mariani Primiani, "Reliable finite-difference time-domain simulations of reverberation chambers by using equivalent volumetric losses," *IEEE Trans. on EMC*, vol. 58, no. 3, pp. 653–660, Jun. 2016.

[63] L. Bastianelli, V. Mariani Primiani, and F. Moglie, "Effect of loss distribution on uncorrelated spatial points and frequency steps in reverberation chambers," in *EMC Europe*, Wroclaw, Poland, Jul. 2016.

[64] U. Carlberg, P.-S. Kildal, and J. Carlsson, "Study of antennas in reverberation chamber using method of moments with cavity green's function calculated by ewald summation," *IEEE Trans. on EMC*, vol. 47, no. 4, pp. 805–814, Nov. 2005.

[65] H. Stöckmann, *Quantum Chaos: An Introduction*. Cambridge University Press, 2006. [Online]. Available: https://books.google.co.uk/books?id=_7l-YeNORnUC

[66] L. R. Arnaut and P. D. West, "Evaluation of the NPL untuned stadium reverberation chamber using mechanical and electronic stirring techniques," *NPL Report CEM 11*, pp. 1–176, Aug. 1998.

[67] E. Ott, *Chaos in Dynamical Systems*, 2nd ed. Cambridge University Press, Sep. 2002.

[68] L. R. Arnaut, "Design of chaotic cavities with curved wave diffractors for enhanced low-frequency operation," *ArXiv e-prints*, Dec. 2014.

[69] M. L. Mehta, *Random matrices*, 3rd ed. Academic Press, 2004.

[70] F. Haake and K. Zyczkowski, "Random-matrix theory and eigenmodes of dynamical systems," *Phys. Rev. A*, vol. 42, pp. 1013–1016, Jul 1990. [Online]. Available: https://link.aps.org/doi/10.1103/PhysRevA.42.1013

[71] P. Peplowski and F. Haake, "Random-matrix theory and eigenvector statistics of dissipative dynamical systems," *Journal of Physics A: Mathematical and General*, vol. 26, no. 14, p. 3473, 1993. [Online]. Available: http://stacks.iop.org/0305-4470/26/i=14/a=014

[72] E. Ott, *Chaos in Dynamical Systems*, 2nd ed. Cambridge University Press, Sep. 2002.

[73] U. Dörr, H.-J. Stöckmann, M. Barth, and U. Kuhl, "Scarred and chaotic field distributions in a three-dimensional sinai-microwave resonator," *Phys. Rev. Lett.*, vol. 80, pp. 1030–1033, Feb. 1998.

[74] P. W. Brouwer, "Wave function statistics in open chaotic billiards," *Phys. Rev. E*, vol. 68, p. 046205, Oct 2003.

[75] R. Balian and C. Bloch, "Distribution of eigenfrequencies for the wave equation in a finite domain. ii. electromagnetic field. riemannian spaces," *Annals of Physics*, vol. 64, no. 1, pp. 271 – 307, 1971. [Online]. Available: http://www.sciencedirect.com/science/article/pii/0003491671902867

[76] H. P. Baltes and E. R. Hilf, *Spectra of finite systems*. BI-Wissenschaftsverlag Mannheim, 1976.

[77] H. Alt, A. Bäcker, C. Dembowski, H.-D. Gräf, R. Hofferbert, H. Rehfeld, and A. Richter, "Mode fluctuation distribution for spectra superconducting microwave billiards," *Physical review. E 58 (1998), 2, S. 1737-1743*, January 1998.

[78] C. Grosche, *Emerging Applications of Number Theory*. New York, NY: Springer New York, 1999, ch. Energy Fluctuation Analysis in Integrable Billiards in Hyperbolic Geometry, pp. 269–289.

[79] M. V. Berry, "Quantizing a classically ergodic system: Sinai's billiard and the kkr method," *Annals of Physics*, vol. 31, pp. 163–216, Jan. 981.

[80] O. Bohigas, M. J. Giannoni, and C. Schmit, "Characterization of chaotic quantum spectra and universality of level fluctuation laws," *Phys. Rev. Lett.*, vol. 52, pp. 1–4, Jan. 1984. [Online]. Available: https://link.aps.org/doi/10.1103/PhysRevLett.52.1

[81] Z. Cheng and J. L. Lebowitz, "Statistics of energy levels in integrable quantum systems," *Phys. Rev. A*, vol. 44, pp. 3399–3402, 1991.

[82] C. P. Dettmann and O. Georgiou, "Open mushrooms: stickiness revisited," *Journal of Physics A: Mathematical and Theoretical*, vol. 44, no. 19, p. 195102, 2011. [Online]. Available: http://stacks.iop.org/1751-8121/44/i=19/a=195102

[83] Y. G. Sinai, "On the foundations of the ergodic hypothesis for a dynamical system of statistical mechanics," *Doklady Akademii Nauk SSSR*, vol. 153, no. 6, pp. 1261–1264, 1963.

[84] ——, "Dynamical systems with elastic reflections," *Russian Mathematical Surveys*, vol. 25, pp. 137–191, 1970.

[85] M. O. Hatfield, M. B. Slocum, E. A. Godfrey, and G. J. Freyer, "Investigations to extend the lower frequency limit of reverberation chambers," Denver, CO (USA), Aug. 1998, pp. 20–23.

[86] T. J. Cox and P. D'Antonio, *Acoustic Absorbers and Diffusers*, 3rd ed. CRC Press, 2017.

[87] F. Leferink, J. C. Boudenot, and W. van Etten, "Experimental results obtained in the vibrating intrinsic reverberation chamber," in *Electromagnetic Compatibility, 2000. IEEE International Symposium on*, vol. 2, 2000, pp. 639–644.

[88] F. B. J. Leferink, "High field strength in a large volume: the intrinsic reverberation chamber," in *1998 IEEE EMC Symposium. International Symposium on Electromagnetic Compatibility*, vol. 1, Aug. 1998, pp. 24–27.

[89] S. Baoli, R. Wu, G. Benqing, and Y. Shiming, "The analysis of several diffusers in a reverberation chamber by fdtd method," in *2002 3rd International Conference on Microwave and Millimeter Wave Technology, 2002. Proceedings. ICMMT 2002.*, Aug. 2002, pp. 911–914.

[90] L. Bastianelli, G. Gradoni, F. Moglie, and V. M. Primiani, "Bringing chaos inside the reverberation chamber," Nuremberg, Germany, 2017.

[91] W. Lukosz, "Electromagnetic zero-point energy shift induced by conducting surfaces: Ii. the infinite wedge and the rectangular cavity," *Z. Phys.*, vol. 262, pp. 327–348, 1973.

[92] H. Weyl, "Über die randwertaufgabe der strahlungstheorie and asymptotische spektralgesetze," *J. Reine Angew. Math.*, vol. 143, pp. 177–202, 1913.

[93] C. Vaa, P. M. Koch, and R. Blümel, "Weyl formula: Experimental test of ray splitting and corner corrections," *Phys. Rev. E*, vol. 72, p. 056211, Nov 2005.

[94] H. Weyl, "Das asymptotische verteilungsgesetz der eigenwerte linearer partieller differentialgleichungen (mit einer anwendung auf die theorie der hohlraumstrahlung)," *Mathematische Annalen*, vol. 71, no. 4, pp. 441–479, 1971. [Online]. Available: http://dx.doi.org/10.1007/BF01456804

[95] ——, "Über die abhängigkeit der eigenschwingungen einer membran und deren begrenzung." *Journal für die reine und angewandte Mathematik*, vol. 141, pp. 1–11, 1912. [Online]. Available: http://eudml.org/doc/149369

[96] J.-B. Gros, U. Kuhl, O. Legrand, and F. Mortessagne, "Lossy chaotic electromagnetic reverberation chambers: Universal statistical behavior of the vectorial field," *Phys. Rev. E*, vol. 93, Mar. 2016.

[97] J.-B. Gros, O. Legrand, F. Mortessagne, E. Richalot, and K. Selemani, "Universal behaviour of a wave chaos based electromagnetic reverberation chamber," *Wave Motion*, vol. 51, no. 4, pp. 664–672, 2014.

[98] K. Selemani, E. Richalot, O. Legrand, O. Picon, and F. Mortessagne, "Energy localization effects within a reverberation chamber and their reduction in chaotic geometries," *IEEE Transactions on Electromagnetic Compatibility*, vol. 59, no. 2, pp. 325–333, Apr. 2017.

[99] A. Cozza, "The role of losses in the definition of the overmoded condition for reverberation chambers and their statistics," *IEEE Trans. on EMC*, vol. 53, no. 2, pp. 296–307, May 2011.

[100] ——, "Likelihood of meeting isotropic conditions in reverberation chambers from power transmission," *IEEE Antennas Wireless Propag. Lett.*, vol. 16, pp. 2881–2884, 2017.

[101] B. H. Liu, D. C. Chang, and M. T. Ma, "Eigenmodes and the composite quality factor of a reverberating chamber," *U.S. Govern. Printing Office, NBS Tech. Note 1066*, 1983.

[102] C. L. Holloway, D. A. Hill, J. M. Ladbury, P. F. Wilson, G. Koepke, and J. Coder, "On the use of reverberation chambers to simulate a Rician radio environment for the testing of wireless devices," *IEEE Trans. on Antennas and Propagation*, vol. 54, no. 11, pp. 3167–3177, Nov. 2006.

[103] G. Gradoni, T. M. Antonsen, S. M. Anlage, and E. Ott, "A statistical model for the excitation of cavities through apertures," *IEEE Trans. on EMC*, vol. 57, no. 5, pp. 1049–1061, Jul. 2015.

[104] G. Gradoni, J.-H. Yeh, T. M. Antonsen, S. M. Anlage, and E. Ott, "Wave chaotic analysis of weakly coupled reverberation chambers," in *Int. Sym. on EMC*, Long Beach, CA, USA, Oct. 2011.

[105] Z. B. Drikas, J. G. Gil, S. K. Hong, T. D. Andreadis, J.-H. Yeh, B. T. Taddese, and S. M. Anlage, "Application of the random coupling model to electromagnetic statistics in complex enclosures," *IEEE Trans. on EMC*, vol. 56, no. 6, pp. 1480–1487, Sep. 2014.

[106] G. Gradoni, J.-H. Yeh, T. M. Antonsen, S. M. Anlage, and E. Ott, "Predicting the statistics of wave transport through chaotic cavities by the random coupling model: a review and recent progress," Mar. 2013.

[107] G. Gradoni, C. Xiaoming, T. M. Antonsen, S. M. Anlage, and E. Ott, "Random coupling model for wireless communication channels," in *Int. Sym. on EMC*, Gothenburg, Sweden, Sep. 2014.

[108] G. Gradoni, V. M. Primiani, and F. Moglie, "Effect of losses on the maximum-to-mean value in a mode-stirred reverberation chamber," in *2014 International Symposium on Electromagnetic Compatibility*, Gothenburg, Sweden, Sep. 2014, pp. 318–323.

[109] F. Moglie and V. M. Primiani, "Numerical analysis of a new location for the working volume inside a reverberation chamber," vol. 54(2), p. 238–245, Apr. 2012.

[110] L. Bastianelli, F. Moglie, and V. M. Primiani, "Evaluation of stirrer efficiency varying the volume of the reverberation chamber," in *2016 IEEE International Symposium on Electromagnetic Compatibility (EMC)*, Ottawa, Canada, July 2016, pp. 19–24.

[111] V. M. P. L. Bastianelli and F. Moglie, "Stirrer efficiency as a function of its axis orientation," *IEEE Trans. on EMC*, vol. 57, no. 6, pp. 1732–1735, Dec. 2015.

[112] N. Wellander, O. Lundén, and M. Bäckström, "Experimental investigation and mathematical modeling of design parameters for efficient stirrers in mode-stirred reverberation chamber," *IEEE Trans. on EMC*, vol. 49, no. 1, pp. 94–103, Feb. 2007.

[113] F. Moglie and V. M. Primiani, "Numerical analysis of a new location for the working volume inside a reverberation chamber," *IEEE Trans. on EMC*, vol. 54, no. 2, pp. 238–245, Apr. 2012.

[114] V. M. Primiani and F. Moglie, "Numerical determination of reverberation chamber field uniformity by a 3-d simulation," in *EMC Europe*, York, United Kingdom, 2011, pp. 829–832.

[115] L. R. Arnaut, F. Moglie, L. Bastianelli, and V. M. Primiani, "Helical stirring for enhanced performance of reverberation chambers," *IEEE Trans. on EMC*, vol. 59, no. 4, Aug. 2017, accepted for pubblication, DOI: 10.1109/TEMC.2016.2641386.

[116] V. Creta, L. Bastianelli, F. Moglie, V. M. Primiani, and L. R. Arnaut, "Stirring performance of helically distributed paddles," Washington, DC, USA, Aug. 2017.

[117] A. C. Marvin, J. A. S. Angus, J. F. Dawson, and J. Clegg, "Enhancement to stirred mode chambers by the use of pseudo-random phase reflection gratings," Rome, Italy, 1994, pp. 218–221.

[118] M. Petirsch and A. J. Schwab, "nvestigation of the field uniformity of a mode-stirred chamber using diffusors based on acoustic theory," *IEEE Trans. on EMC*, vol. 41, no. 4, pp. 446–451, Nov. 1999.

[119] J.-B. Gros, U. Kuhl, O. Legrand, F. Mortessagne, O. Picon, and E. Ricahlot, "Statistics of the electromagnetic response of a chaotic reverberation chamber," *Adv. Electromagn.*, vol. 4, no. 2, pp. 38–43, 2015.

[120] C. L. Holloway, D. A. H. J. M., Ladbury, and G. Koepke, "Requirements for an effective reverberation chamber: Unloaded or loaded," *IEEE Trans. on EMC*, vol. 48, no. 1, pp. 187–194, Feb. 2006.

[121] L. Bastianelli, L. Giacometti, V. M. Primiani, and F. Moglie, "Effect of absorber number and positioning on the power delay profile of a reverberation chamber," in *2015 IEEE International Symposium on Electromagnetic Compatibility (EMC)*, Dresden, Germany, Aug. 2015, pp. 422–427.

[122] C. L. Holloway, H. A. Shah, R. J. Pirkl, K. A. Remley, D. A. Hill, and J. Ladbury, "Early time behavior in reverberation chambers and its effect on the relationships between coherence bandwidth, chamber decay time, RMS delay spread, and the chamber buildup time," *IEEE Trans. on EMC*, vol. 54, no. 4, pp. 714–725, Aug. 2012.

[123] A. J. Pomianek, K. Staniec, and Z. Joskiewicz, "Practical remarks on measurement and simulation methods to emulate the wireless channel in the reverberation chamber," *Progress In Electromagnetics Research*, vol. 105, pp. 49–69, 2010.

[124] E. Genender, C. L. Holloway, K. A. Remley, J. M. Ladbury, G. Koepke, and G. H. Garbe, "Simulating the multipath channel with a reverberation chamber: Application to bit error rate measurements," *IEEE Trans. on EMC*, vol. 52, no. 4, pp. 766–777, Nov. 2010.

[125] R. Recanatini, F. Moglie, and V. M. Primiani, "Performance and immunity evaluation of complete WLAN systems in a large reverberation chamber," *IEEE Trans. on EMC*, vol. 55, no. 5, pp. 806–815, Oct. 2013.

[126] D. Micheli, M. Barazzetta, F. Moglie, and V. M. Primiani, "Power boosting and compensation during OTA testing of a real 4G LTE base station in reverberation chamber," *IEEE Trans. on EMC*, vol. 57, no. 4, pp. 623–634, Aug. 2015.

[127] M. Barazzetta, D. Micheli, F. Moglie, and V. M. Primiani, "Over-the-air performance testing of a real 4g lte base station in a reverberation chamber," Raleigh, NC, USA, Aug. 2014.

[128] *Guidelines for evaluation of radio interface technologies for IMT-Advanced*, International Telecommunication Union - ITU Report M.2135-1, Dec. 2009.

[129] *Propagation data and prediction methods for the planning of indoor radiocommunication systems and radio local area networks in the frequency range 900 MHz to 100 GHz*, International Telecommunication Union - ITU Recommendation P.1238-7, Feb. 2012.

[130] D. Micheli, M. Barazzetta, C. Carlini, R. Diamanti, V. M. Primiani, and F. Moglie, "Testing of the carrier aggregation mode for a live LTE base station in reverberation chamber," *IEEE Journal on Vehicular Technology*, 2016, available online. DOI: 10.1109/TVT.2016.2587662.

[131] X. Chen, P.-S. Kildal, C. Orlenius, and J. Carlsson, "Channel sounding of loaded reverberation chamber for over-the-air testing of wireless devices: Coherence bandwidth versus average mode bandwidth and delay spread," *IEEE Antennas Wireless Propag. Lett.*, vol. 8, pp. 678–681, 2009.

[132] C. Xiaoming, P.-S. Kildal, and J. Carlsson, "Verification of the Rician K-factor-based uncertainty model for measurements in reverberation chambers," *IET Science, Measurement Technology*, vol. 9, no. 5, pp. 534–539, 2015.

[133] M. Barazzetta, D. Micheli, R. Diamanti, L. Bastianelli, F. Moglie, and V. M. Primiani, "Optimization of 4G wireless access network features by using reverberation chambers: Application to high-speed train LTE users," in *2016 46th European Microwave Conference (EuMC)*, Oct. 2016, pp. 719–722.

[134] M. Barazzetta, D. Micheli, L. Bastianelli, R. Diamanti, M. Totta, P. Obino, R. Lattanzi, F. Moglie, and V. M. Primiani, "A comparison between different reception diversity schemes of a 4G-LTE base station in reverberation chamber: a deployment in a live cellular network," *IEEE Trans. on EMC*, vol. 59, no. 6, Dec. 2017.

[135] G. Esposito, G. Gradoni, F. Moglie, and V. Mariani Primiani, "Stirrer performance of reverberation chambers evaluated by time domain fidelity," *2013 IEEE International Symposium on Electromagnetic Compatibility (EMC)*, pp. 207–212,5–9, Aug. 2013.

[136] E. Genender, C. L. Holloway, K. A. Remley, J. Ladbury, G. Koepke, and H. Garbe, "Use of reverberation chamber to simulate the power delay profile of a wireless environment," in *2008 Int. Symp. Electromagn. Compat. - EMC Europe*, Hamburg, Germany, Sep. 2008, pp. 1–6.

[137] O. Lundén and M. Bäckström, "Absorber loading study in FOI 36.7 m^3 mode stirred reverberation chamber for pulsed power measurements," in *2008 IEEE Int. Symp. Electromagn. Compat. EMC 2008.*, Detroit, MI, USA, Aug. 2008.

[138] V. M. Primiani and F. Moglie, "Numerical simulation of reverberation chamber parameters affecting the received power statistics," *IEEE Trans. on EMC*, vol. 54, no. 3, pp. 522–532, Jun. 2012.

[139] *Medical electrical equipment - Part 1-2: General Requirements for basic safety and essential performance*, Collateral Standards - IEC 60601-1-2 Electromagnetic disturbances - Requirements and tests, 2014.

[140] *Medical Devices Agency Electromagnetic Compatibility of Medical Devices with Mobile Communications*, Devices Bulletin - DB9702 - Department of Health, London, United Kingdom, 1997.

[141] A. Baranchuk, J. Kang, C. Shaw, D. Campbell, S. Ribas, W. M. Hopman, H. Alanazi, D. P. Redfearn, and C. S. Simpson, "Electromagnetic interference of communication devices on ECG machines," vol. 32, no. NIST TN–1508, 2009, pp. 588–592.

[142] A. Kreth, E. Genender, O. Doering, and H. Garbe, "Identifying electromagnetic attacks against airports," in *Aerospace EMC, 2012 Proceedings ESA Workshop*, Venice, Italy, 2012, pp. 1–5.

[143] *NSA-82-89 NACSIM 5000 TEMPEST Fundamentals*, National Security Agency, Feb. 1982.

[144] *Directive 2004/108/EC of the European Parliament and of the Council of 15 December 2004 on the approximation of the laws of the Member States relating to electromagnetic compatibility and repealing Directive 89/336/EECText with EEArelevance*, Dec. 2004.

[145] T. W. Wieckowski and J. M. Janukiewicz, "Methods for evaluating the shielding effectiveness of textiles," *Fibres and Textiles in Eastern Europe*, vol. 14, no. 5, pp. 18–22, 2006.

[146] R. D. Leo, G. Gradoni, A. Mazzoli, F. Moglie, G. Moriconi, and V. M. Primiani, "Shielding effectiveness evaluation of densified-small-particles (dsp) cement composite," in *Electromagnetic Compatibility - EMC Europe, 2008 International Symposium on*, Sep. 2008, pp. 1–6.

[147] ——, "DSP cement composites for electromagnetic shielding: practice and experimental analysis," in *Electromagnetic Compatibility (EMC Europe) International Symposium*, Athens, Greece, Jun. 2009, pp. 1–4.

[148] D. Micheli, A. Vricella, R. Pastore, A. Delfini, R. B. Morles, M. Marchetti, F. Santoni, V. Corinaldesi, A. Mazzoli, J. Donnini, L. Bastianelli, F. Moglie, and V. M. Primiani, "Electromagnetic properties of carbon nanotube reinforced concrete composites for frequency selective shielding structures," *Methods for Evaluating the Shielding Effectiveness of Textiles*, vol. 131, pp. 267–277, Jan. 2017.

[149] L. Bastianelli, S.Capra, G. Gradoni, D. Micheli, A. Vricella, V. Corinaldesi, A. Mazzoli, F. Moglie, and V. M. Primiani, "Shielding effectiveness statistical evaluation of random concrete composites," in *International Workshop on Metrology for AeroSpace*, Florence, Italy, Jun. 2016.

[150] P. Corona, G. Ferrara, and M. Migliaccio, "Generalized stochastic field model for reverberating chambers," *IEEE Trans. on EMC*, vol. 46, no. 4, pp. 655–660, Nov. 2004.

[151] A. Tamburrano, D. Desideri, A. Maschio, and M. S. Sarto, "Coaxial waveguide methods for shielding effectiveness measurement of planar materials up to 18 ghz," *IEEE Trans. on EMC*, vol. 56, no. 6, pp. 1386–1395, Jun. 2014.

[152] P. Dehkhoda, A. Tavakoli, and R. Moini, "An efficient and reliable shielding effectiveness evaluation of a rectangular enclosure with numerous apertures," *IEEE Trans. on EMC*, vol. 50, no. 1, pp. 208–212, Feb. 2008.

[153] D. Micheli, M. Marchetti, R. Pastore, A. Vricella, G. Gradoni, F. Moglie, and V. M. Primiani, "Shielding effectiveness of carbon nanotube reinforced concrete composites by reverberation chamber measurements," in *Electromagnetics in Advanced Applications (ICEAA), 2015 International Conference*, Turin, Italy, Sep. 2015, pp. 145–148.

[154] A. Gifuni, G. Ferrara, A. Sorrentino, and M. Migliaccio, "Analysis of the measurement uncertainty of the absorption cross section in a reverberation chamber," *IEEE Trans. on EMC*, vol. 57, no. 5, pp. 1262–1265, Oct. 2015.

[155] G. Gradoni, D. Micheli, F. Moglie, and V. M. Primiani, "Absorbing cross section in reverberation chamber: Experimental and numerical results," *Progress In Electromagnetics Research B*, vol. 45, pp. 187–202, 2012.